

POLITECNICO DI TORINO

MASTER DEGREE COURSE IN CIVIL ENGINEERING



**HYBRID REINFORCED CONCRETE ELEMENTS (HRC):
BRIDGED CRACK MODEL DETERMINATION OF
MINIMUM REINFORCEMENT CONDITIONS**

Master Degree Thesis

Supervisor

Chiar.mo Prof. Ing. Alberto Carpinteri

Co-Supervisor

Ill.mo Dr. Ing. Federico Accornero

Ill.mo Ing. Alessio Rubino

Candidate

Gianluca Terranova

A.A. 2020/21

ABSTRACT

In the framework of Fracture Mechanics, this Master Thesis aims to analyze the behaviour of Hybrid Reinforced Concrete (HRC) structural elements, in which the reinforcing secondary phase consists in a combination of ordinary steel rebars and short discontinuous fibres.

Analogously to the case of Fibre Reinforced Concrete (FRC) members, experimental campaigns suggest to subdivide the flexural behaviour of HRC beams into three different stages. Considering a notched HRC element subjected to bending the related applied load versus deflection diagram starts with a linear elastic branch (Stage I), up to the initiation of the fracturing process. Then, the post-cracking regime of the composite takes place, which depends on the amount of ordinary steel rebars and of reinforcing fibres. In the first part of this regime (Stage II), both fibres and steel rebars provide their contribution in terms of closing action against crack propagation. Finally, the toughening contribution of the fibres gradually decreases with the crack propagation, leading to a final plastic plateau (Stage III), which depends only on the amount of traditional steel rebars.

As reported in Chapter 2, the Bridged Crack Model is proposed as a Fracture Mechanics approach able to describe the evolution of the crack propagation process at the notched (or critical) cross-section of HRC members subjected to monotonically increasing flexural loading. The model assumes an elastic-perfectly brittle behaviour of the concrete matrix, whose toughening contribution is described by the concrete fracture toughness, K_{IC} . On the other hand, appropriate constitutive laws describe the toughening contribution of the reinforcing secondary phase, which relates to the yielding of the steel rebars and to the slippage of the steel fibres, respectively. The numerical model has been extended in order to simultaneously consider the effect of these two different bridging mechanisms, as described in Chapter 3.

In Chapter 4, parametric sets of numerical simulations are presented, showing that the abovementioned post-cracking regimes are actually governed by three scale-dependent dimensionless numbers: (i) two reinforcement dimensionless numbers, N_{Pb} and N_{Pf} , which are directly related to the steel area percentage, ρ , and to the fibre volume fraction, V_f , respectively; (ii) the dimensionless number, N_w , which depends on the fibre embedment length, w_c . The focus of the present analysis is on the combination of these three dimensionless numbers, which provides the minimum reinforcement condition, i.e., the minimum percentage steel area, ρ_{min} , or minimum fibre volume fraction, $V_{f,min}$, required to obtain a stable post-cracking response, together with its scale-dependence.

Finally, in Chapter 5 the model is validated on the basis of different experimental campaigns reported in the scientific literature, in which flexural tests were carried out on HRC beams. It is shown that the identification of the mechanical properties of the composite leads to an effective superposition between experimental data and numerical predictions, thus promoting the model as an effective tool to predict the flexural behaviour of HRC structural members together with the minimum reinforcement condition.

Contents

1	Introduction	7
2	The Bridged Crack Model	9
2.1	Introduction	9
2.2	Fundamentals	11
2.2.1	Basic Assumption	11
2.2.2	Stress Intensity Factor	13
2.2.3	Compatibility equation	15
2.2.4	Constitutive Laws	17
2.2.5	Moment rotation response and dimensionless number	25
3	Numerical Algorithm	29
3.1	Crack Length Control Scheme (CLCS)	29
3.2	Numerical errors	32
3.3	Number of fibres	34
4	Dimensional Analysis and Numerical Simulations	37
4.1	Buckingham's π Theorem	37
4.2	Influence of N_{Pb} on the flexural response	40
4.3	Influence of N_{Pb} on the flexural response	45
4.4	Influence of N_w on the flexural response	50
4.5	Minimum reinforcement condition	55
5	Experimental results	59
5.1	Introduction	59
5.2	Comparison with experimental data	61

5.2.1	Holschemacher et al. experimental work.....	61
5.2.2	Mobasher et al. experimental work	75
5.2.3	Fantilli et al. experimental work.....	86
6	Conclusions	101
7	References	103

1 Introduction

Recent developments in concrete technology revealed the advantages in the structural performance of the material by including fibres in the concrete mixture or in a Reinforced Concrete (RC) element. In this perspective, the Fibre Reinforced Concrete (FRC) and Hybrid Reinforced Concrete (HRC) were developed since the mid-twentieth century, particularly in the last 30 years (Carpinteri, 1981; Carpinteri, 1984; Carpinteri and Bosco, 1991a; Carpinteri and Bosco 1991b; Altun et al. 2007; Jones, Austin and Robins, 2008; Carpinteri et al, 2015; Accornero, Rubino and Carpinteri, 2019; Fantilli and Gorino,2020). HRC element can be generally defined as a cementitious composite made of two main components: the cementitious matrix and the reinforcement, which is in turn can be made of fibres and steel rebars. The cementitious matrix may itself be considered a composite with several components (aggregate, additive, water), but it will be assumed to represent, in this context, the first main component of the HRC composite. The secondary phase of the composite is the reinforcement, made of short discontinuous fibres, that are randomly oriented and distributed within the volume of the composite, and of steel rebars. Both the fibres, the rebars and the matrix work together, providing the synergism required to make an effective composite. The constituents are characterized by enormous variability. High Strength Concrete, High Performance Concrete and many others special cementitious matrices are available with modern technologies. Fibres also can be really different, both for material and geometry. They can be made of steel, polymeric materials as well as inorganic materials such as carbon, glass and natural materials (CNR, 2006). Moreover, the fibres shape can be undeformed (straight), with a round or flat section; or characterized by a deformed profile, such as crimped along the length or with hooked end. The bars can be made of steel, plastic, glass and other inorganic materials and their shape is typical undeformed; they can vary their diameter or their yield strength. Moreover, the surface of the bars can be smooth or may have ribs to improve adhesion. This work is focused on composites with steel fibres and with steel rebars, but the concepts relating to mechanical and geometric parameters could also be extended to other materials.

The experimental research on the flexural behaviour of the HRC specimens points out three different stages into a typical load-deflection curve. The diagram starts with a linear elastic branch (Stage I), up to the initiation of the fracturing process. Then, the post-cracking regime of the composite takes place, which depends on the amount of ordinary steel rebars and of reinforcing fibres. In the first part of this regime (Stage II), both fibres and steel rebars provide their contribution in terms of closing action against crack propagation. Depending on several conditions, including the fibre volume continent (V_f) and the steel area percentage (ρ), the element could exhibit a different behaviour in the second stage, such as brittle, perfectly plastic or hardening. Increasing the amount of reinforcement (both bars and fibres), there is a ductile-to-brittle transition, which suggests the definition of the *minimum reinforcement condition* required to guarantee a stable post-cracking response. Finally, the toughening contribution of the fibres gradually decreases with the crack propagation, leading to a final plastic plateau (Stage III), which depends only on the amount of traditional steel rebars.

The fundamental role of the secondary phase is that of providing crack control and improving the fracture toughness of the composite, by means of a bridging action affecting the matrix macro- and microcracks. However, several parameters have to be taken into account in the design of the so called *minimum reinforcement*: fibres and bars geometric and mechanical characteristics, concrete mechanical properties, fibre volume fraction, steel area percentage, position of the bars and geometrical characteristic of the structural element. Experimental tests are thus necessary, both on the three individual main components and on the composite mixture.

The purpose of this work is to interpret the aforementioned stages in the framework of Fracture Mechanics. Following this purpose, the Bridged Crack Model is proposed to reproduce analytically the flexural response, providing the identification of the constituent materials. The application of Buckingham's π Theorem confirm the presence of three scale-dependent dimensionless parameters, which synthetically describe the post-cracking response of the composite.

Moreover, the flexural behaviour of different specimens made of the same materials vary according to specimen size. This phenomenon, known as *size effect*, depends on the fact that the dimensionless parameters mentioned above, which synthetically describe the flexural response, are scale-dependent.

In the case of modern high technology composite materials, such as Fibre Reinforced Concrete or Hybrid Reinforced Concrete, there are two alternative nonlinear models that are used to analyse the failure process: the Bridged Crack Model and the Cohesive Crack Model. They were presented in a dimensionless formulation by Carpinteri et al. (1996) and an experimental campaign demonstrated that correctly choosing the characteristic parameter of the two models, both of them lead to similar structural behaviour.

The Cohesive Crack Model, in accordance with the model proposed by Barenblatt (1962) for the analysis of brittle heterogeneous materials and then by Dugdale (1962) for the analysis of ductile materials, has been originally proposed by Hillerborg et al (1976) with the name of Fictitious Crack Model.

The key differences between these two models regard the material's basic assumption, the crack tip stress field and the corresponding crack propagation conditions. These lead to the two different options of the model, which will be called *bridging option* and *cohesive option*. In the *bridging option* the composite is theoretically simulated as a bi-phase material. A singular stress field is assumed at the crack-tip and the crack starts propagating when the crack tip stress intensity factor reaches the matrix fracture toughness. In the *cohesive option*, on the other hand, the composite material is assumed to be homogeneous. A finite stress field is assumed in the crack tip vicinity, and consequently the crack starts propagating when the total crack tip stress intensity factor becomes equal to zero.

In conclusion, it will be clear how, by means of Bridged Crack Model, it is possible to interpret the tests and predict the mechanical behaviour of the structural element, by varying the design parameters.

2 The Bridged Crack Model

2.1 Introduction

As mentioned in the previous chapter, two nonlinear models can be used to analyse the failure process: the Bridged Crack Model and the Cohesive Crack Model. In this work it will be analyzed the Bridged Crack Model. This model is a nonlinear fracture mechanics model which simulates the bridging zone and the bridging mechanisms of the material through a crack and a continuous or discontinuous distribution of closing tractions, directly applied into the crack faces. Different versions of this model have been formulated for the analysis of composites with uniformly distributed reinforcements (Marshall et al., 1985; Jenq and Shah, 1985; Cox and Marshall, 1991; Ballarini and Muju, 1993). Moreover, bridged -crack models have been proposed for the analysis of the overall behavior of brittle-matrix composites with localized reinforcements, such as bars, wires, and riveted or bonded stiffeners (Carpinteri, 1984; Desayi and Ganesan, 1986; Bosco and Carpinteri, 1992; Carpinteri and Massabò, 1994).

Within the Bridged Crack Model, the composite is interpreted as a bi-phase material, in which the brittle matrix and the reinforcement (both fibres and bars) represent the primary and secondary phase of the mixture, respectively. Thus, the mechanical behaviour of the two distinct phases is differently characterized, including the related contributions in terms of toughening mechanism. The behaviour of the matrix is assumed as elastic-perfectly brittle and it is characterized by Young's modulus, E , and fracture toughness, K_{IC} . On the other hand, The Bridged Crack Model replaces the secondary-phase bridging action by means of concentrated forces directly applied into the crack faces; as far as fibres are concerned the bridging mechanism of the secondary phase is described by a cohesive softening constitutive law, which takes into account the progressive slippage of the fibre from the matrix. Instead, the bar's contribution is described by an elastic-perfectly plastic constitutive law, which takes into account the yielding of the bar, but not the possible slipping of the same. Under these assumptions, the singular crack-tip stress field is uniquely characterized by a global stress-intensity factor, K_I . In agreement with the LEFM, the failure process is governed by the stress-intensity factor at the crack tip and the criterion for crack growth is reached when $K_I = K_{IC}$.

The analytical formulation derives from a model formerly proposed by Carpinteri (1984) for composites with localized reinforcements. The nonlinear integral problem, describing the evolution of crack propagation in a composite section under monotonic bending, is solved through the verification of both equilibrium and kinematic compatibility.

This discontinuous model was able to describe the behaviour of element with localized reinforcement, such as bars, wires, fibres and riveted or bonded stiffeners. However, when the number of localized reinforcements becomes sufficiently high, the global results of discontinuous and continuous models are convergent (A. Carpinteri et al., 1997).

In this Chapter is presented a discontinuous model for RC, FRC and HRC beams under monotonic bending, which is the base of the numerical algorithm. The novelty, in comparison to previous versions of the model, is

the possibility of being able to analyze HRC elements, in which the fibres and bars contribute together to the bridging action on the crack.

2.2 Fundamentals

2.2.1 Basic Assumption

As briefly introduced in the previous section, the Bridged Crack Model is able to describe the flexural behaviour of a hybrid reinforced concrete beams, characterized by a rectangular cross section, an edge crack, and subjected to an applied bending moment, M . The geometry of the model is shown in Figure 2.1, where b and h are the section thickness and the section depth, respectively; a is the initial crack depth; and h_i , $i = 1, \dots, n$ defines the position of the generic reinforcement. A normalized crack depth and a normalized position of generic reinforcement can be defined as:

$$\xi = \frac{a}{h} \quad (2.1)$$

$$\zeta_i = \frac{h_i}{h} \quad (2.2)$$

The number of fibres for each section is n , uniformly distributed in the ligament, with generic position h_i . The $m < n$ fibres crossing the crack are considered as active, whose bridging action is represented by the m reclosing forces, F_i , $i = 1, \dots, m$. The total number of fibres crossing the mid-span cross section is assumed as a deterministic quantity, calculated as:

$$n = \alpha V_f \frac{bh}{A_f} \quad (2.3)$$

where A_f is the cross-sectional area of the single fibre, V_f is the fibre volume ratio and α is the orientation factor. The latter is generally found by investigating the specimen fracture surfaces (manual counting, X-ray analysis), and calculated as the ratio between the actual number of fibres with respect to the theoretical one.

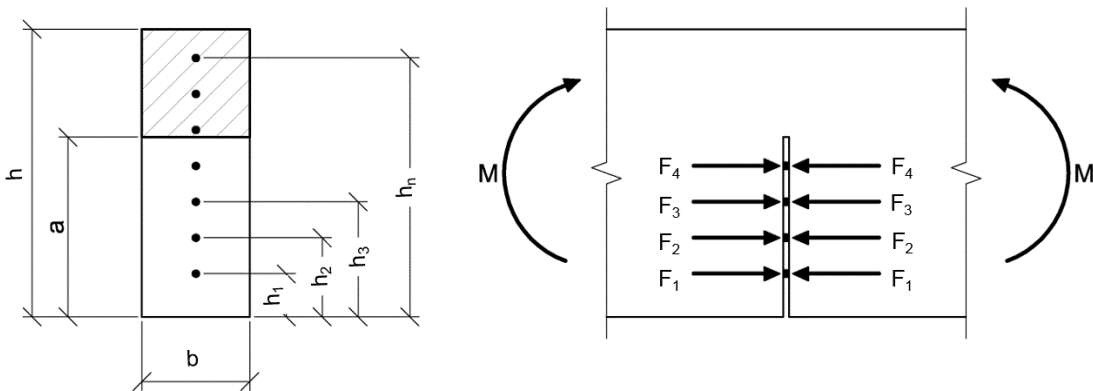


Figure 2.1 Theoretical scheme of the discontinuous model

Within the Bridged Crack Model, the fracture process zone of HRC beams is considered sufficiently small, since it is confined to the interspace between two subsequent fibre reinforcements. Under these circumstances,

the concepts of Linear Elastic Fracture Mechanics are fully applicable: the concrete matrix is assumed linear elastic-perfectly brittle, both in traction and in compression, characterized by the Young's modulus, E , and its fracture toughness, K_{IC} . The fibres are considered as uniformly distributed in the matrix, their orientation is assumed orthogonal with respect to the faces of the crack and the embedded length is considered the same for all the fibres. In Figure 2.2 it is showed the difference between the fibre distribution assumed in the model, and the actual one. Further developments of the model could randomize the position and orientation of the fibre, considering these quantities as stochastic variables.

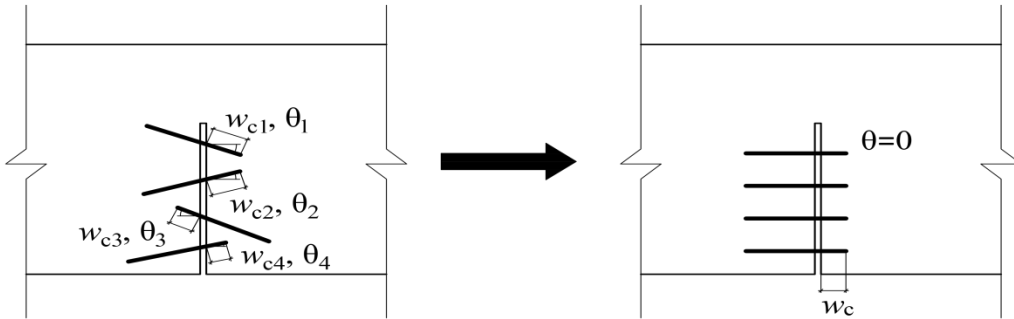


Figure 2.2 From real to model fibre distribution.

The bridging action depends by the position and orientation of the fibres. Considering the model distribution, instead, the bridging action is related only to the crack opening displacement along the crack faces at the fibre level, w_i ; there is no more reclosing force when the crack opening displacement is equal to the embedded length. The relationship among the reclosing force and w_i , namely *slippage constitutive law* or *bridging law*, can be obtained from experimental tests or micromechanical models and will be discuss in the paragraph 2.2.4. Instead, for what concern the reinforcement bars, their position is known, they are positioned at a distance equal to the concrete cover from the bottom edge of the cross section.

2.2.2 Stress Intensity Factor

The model assumes the crack propagation condition in according to LEFM, Eq. (2.4), considering only the Mode I opening, that occurs when the stress-intensity factor, K_I , reaches its critical value, K_{IC} :

$$K_I = K_{IC} \quad (2.4)$$

The value of the stress intensity factor at the crack tip is obtained, by means of the superposition principle, taking into account the two opposite contributes, due to bending moment and to the reclosing forces:

$$K_I = K_{IM} - \sum_{i=1}^m K_{Ii} \quad (2.5)$$

As regard the first contribute, considering a simply cracked bended strip, represented in Figure 2.3, Tada et al. (1985) found the following expression:

$$K_{IM} = \frac{M}{h^{1.5}b} Y_M(\xi) \quad (2.6)$$

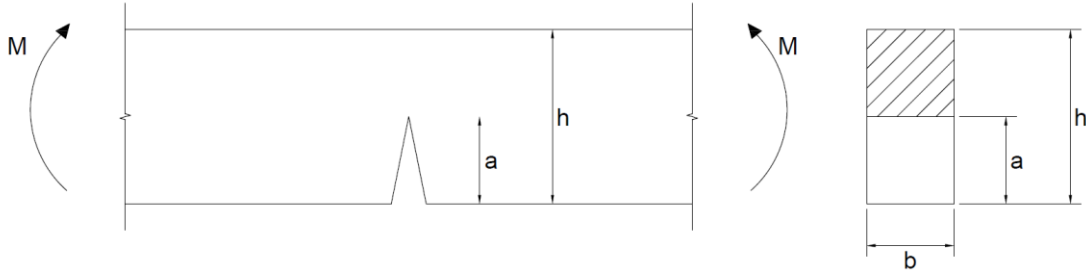


Figure 2.3 Simply cracked bended strip.

Considering the same geometry, the stress intensity factor due to a concentrated force, applied on the crack face (Figure 2.4), is given by:

$$K_{IF} = \frac{F}{h^{0.5}b} Y_F(\xi, \zeta) \quad (2.7)$$

It is possible to find the fracturing moment, by means of the Eq. (2.4), substituting the expressions of the stress intensity factor reported in Eq. (2.6) and Eq. (2.7). The scalar product of vectors is used for the summation, so the crack propagation condition becomes:

$$K_I = \frac{M}{h^{1.5}b} Y_M - \frac{\{Y_F\}^T \{F\}}{h^{1.5}b} \quad (2.8)$$

The value of the fracture moment is:

$$M_F = \frac{h^{1.5}b}{Y_M} \left(K_{IC} + \frac{\{Y_F\}^T \{F\}}{h^{\frac{1}{2}}b} \right) = \frac{h^{1.5}b}{Y_M} K_{IC} + \frac{h}{Y_M} \{Y_F\}^T \{F\} = R_1 + R_2 \{Y_F\}^T \{F\} \quad (2.9)$$

where R_1 and R_2 are used to reduce the expression of the fracture moment.

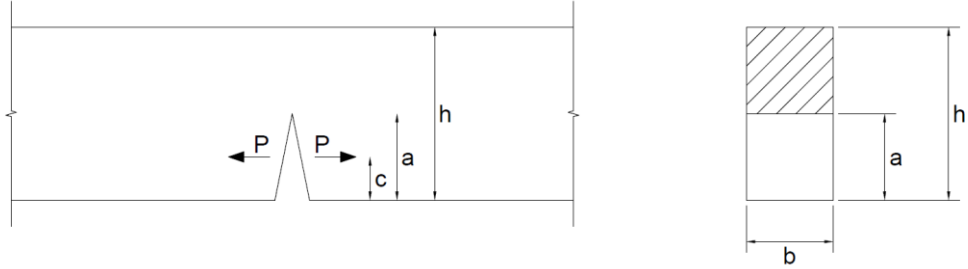


Figure 2.4 Simply cracked strip with concentrated forces.

In Eq. (2.10) and Eq. (2.11), two shape functions, Y_M and Y_F :

$$Y_M(\xi) = \begin{cases} 6(1.99\xi^{0.5} - 2.47\xi^{1.5} + 12.97\xi^{2.5} - 23.17\xi^{3.5} + 24.8\xi^{4.5}) & \xi \leq 0.6 \\ 3.99(1-\xi)^{-1.5} & \xi > 0.6 \end{cases} \quad (2.10)$$

$$Y_F(\xi, \zeta) = \frac{2}{\sqrt{\pi\xi}} \frac{1}{(1-\xi)^{1.5} \sqrt{1 - \left(\frac{\zeta_i}{\xi}\right)^2}} G(\xi, \zeta_i) \quad (2.11)$$

$$G(\xi, \zeta_i) = g_1(\xi) + g_2(\xi) \frac{\zeta_i}{\xi} + g_3(\xi) \left(\frac{\zeta_i}{\xi}\right)^2 + g_4(\xi) \left(\frac{\zeta_i}{\xi}\right)^3 \quad (2.12)$$

$$g_1(\xi) = 0.46 + 3.06\xi + 0.84(1-\xi)^5 + 0.66\xi^2(1-\xi)^2 \quad (2.13)$$

$$g_2(\xi) = -3.52\xi^2 \quad (2.14)$$

$$g_3(\xi) = 6.17 - 28.22\xi + 34.54\xi^2 - 14.39\xi^3 - (1-\xi)^{1.5} - 5.88(1-\xi)^5 - 2.64\xi^2(1-\xi)^2 \quad (2.15)$$

$$g_4(\xi) = -6.63 + 25.16\xi - 31.04\xi^2 + 14.41\xi^3 + 2(1-\xi)^{1.5} + 5.04(1-\xi)^5 + 1.98\xi^2(1-\xi)^2 t \quad (2.16)$$

It is worth noting that the shape function related to the bending moment, Eq. (2.10), is a function of the normalized crack depth. On the other hand, the shape function introduced for the concentrated force, Eq. (2.11), depends also on the normalized reinforcement position, and it provides a singularity for $\xi = \zeta_i$ (this singularity will be discussed in the next chapter).

2.2.3 Compatibility equation

The compatibility conditions are applied to solve the statically indeterminate problem, i.e., to evaluate the bridging forces, for a given crack depth, depending on the applied bending moment. The crack opening displacements vector is defined as:

$$\{w\} = \{w_1, \dots, w_m\}^T \quad (2.17)$$

where w_i is the crack opening displacement at the level of the i -th fibre, obtained by applying the superposition principle on the two opposite contributes. The vector of the reactions of the m active fibres is defined as:

$$\{F\} = \{F_1, \dots, F_m\}^T \quad (2.18)$$

The vector of the local compliance due to the bending moment is defined as:

$$\{\lambda_M\} = \{\lambda_{1M}, \dots, \lambda_{mM}\}^T \quad (2.19)$$

The mathematical problem consists in the determination of the crack opening displacements and the reinforcement actions, for each reinforcement level. By using the superposition principle, these quantities can be described by the following relationship:

$$\{w\} = \{\lambda_M\}M - [\lambda]\{F\} \quad (2.20)$$

where the minus sign is due to the crack-closure action exerted by the active reinforcement; $[\lambda]$ is the $m \times m$ matrix of the local compliances due to the bridging action, and it is symmetric for Betti's theorem.

Eq. (2.18) describe a linear system of m equations, and $2m$ unknowns, i.e., the bridging forces F_i , and the corresponding crack opening displacements, w_i . The solution of the system requires other m conditions. The m missing conditions are given by the constitutive laws introduced above. i.e. by a link between the force and the accompanying opening at the level of each reinforcement.

Previously, considering a rigid-perfectly plastic behavior for the reinforcements, the crack resulted to be closed until the ultimate force $F_{P,i}$ is reached. Now, with the introduction of a new elastic-perfectly plastic constitutive laws for the reinforcements (these will be described in the next paragraph), the reactions are determined with an iterative process until the convergence is reached.

We can recognize the bars that are active, n_b and the fibres that are still bridging the crack faces, $n_{f,c}$, from those whose bridging effect is exhausted, $n_{f,s}$: in all cases, the condition $m = n_b + n_{f,c} + n_{f,s}$ must be satisfied. In matrix form they can be portioned as follows:

$$\begin{pmatrix} w_b \\ w_{f,c} \\ w_{f,s} \end{pmatrix} = \begin{pmatrix} \lambda_{Mb} \\ \lambda_{Mf,c} \\ \lambda_{Mf,s} \end{pmatrix} M - \begin{bmatrix} \lambda_{bb} & \lambda_{bf,c} & \lambda_{bf,s} \\ \lambda_{f,cb} & \lambda_{f,cf,c} & \lambda_{f,cf,s} \\ \lambda_{f,sb} & \lambda_{f,sf,c} & \lambda_{f,sf,s} \end{bmatrix} \begin{pmatrix} F_b \\ F_{f,c} \\ F_{f,s} \end{pmatrix} \quad (2.21)$$

Unlike in the previous case, we have both kinematic and static unknowns, since both crack opening displacements, w_i , and bridging forces, F_i , must be determined. Again, the problem requires $m=(b+f,c+f,s)$ as an additional condition, which consists in:

$$b: \quad F_i = F(w_i) \quad (2.22a)$$

$$f, c: \quad F_i = F(w_i) \quad (2.22b)$$

$$f, s: \quad F_i = 0 \quad (2.22c)$$

where $F(w_i)$ is the force of the i -th fiber, evaluated by the slippage constitutive law adopted for the reinforcing phase. The expressions of the Eq. 2.22 will be discussed in the next paragraph.

2.2.4 Constitutive Laws

Fibres and reinforcement bars represent the secondary phase of the HRC composite material. The mechanical and geometrical properties of the reinforcement are fundamental to provide the synergism with the concrete matrix, which make the material an effective composite. The bars are usually straight and they could vary their diameter or yielding resistance. The fibres are variable, both for material and geometry. They can be made of steel, polymeric materials as well as inorganic materials such as carbon, glass and natural materials (CNR, 2006). Moreover, the shape of the fibre can be undeformed (straight), with a round or flat section; there are also fibers with deformed profile, such as twisted or with hooked end. In Figure 2.5 different types of fibres are showed.

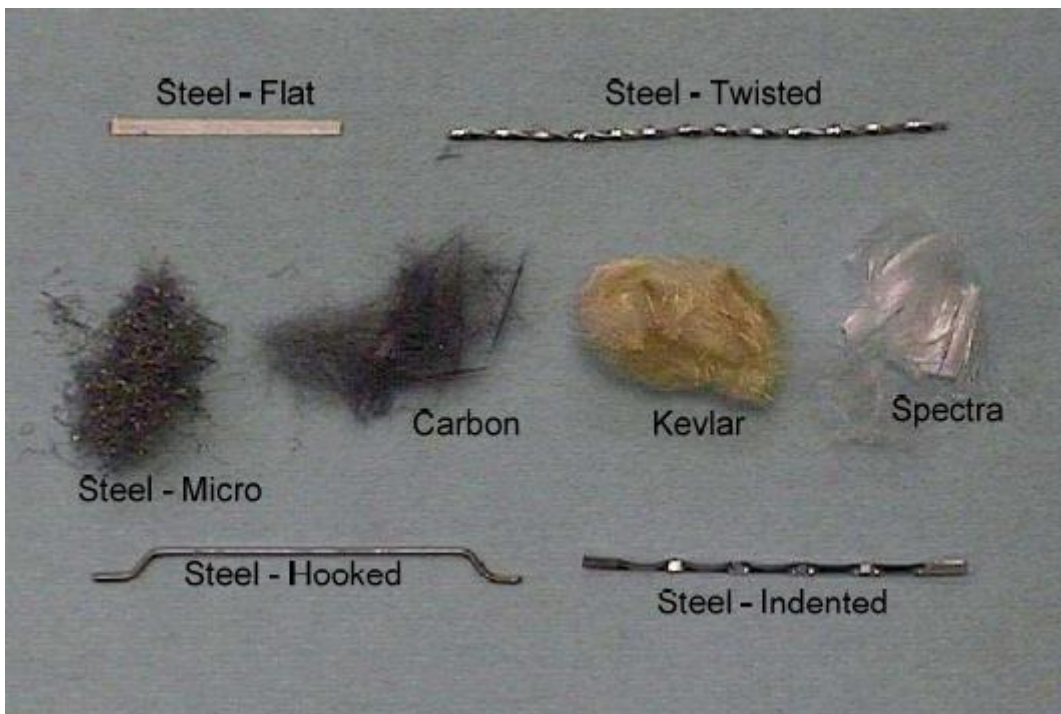


Figure 2.5 Different type of fibres (Figure from Naaman, 2008).

Fibre pull-out tests measure the force required to pull out a fibre, embedded in a matrix, when it is subjected to uniaxial tension. These tests can be carried out applying the tensile force in one side or in double side; they can be also performed on a single fibre or in a multiple configuration.

This work is focused on steel fibres, particularly on the straight and the hooked-end ones (Figure 2.6).

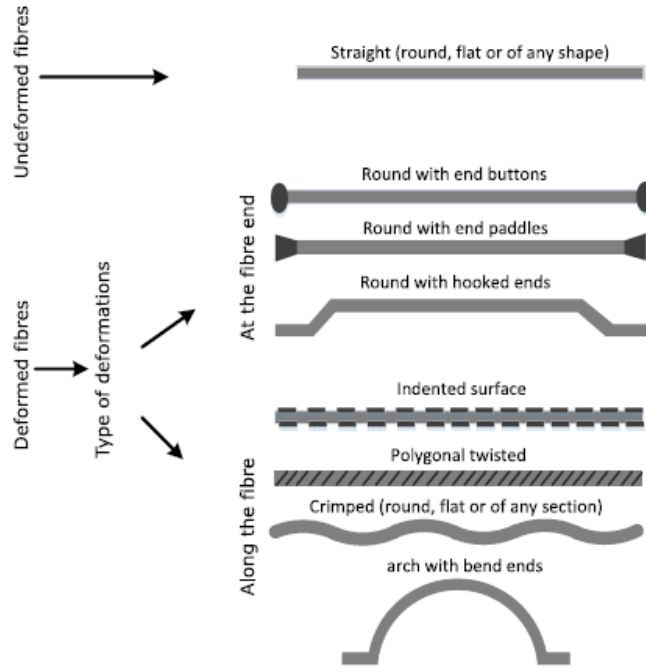


Figure 2.6 Different geometric shape of steel fibres (Figure from Abdallah, 2018).

A scheme of the slippage phenomenon, occurring during a typical pull-out test, is represented in Figure 2.7, where a fibre, embedded for a length l in a cementitious matrix, is subjected to a tensile force P . Once debonding occurs along the entire embedded length of the fibre, a progressive slippage of the fibre into the matrix occurred, with the consequent distribution of tangential stresses, mobilized at the fibre-matrix interface.

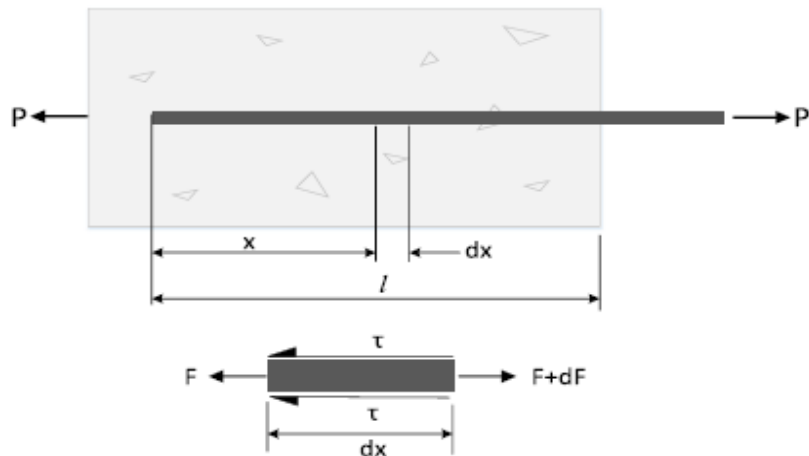


Figure 2.7 Free-body diagram of an element of fibre (data from Naaman et al., 1991b).

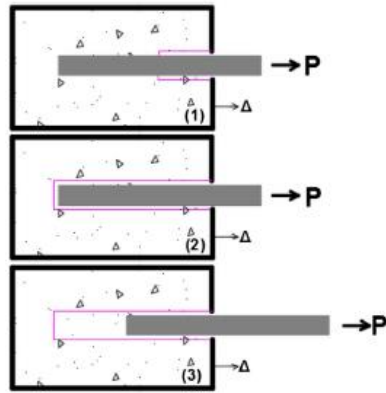


Figure 2.8 Pull-out behaviour of straight fibre (Stages 1-3).
(Figure from Abdallah, 2018).

More complex mechanisms are exhibited in pull-out tests by deformed shape of fibre (Figure 2.6). The hooked-end type is the most commonly employed, because these fibres are able to further enhance the energy absorption during the pull-out process. For this type of geometry, indeed, the pull-out mechanism provides other two additional stages, due to the development of two plastic hinges (PH1 and PH2) correspondingly to the end deformed region (Figure 2.9).

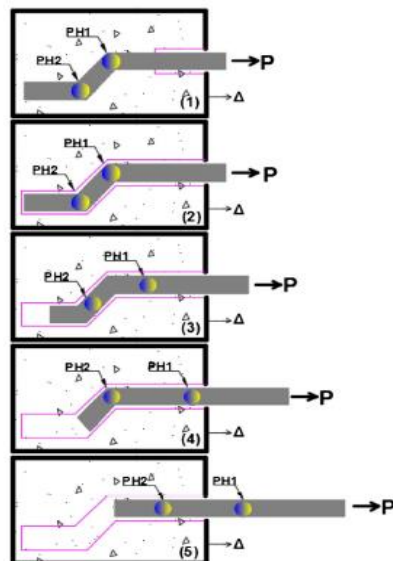


Figure 2.9 Pull-out behaviour of hooked-end fibre (Stages 1-5).
(Figure from Abdallah, 2018).

The difference between the two typical pull-out responses can be evaluated in Figure 2.10. The curves show the same elastic range, after which the straight fibre experiences the exponential decay, as previously described. On the contrary, the hooked-end fibre reaches a higher value of the pull-out force, due to the mechanical anchorage of the fibre end. After this maximum, the pull-out load starts to decrease due to the progressive mobilization of the PH1. When the first plastic hinge has straightened the fibre, it is placed in the straight part of the channel. Further straightening under PH2 is recognized in the slight increase in pull-out load

at Stage 4 (Abdallah, 2018). Finally, when both the hooked-end are straightened, the fibre has reached the straight configuration, and the same exponential decay is found.

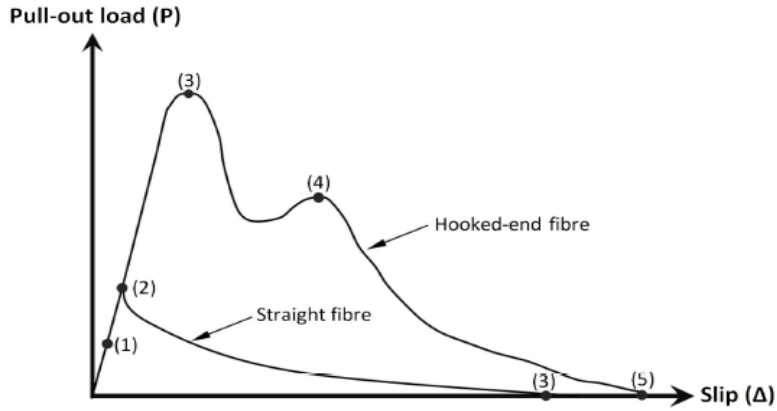


Figure 2.10 Pull-out response of straight fibre (Stages 1-3) and hooked-end fibre (Stages 1-5).

Moreover, the influence of fibre orientation and matrix strength, for hooked-end type, is extensively investigated by Robins et al. (2002) and Cunha et al. (2010). The results of the experimental researches suggest that: (i) increasing the matrix strength, and the embedded length, the critical value of the pull-out force increases; (ii) the embedded length must be greater than the hooked length to guarantee the employment of the mechanical anchorage; (iii) an inclination of 10-20 degrees provides the maximum value of energy absorption. Despite this, the inclination of the fibres is not taken into account in the model.

In order to define an analytical bridging-law, both for straight and hooked-end steel fibres, the experimental results obtained by Abdallah et al. (2019) are analysed.

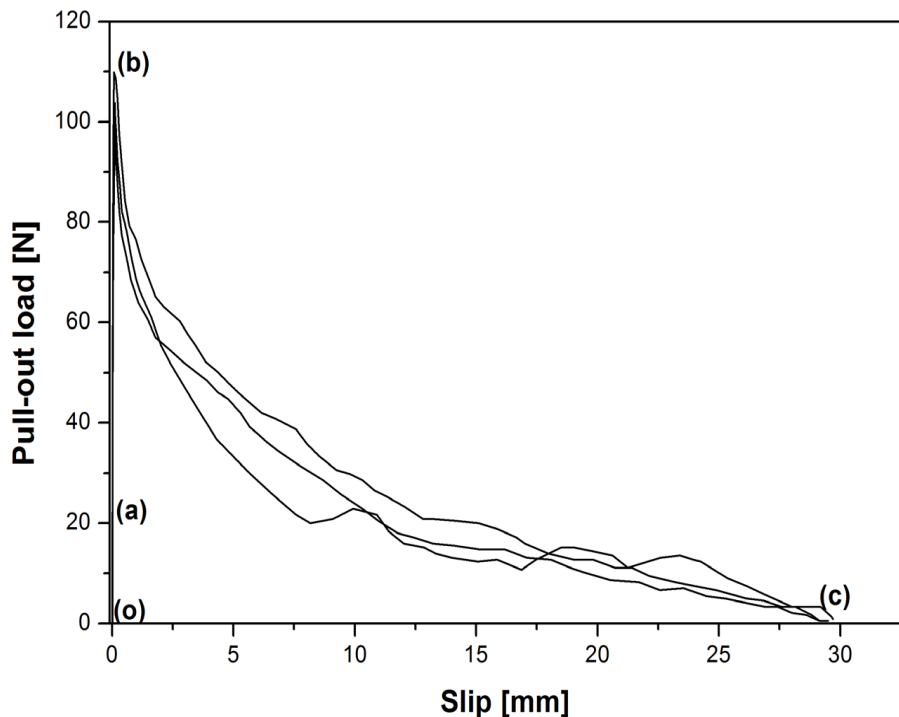


Figure 2.11 Pull-out tests on straight steel fibre results. (Abdallah, 2019).

In all the tests, can be recognized three different stages:

1. *Elastic range*
2. *Partial debonding stage*
3. *Fully debonded and frictional pull-out stage*

The average of the results is normalized: the load respect to the maximum pull-out force, $F_P = 110$ N, the slip respect to the fibre embedded length, $w_c = 30$ mm. This normalization provides the so-called slippage law per “unit embedded length” of the fiber. By the graphical analysis of the normalized experimental data, the function in Figure 2.14 is thus obtained. The corresponding analytical formulation is defined as follow:

1. For $0 < \frac{w_i}{w_c} < 2 \times 10^{-3}$

$$\frac{F_i}{F_P} = \frac{\frac{w_i}{w_c}}{2 \times 10^{-3}} \quad (2.23)$$

2. For $2 \times 10^{-3} < \frac{w_i}{w_c} < 1$

$$\frac{F_i}{F_P} = e^{-5.204\left(\frac{w_i}{w_c}\right)} \quad (2.24)$$

3. For $\frac{w_i}{w_c} \geq 1$

$$\frac{F_i}{F_P} = 0 \quad (2.25)$$

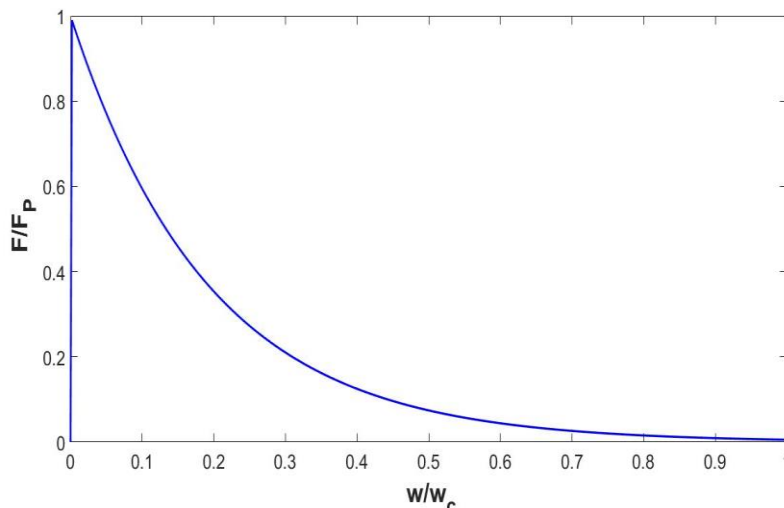


Figure 2.12 Normalized pull-out curve of straight steel fibre adopted in the Bridged Crack model.

The pull-out of straight fibre is reproduced using an exponential decay law after the peak load.

The same procedure is conducted for the hooked-end steel fibres; experimental pull-out tests results (Abdallah, 2019) are represented in Figure 2.15.

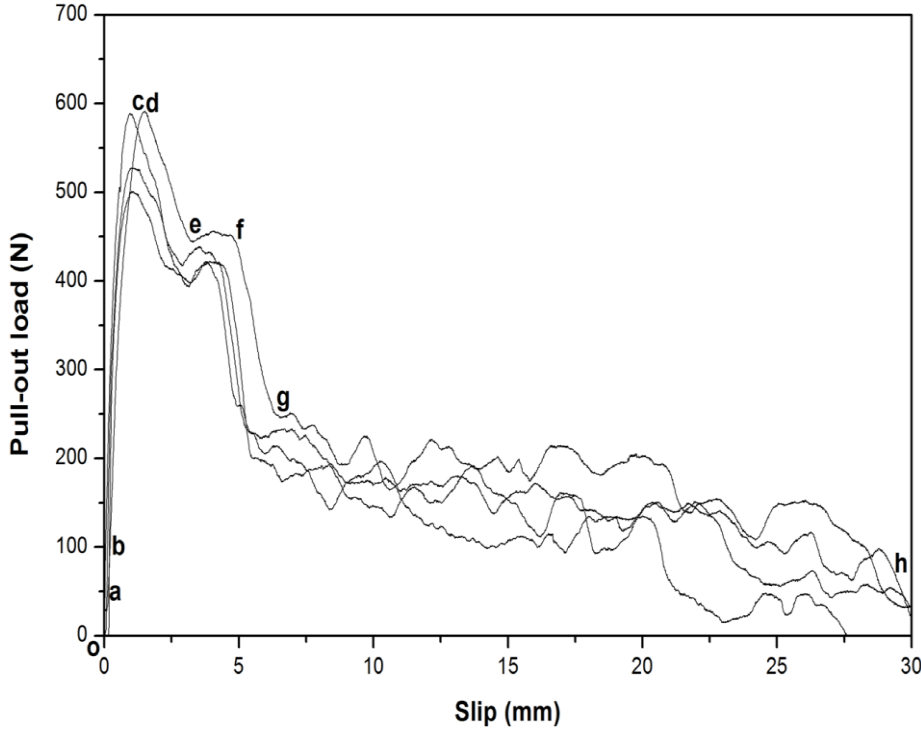


Figure 2.13 Pull-out tests on hooked-end steel fibre results. (Abdallah, 2019)

Also in this case, the experimental curves show the typical phases connected to the hooked-end fibre geometry. Particularly, it is remarkable the effect of the two plastic hinges correspondently to the c-d, and e-f curve's range. By the graphical analysis of the normalized experimental data, the function in Figure 2.16 is thus obtained. The corresponding analytical formulation is defined as follow:

1. For $0 < \frac{w_i}{w_c} < 0.03$

$$\frac{F_i}{F_p} = \frac{\frac{w_i}{w_c}}{0.03} \quad (2.26)$$

2. $0.03 < \frac{w_i}{w_c} \leq 0.05$

$$\frac{F_i}{F_p} = 1 \quad (2.27)$$

3. For $0.05 < \frac{w_i}{w_c} < 0.1$

$$\frac{F_i}{F_p} = 1 - 4 \left(\frac{w_i}{w_c} - 0.05 \right) \quad (2.28)$$

4. For $0.1 \leq \frac{w_i}{w_c} \leq 0.15$

$$\frac{F_i}{F_p} = 0.8 \quad (2.29)$$

5. For $0.15 < \frac{w_i}{w_c} \leq 0.18$

$$\frac{F_i}{F_p} = 1 - 13.33 \left(\frac{w_i}{w_c} - 0.15 \right) \quad (2.30)$$

6. For $0.18 < \frac{w_i}{w_c} < 1$

$$\frac{F_i}{F_p} = 0.4 \cdot e^{-5.204 \left(\frac{w_i}{w_c} - 0.18 \right)} \quad (2.31)$$

7. For $\frac{w_i}{w_c} \geq 1$

$$F_i = 0 \quad (2.32)$$

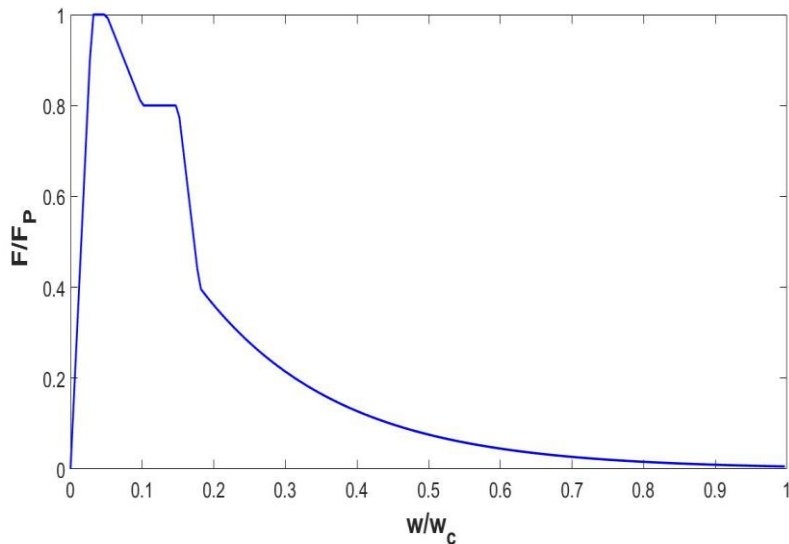


Figure 2.14 Normalized pull-out curve of hooked-end steel fibres adopted in the Bridged Crack Model.

The pull-out response of the hooked-end is analytically reproduced taking into account the experimental peculiarity: the effect of the plastic hinges is considered through the insertion of the two plateaus.

These two constitutive slippage laws are currently implemented in the algorithm of the Bridged Crack Model, since steel straight and hooked-end steel fibres are the most commonly employed in practical applications. Instead for what concern the reinforcement steel rebars, an elastic-perfectly plastic constitutive law was used. There is a first elastic stage where the reaction grows linearly with the crack opening displacement. The value F_p is reached when $w_i = w_y$ and after this point there is the perfectly plastic stage, in which the reaction remains constant without a decay after the peak load. The value of w_y is identified by the analysis of the experimental campaigns and depends by several aspect: Bar's diameter, adhesion phenomena between concrete and bars, bar's length and concrete strength. Moreover, the model does not consider the possible rupture (breakage) of the reinforcement bars. If necessary, it should be taken into account by estimating a value w_c , at which the action of the bar suddenly ceases. The corresponding analytical formulation is defined as follow:

1. For $0 < w_i < w_y$

$$\frac{F_i}{F_p} = \frac{w_i}{w_y} \quad (2.33)$$

2. For $w_i \geq w_y$

$$\frac{F_i}{F_p} = 1 \quad (2.34)$$

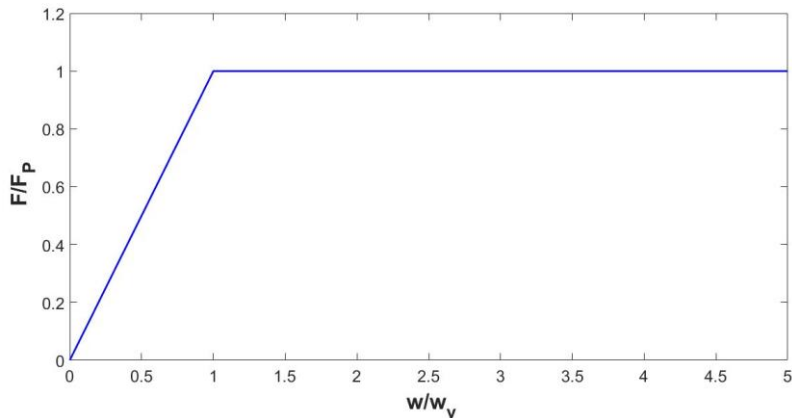


Figure 2.15 Normalized constitutive law of steel bars adopted in the Bridged Crack Model.

2.2.5 Moment rotation response and dimensionless number

For a given crack depth, a , and a given applied bending moment, M , the related bridging forces have been evaluated. Also the localized rotation of the cracked cross section can be calculated. In matrix form:

$$\varphi = \lambda_{MM} M - \{\lambda_M\}^T \{F\} \quad (2.35)$$

When the fracture moment is achieved the crack depth increases, and the same calculations, regarding fracture moment and localized rotation are required for each crack advancement.

In this way the Crack Length Control Scheme (CLCS) allows to describe the sectional response in terms of moment vs localized rotation. From these results, it is also possible to evaluate the load vs deflection response of the beam, taking into account also the elastic displacement of the beam midspan.

The conversion from $M - \varphi$ to $P - \delta$ response, for three-point bending test (TPBT) and four-point bending test (FPBT), is developed starting from the simple schemes of Figures 2.16 and 2.17.

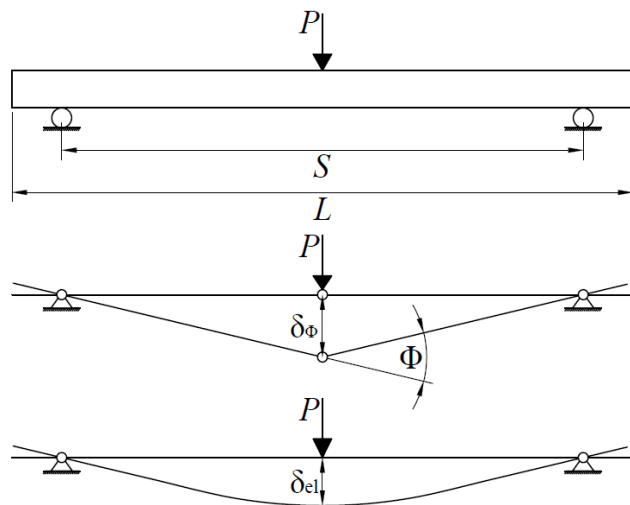


Figure 2.16 Evaluation of the beam displacement in case of three-point bending test.

(a) Test with loaded point deflection control (b) Test with midspan deflection control

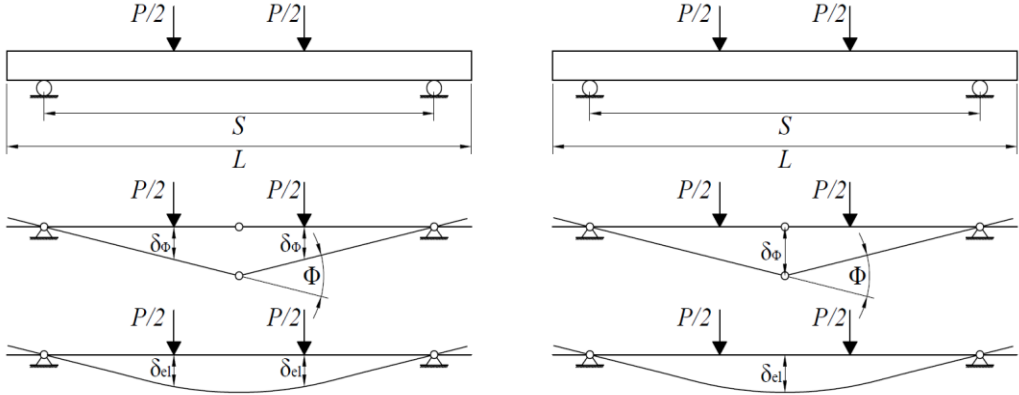


Figure 2.17 Determination of the beam displacement in case of four-point bending test.

For each crack length, the localized rotation of the notched cross-section can be calculated with Eq. 2.35. On the other hand, the global behaviour of the structural element, which is usually described in terms of the applied load vs mid-span deflection diagram, depends on the loading scheme. For instance, in the case of a three-point bending (TPB) test (fig. 2.16), the applied load, P , can be related to the internal bending moment as:

$$P = \frac{4M}{S} \quad (2.36)$$

The consequent total deflection of the beam element can be calculated taking into account both the contribution related to the damage localized in the mid-span cross-section and that related to the elastic deformation occurring in the remaining part of the beam. The former can be modelled as a non-linear hinge, whereas the latter refers to the elastic beam theory, as schematically represented in Fig. 2.16. During the crack propagation process, the first contribution becomes dominant, leading to a rigid-body motion of the two halves of the specimen rotating around the mid-span hinge. The application of the superposition principle leads to:

$$\delta = \delta_{el} + \delta_\phi = \frac{PS^3}{48EI} + \frac{\phi S}{4} \quad (2.37)$$

where S is the beam span, I the inertia of the cross section, and E the Young's Modulus.

Similar considerations can be drawn for the four-point bending test controlled by the loaded point deflection, Figure 2.17 scheme (a). The application points of the forces divide the beam span into three equal parts; with this supposition, the value of the load and the corresponding deflection is computed:

$$P = \frac{6M}{S} \quad (2.38)$$

$$\delta = \delta_{el} + \delta_\phi = \frac{23PS^3}{1296EI} + \frac{\phi S}{4} = \frac{23MS^2}{216EI} + \frac{\phi S}{4} \quad (2.39)$$

From a global point of view, the post-cracking regime is found to be governed by three dimensionless numbers, N_{Pb} , N_{Pf} and N_{w} , defined as follows:

$$N_{\text{Pb}} = \rho \frac{\sigma_y}{K_{\text{IC}}} h^{0.5} \quad (2.40)$$

$$N_{\text{Pf}} = \frac{\sum_{i=1}^n F_{\text{P},i}}{K_{\text{IC}} b h^{0.5}} = V_f \frac{\alpha \beta \bar{\sigma}_{\text{s,max}}}{K_{\text{IC}}} h^{0.5} = V_f \frac{\bar{\sigma}_{\text{s,max}}}{K_{\text{IC}}} h^{0.5} \quad (2.41)$$

$$N_{\text{w}} = \frac{E w_c}{K_{\text{IC}} h^{0.5}} \quad (2.42)$$

The *bars reinforcement brittleness number*, N_{Pb} , depends on the yield strength of the bars f_y , on the steel percentage area ρ , on the fracture toughness K_{IC} , and on the beam depth h .

The *fibres reinforcement brittleness number*, N_{Pf} , depends on the fibre volume fraction, V_f , on the maximum value of the generalized tensile stress acting within the reinforcing fibre, $\bar{\sigma}_{\text{s,max}}$ —in which the parameters of fibres distribution, α and β , are included—, on the matrix fracture toughness, K_{IC} , and on the beam depth, h . On the other hand, the *pull-out brittleness number* N_{w} depends on the matrix Young's modulus, E , on the equivalent embedded length of the fibre, w_c , on the matrix fracture toughness, K_{IC} , and on the beam depth, h . It is worth stress again that these three dimensionless numbers are scale-dependent.

3 Numerical Algorithm

3.1 Crack Length Control Scheme (CLCS)

The algorithm of the Bridged Crack Model is implemented in MATLAB language.

The initialization requires input parameters, which can be divided into the following groups:

- Beam geometry
 - $b \rightarrow$ section thickness
 - $h \rightarrow$ section depth
 - $a_0 \rightarrow$ initial crack depth (or $\xi_0 \rightarrow$ normalized initial crack depth)
 - $L \rightarrow$ beam length
 - $S \rightarrow$ beam span
- Steel bar geometry
 - $d_b \rightarrow$ bar diameter
 - $n_b \rightarrow$ number of bars
- Fibre geometry
 - $d_f \rightarrow$ fibre diameter
 - $l_f \rightarrow$ fibre length
 - $V_f \rightarrow$ fibre volume fraction
 - $\rho \rightarrow$ fibre specific weight
 - $c_1 \rightarrow$ position of the first fiber (or $\zeta_{\min} \rightarrow$ normalized position)
 - $c_n \rightarrow$ position of the last fiber (or $\zeta_{\max} \rightarrow$ normalized position)
 - $w_c \rightarrow$ average embedded length of the fiber
- Concrete mechanical properties
 - $E \rightarrow$ matrix Young's modulus
 - $K_{IC} \rightarrow$ matrix fracture toughness
 - $f_{ck} \rightarrow$ matrix characteristic cylindrical compression strength

- Steel bar material
 - f_y → bar yielding strength
 - w_y → opening crack displacement at which the bar is yielded.
- Fibre material
 - f_u → fibre ultimate tensile strength
 - σ_s → fibre slippage strength
- Process control
 - a_{\max} → final crack depth (or ξ_{\max} → normalized final crack depth)
 - $\Delta\xi$ → normalized crack depth increment at each calculation step
 - n → number of fibres modelling
 - $toll$ → iteration tolerance

The actual number of fibres is evaluated through the Eq. (2.3). However, it can be really high, affecting the computation time. To avoid this problem, the input data include the fibres number; the numerical code is able to define an equivalent bridging force in order to guarantee the equivalence between the two distributions. The effect of different numbers of fibres modelling regards the local phenomenon, whereas the global response remains unchanged.

As seen in Chapter 2, the fibres are considered evenly spaced in the entire ligament, between c_1 and c_n (Figure 2.1). The constitutive law is defined, on the basis of the type of reinforcement. For straight and hooked-end steel fibres and for steel rebars the bridging laws implemented are illustrated in section 2.2.4.

After the input data initialization, at each k -th step the crack depth is increased as follow:

$$\xi^{(k+1)} = \xi^{(k)} + \Delta\xi \quad (3.1)$$

where the apex (k) indicates the generic calculation step.

The fibre is defined active if:

$$\zeta_i < \xi^{(k)} \quad (3.2)$$

The algorithm is based on the following steps:

1. Data initialization;
2. Actual crack depth. At the first step it is assumed equal to a_0 ;
3. Compute the m active fibres;
4. Compute compliances;
5. Initialize n_c and n_f . At the first step, it is assumed $n_c = m$, $n_f = 0$;
6. Initialize $\{w_{old}\}$. At the first step, it is assumed $\{w_{old}\} = 0$.
7. Computed the m bridging actions $\{F\}$

7.1. loop entering conditions:

If $F_i > F_p$ or $F_i < -F_p$, $\rightarrow F_i = F_p$;

Update n_c and n_f , and return to step 7.

8. Compute the m crack opening displacements $\{w\}$, with Eq. (2.21).

8.1. loop entering condition:

If $w_i < w_{old,i}(1 - toll)$ or $w_i > w_{old,i}(1 + toll)$

If $F_i \neq F(w_i)$, $\rightarrow F_i = F(w_i)$;

Update n_c , n_f , F_i

Save $w_{old,i} = w_i$ and return to step 3.

9. Compute localized rotation of the cracked cross-section, φ , with Eq. (2.35);
10. Compute crack propagation moment, M_F , with Eq. (2.9);
11. Save results: $M_F, \{w\}, \{F\}, \varphi$
12. Update crack depth, $\xi^{(k+1)} = \xi^{(k)} + \Delta\xi$ and return to step 2 if $\xi^{(k+1)} < \xi_{max}$.
13. Computation of TPBT or FPBT force and the corresponding deflection, with Eq. from (2.36) to (2.39)

The process is thus controlled by increasing the crack length (Crack Length Control Scheme). Using this technique, the discontinuous phenomena characterizing the post-cracking response, i.e., snap-back and snap-through instabilities are described by the model, as extensively discussed by Carpinteri and Accornero (2019).

3.2 Numerical errors

The predicted response is affected by distance between the crack tip and the closest active fibre. This issue is due to the shape function $Y_F(\xi, \zeta_i)$ (Eq. 2.9), that provides a singularity for $\xi = \zeta_i$. In order to avoid this problem, the following conditions are imposed in the numerical code:

$$\Delta\xi = 0.005 \quad (3.3)$$

$$\xi - \zeta_i > 0.05\Delta\xi \quad (3.4)$$

Typical examples of numerical problems related to the crack depth increment, $\Delta\xi$, are shown in Figure 3.1 and Figure 3.2. The curves are obtained imposing the same mechanical and geometrical parameters, but different values of $\Delta\xi$. Particularly, in the first case (Figure 3.1), the peak is the consequence of a too low $\Delta\xi$ (0.0005). On the other hand, the second picture is found using a too high $\Delta\xi$ value (0.05), so the peak is too low that cannot be recognizable. A more realistic solution is obtained when the value of Eq. (3.3) is adopted, and the corresponding result is shown in Figure 3.3.

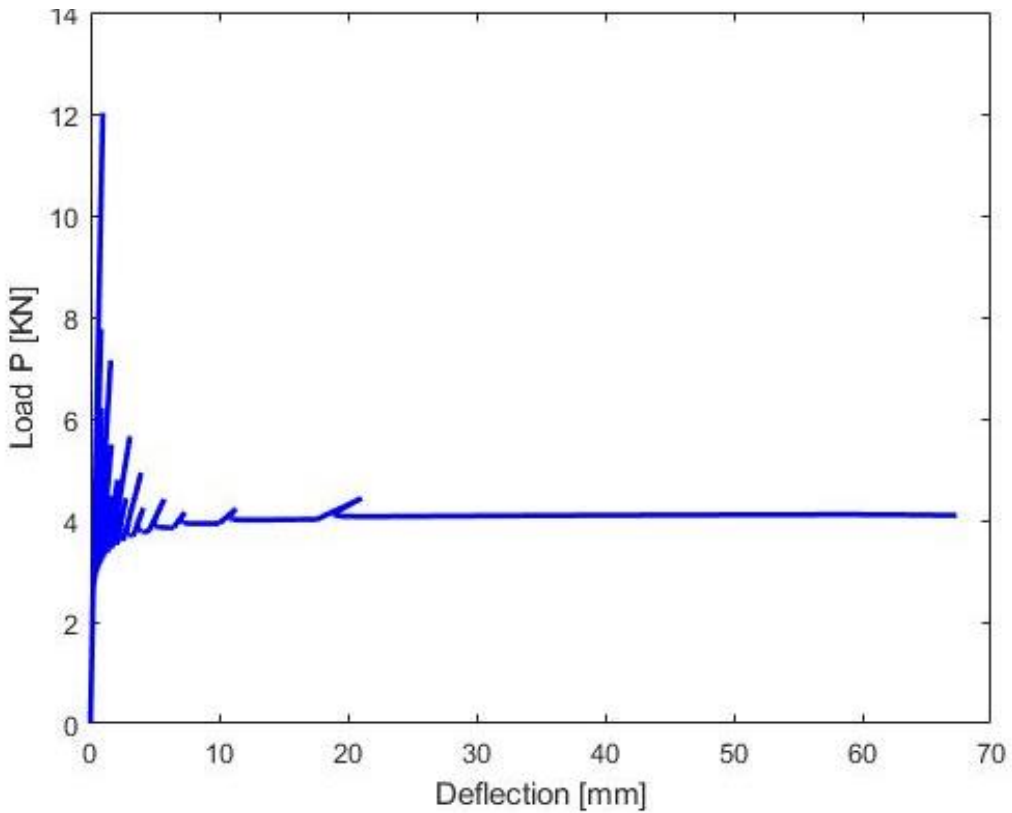


Figure 3.1 Load deflection curve obtained with a value of $\Delta\xi = 0.0005$.

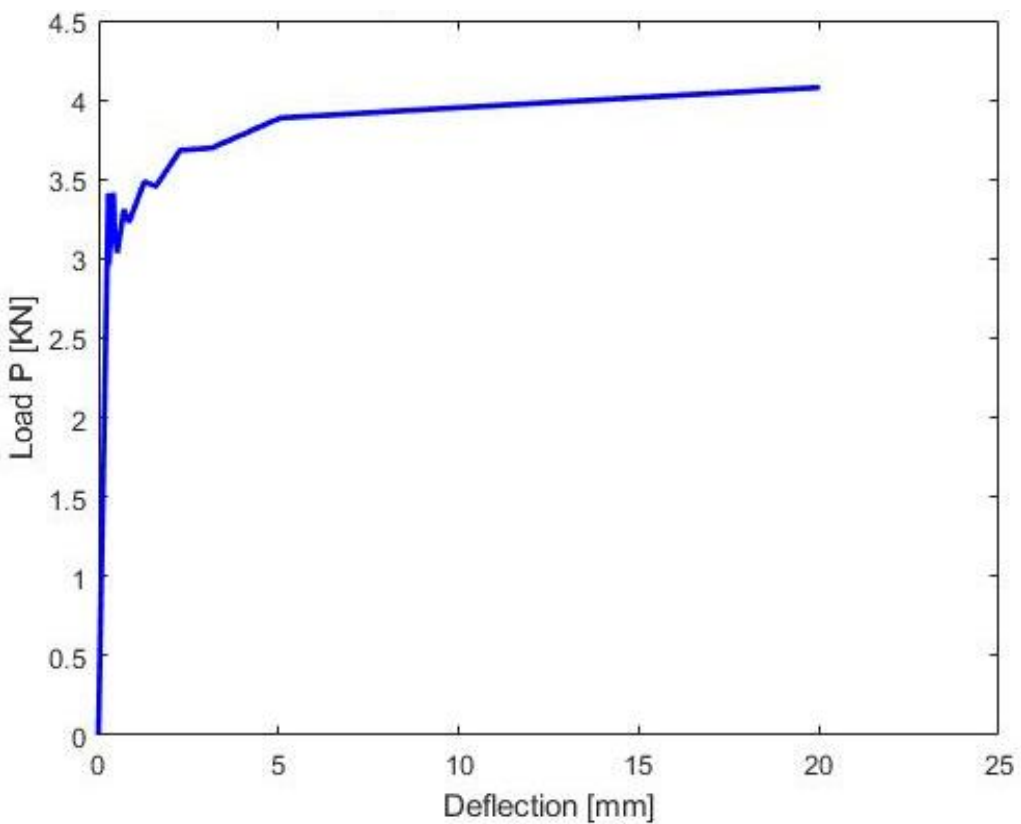


Figure 3.2 Load deflection curve using the value of $\gamma = 0.05$.

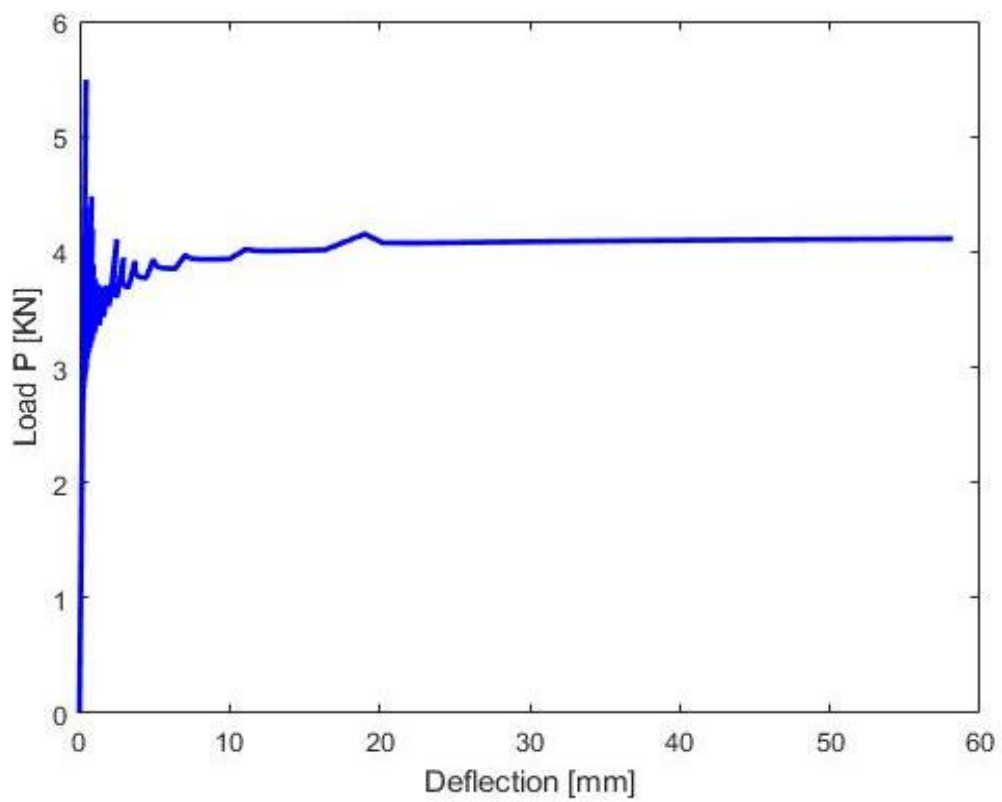


Figure 3.3 Load deflection curve using the value of $\gamma = 0.005$.

3.3 Number of fibres

Another input parameter that influences the predicted $M - \varphi$ response is the number of fibres, n . Using a low number of n , the reaction generated by the fictitious fibres is considerably greater than that which occurs in the real fibres. This, combined with the fact that shape function $Y_F(\xi, \zeta_i)$ (Eq. 2.11) returns high values if the edge of the crack is very close to one of the fictitious fibres, can lead to local high load peaks when the opening crack crosses one of the fibres, even if the global response remains the same. Especially, the post cracking response deviates from the real one, showing an abnormal peak, as is shown in Figure 3.4. These aspects can be improved by increasing the number of fibres, n , approaching the theoretical number of fibers predicted by Eq. 2.3.

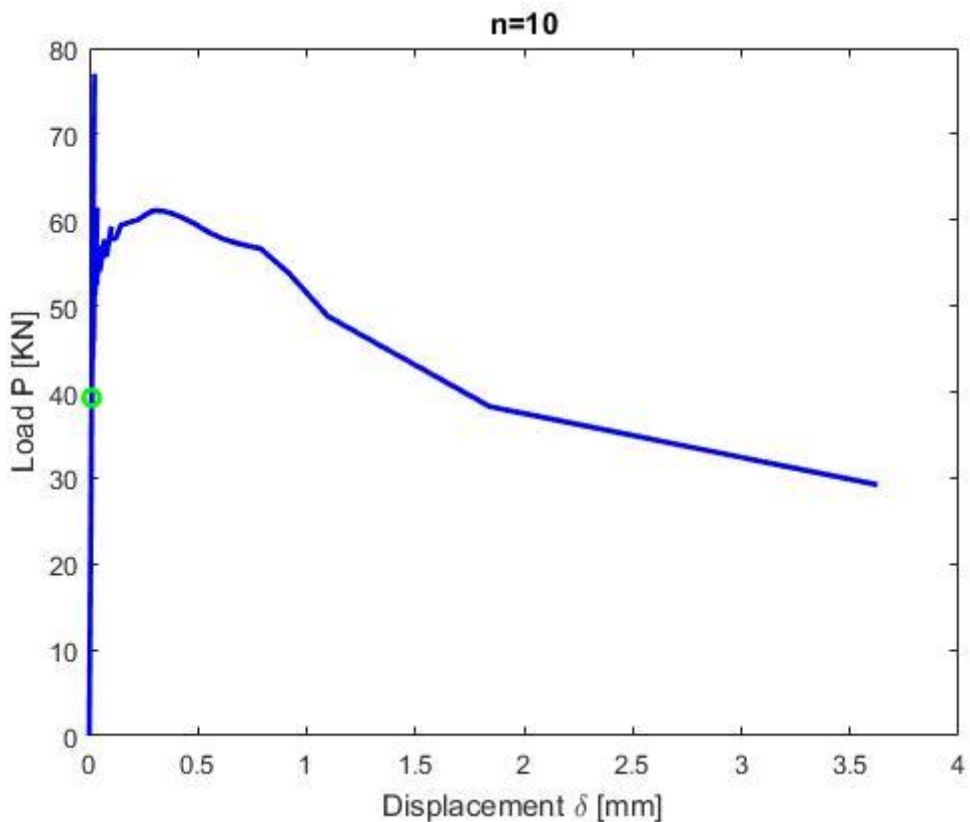


Figure 3.4 Load deflection curve using a low number of fibres, $n = 10$

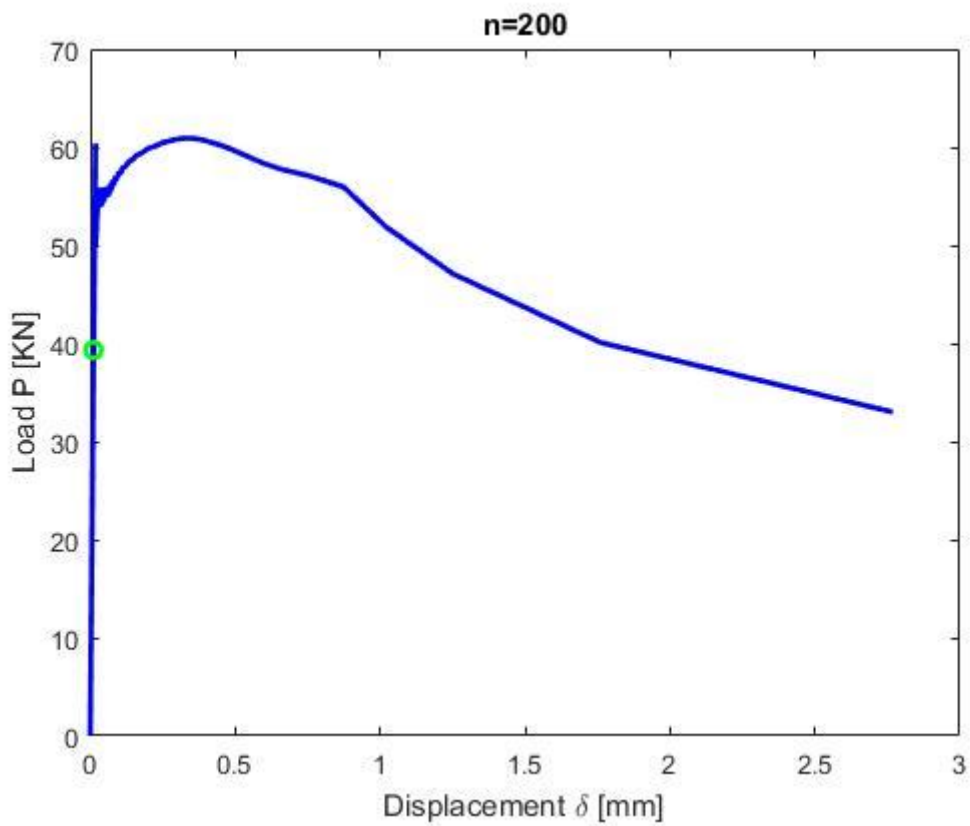


Figure 3.5 Load deflection curve using an high number of fibres, $n = 200$

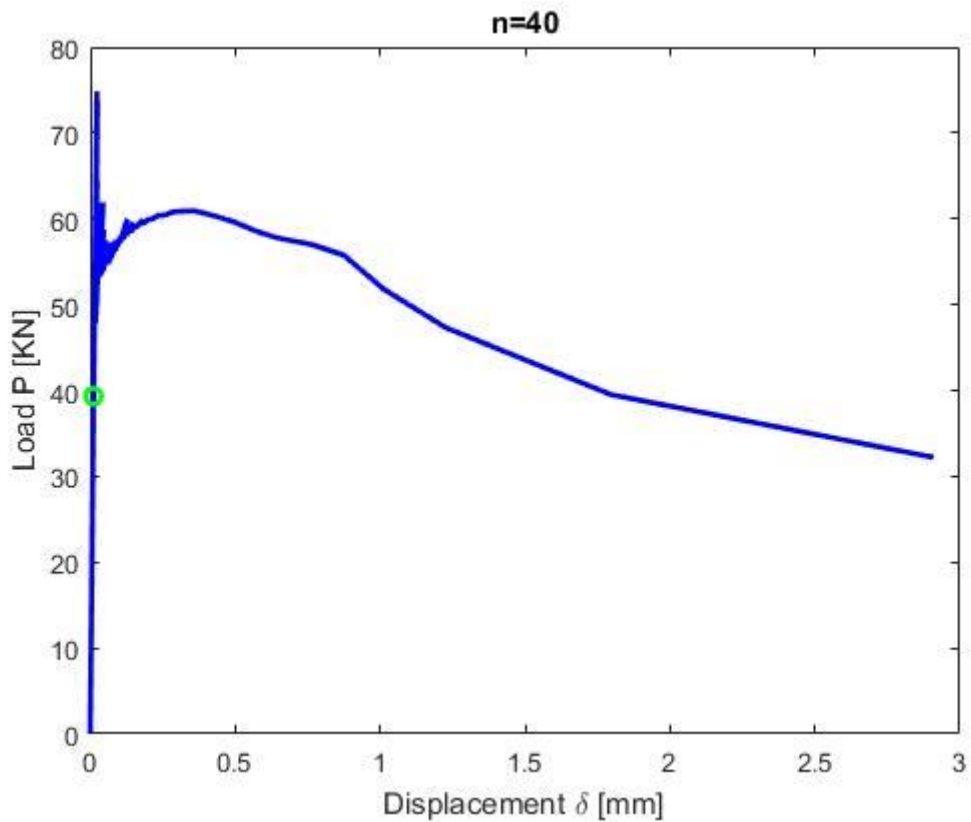


Figure 3.6 Load deflection curve using an intermediate number of fibres, $n = 40$

4 Dimensional Analysis and Numerical Simulations

4.1 Buckingham's π Theorem

Dimensional analysis concepts can be used to define the functional dependence between physical quantities that are relevant for a certain phenomenon under investigation. The Buckingham's π theorem (Buckingham, 1915) states that the functional dependence between a certain number of variables can be reduced to obtain a set of dimensionless groups (P_i groups), which describe synthetically the physical phenomenon. The form of the functional dependence is still unknown, and it has to be defined by means of experimental tests.

The application of the π Theorem requires the definition of the variables involved in the phenomenon. Among these, the output parameter, q_0 , is a function of a number of variables:

$$q_0 = f(q_1, q_2, \dots, q_n; s_1, s_2, \dots, s_m; r_1, r_2, \dots, r_k) \quad (4.1)$$

where q_i are quantities with independent physical dimension; the dimensions of parameters s_i can be, instead, expressed as products of powers of the dimensions of the parameters q_i . The r_i quantities are dimensionless. The product of n dimensionally independent are considered:

$$q_1^{\alpha_{10}} q_2^{\alpha_{20}} \dots q_n^{\alpha_{n0}} = \prod_{i=1}^n q_i^{\alpha_{i0}} \quad (4.2)$$

to make dimensionless the output parameter, with a suitable choice of α_{i0} . By this way, all the s_i quantities can be transformed in dimensionless variables, as follow:

$$\frac{q_0}{q_1^{\alpha_{10}} q_2^{\alpha_{20}} \dots q_n^{\alpha_{n0}}} = \tilde{F} \left(\frac{s_1}{q_1^{\alpha_{11}} q_2^{\alpha_{21}} \dots q_n^{\alpha_{n1}}}, \frac{s_2}{q_1^{\alpha_{12}} q_2^{\alpha_{22}} \dots q_n^{\alpha_{n2}}}, \dots, \frac{s_m}{q_1^{\alpha_{1m}} q_2^{\alpha_{2m}} \dots q_n^{\alpha_{nm}}}; r_1, r_2, \dots, r_k \right) \quad (4.3)$$

These dimensionless groups are called $\Pi_1, \Pi_2, \Pi_3, \dots, \Pi_m$; the functional relationship can thus be reduced to the much more compact form:

$$\Pi_0 = \tilde{F}(\Pi_1, \Pi_2, \Pi_3, \dots, \Pi_m; r_1, r_2, \dots, r_k) = 0 \quad (4.4)$$

In this section, the Buckingham's π theorem is applied to describe the flexural behaviour of a HRC beam, in the framework of the Bridged Crack Model.

The crack propagation phenomenon in the mid-span cross section is assumed to be governed by the following physical variables, listed together with their physical dimensions:

➤ Beam geometry

- h [L], beam depth;
- b [L], beam thickness;

- a_0 [L], initial crack depth.
- Matrix properties
- K_{IC} [F][L]^{-1.5}, matrix fracture toughness;
 - E [F][L]⁻², matrix Young's modulus;
- Bar properties
- ρ [-], reinforcement percentage;
 - σ_y [F][L]⁻², steel yielding strength;
- Fibre characteristic
- σ_s [F][L]⁻², fibre slippage strength;
 - V_f [-], fibre volume ratio
 - w_c [L], average embedded length of the fibres;
 - n [-], the exponent of bridging law decay;
 - α, β [-], fibre distribution coefficients;
- M_F [F][L], crack propagation moment;
- φ [-], localized rotation;

$$F(M_F, \varphi, K_{IC}, \sigma_s, V_f, \sigma_y, E, w_c, \rho, \alpha, \beta, n, h, b, a_0,) = 0 \quad (4.5)$$

The fundamental physical dimensions involved in the problem are force [F] and length [L]. In this respect, if K_{IC} and h are assumed as independent variables, the application of Buckingham's Theorem leads to the following formulation:

$$\Pi\left(\frac{M_F}{K_{IC}bh^{1.5}}, \varphi, \frac{\sigma_s h^{0.5}}{K_{IC}}, V_f, \frac{\sigma_y}{K_{IC}} h^{0.5}, \frac{Eh^{0.5}}{K_{IC}}, \frac{w_c}{h}, \rho, \alpha, \beta, n, \frac{b}{h}, \frac{a_0}{h}\right) = 0 \quad (4.6)$$

in which just dimensionless quantities are involved.

$$\Pi\left(\frac{M_F}{K_{IC}bh^{1.5}}, \varphi, \frac{Eh^{0.5}}{K_{IC}}; \rho, \frac{\sigma_y}{K_{IC}} h^{0.5}, V_f, \frac{\sigma_s}{K_{IC}} h^{0.5}, \frac{Ew_c}{K_{IC}h^{0.5}}, \frac{b}{h}, \frac{a_0}{h}\right) = 0 \quad (4.7)$$

Then, considering a fixed geometrical properties, a further reduction in the involved parameters can be obtained:

$$\Pi\left(\frac{M_F}{K_{IC}bh^{1.5}}, \varphi, \frac{Eh^{0.5}}{K_{IC}}; N_{Pb}, N_{Pf}, N_w\right) = 0 \quad (4.8)$$

in which the dependence of the $M_F-\Phi$ response on the three dimensionless numbers, N_{Pf} , N_{Pb} and N_w , is found.

The first one, the *bars reinforcement brittleness number*, N_{Pb} , shows this expression:

$$N_{Pb} = \rho \frac{\sigma_y}{K_{IC}} h^{0.5} \quad (4.9)$$

The second dimensionless parameter, the *fibre reinforcement brittleness number*, has the following expression:

$$N_{Pf} = V_f \frac{\sigma_s}{K_{IC}} h^{0.5} \quad (4.10)$$

And the sum of this parameter gives us the *total reinforcement brittleness number*:

$$N_{Ptot} = N_{Pb} + N_{Pf} \quad (4.11)$$

The *pull-out brittleness number* has the following expression:

$$N_w = \frac{Ew_c}{K_{IC}h^{0.5}} \quad (4.11)$$

which depends on the equivalent embedded length of the fiber.

These three parameters affect the post-cracking behaviour of the composite. More precisely, N_{Pb} and N_{Pf} mainly affect the so called stage II of the post-cracking phase, which can range from catastrophic to strain hardening. By increasing, N_{Ptot} , called also *reinforcement brittleness number*, it is possible to identify the critical value of N_{Ptot} , N_{PC} , which correspond to the *minimum reinforcement condition*. This condition can be achieved in three cases:

- Only with fibre reinforcement ($N_{Pf} = N_{PC}$; $N_{Pb} = 0$);
- Only with bar reinforcement ($N_{Pf} = 0$; $N_{Pb} = N_{PC}$);
- With a combination of fibre and bar reinforcement ($N_{Pf} \neq 0$; $N_{Pb} \neq 0$; $N_{Pf} + N_{Pb} = N_{PC}$).

4.2 Influence of N_{Pb} on the flexural response

To understand the role of the *bars reinforcement brittleness number*, several TPBT numerical simulations are conducted. In each figure, the effect of N_{Pb} (ranging from 0 to 1) is evaluated for a specific combination of N_{Pf} and N_w . Their value is chosen from:

- $N_{Pf} = [0.3; 0.9; 1.5]$
- $N_w = [406; 1219; 2437]$

Geometrical and mechanical properties assumed for the prismatic specimen are summarized in Table 4.1. The slippage constitutive law of hooked-end fibre and the elastic-perfectly plastic law for bars are considered.

Beam thickness	b	[mm]	150
Beam depth	h	[mm]	150
Notch depth	a_0	[mm]	7.5
Dimensionless notch depth	a_0/h	[/]	0.05
Beam span	S	[mm]	500
Beam length	L	[mm]	550
Young's modulus	E	[MPa]	31500
Fracture toughness	K_{IC}	[kg/cm ^{1.5}]	23
Concrete compressive strength	f_{cm}	[MPa]	38
Fibre diameter	d_f	[mm]	0.75
Fibre length	l_f	[mm]	35
Fibre tensile strength	f_u	[MPa]	1100
Number of fibres modelling	n	[/]	40

Table 4.1 Geometrical and mechanical properties of the HRC specimen

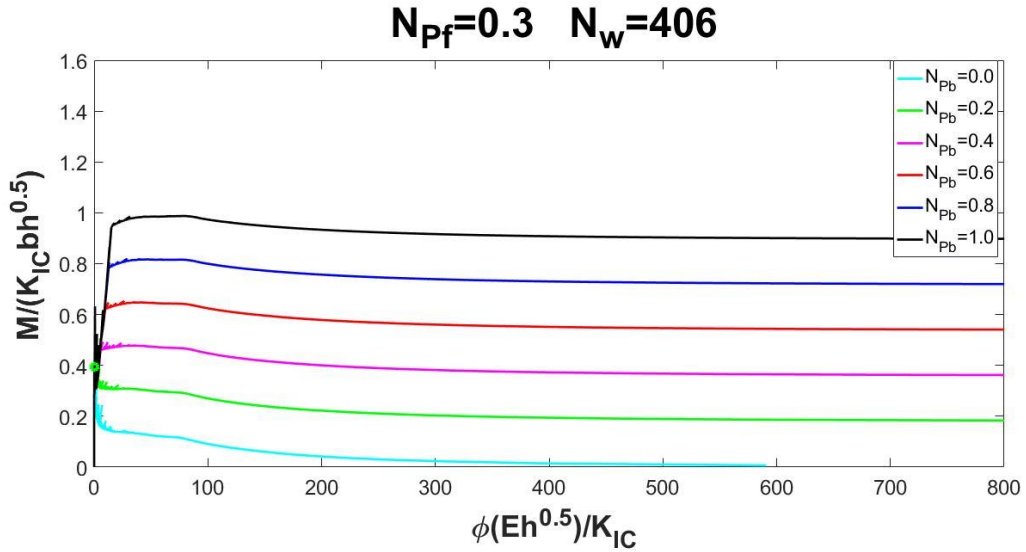


Figure 4.1 Influence of N_{Pb} on flexural response

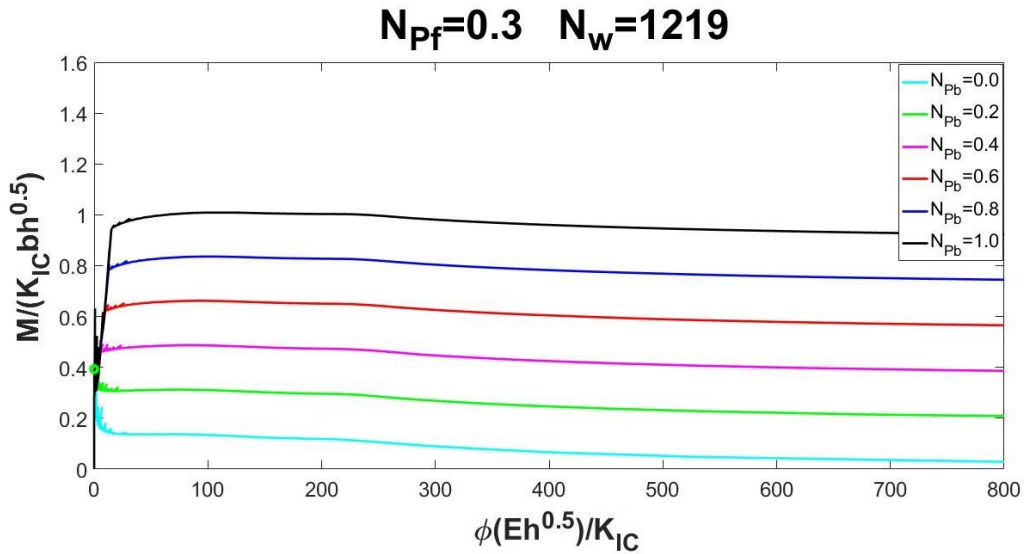


Figure 4.2 Influence of N_{Pb} on flexural response

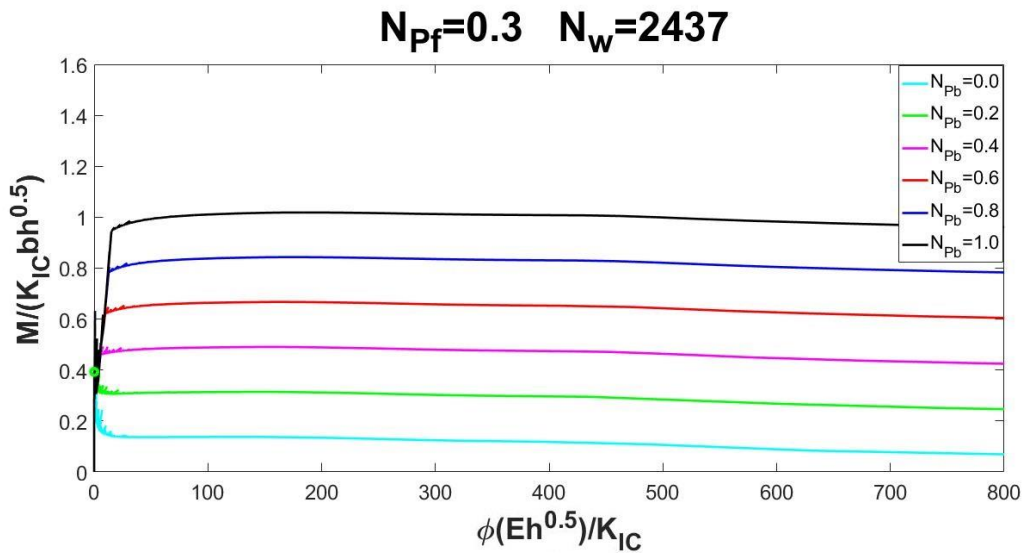


Figure 4.3 Influence of N_{Pb} on flexural response

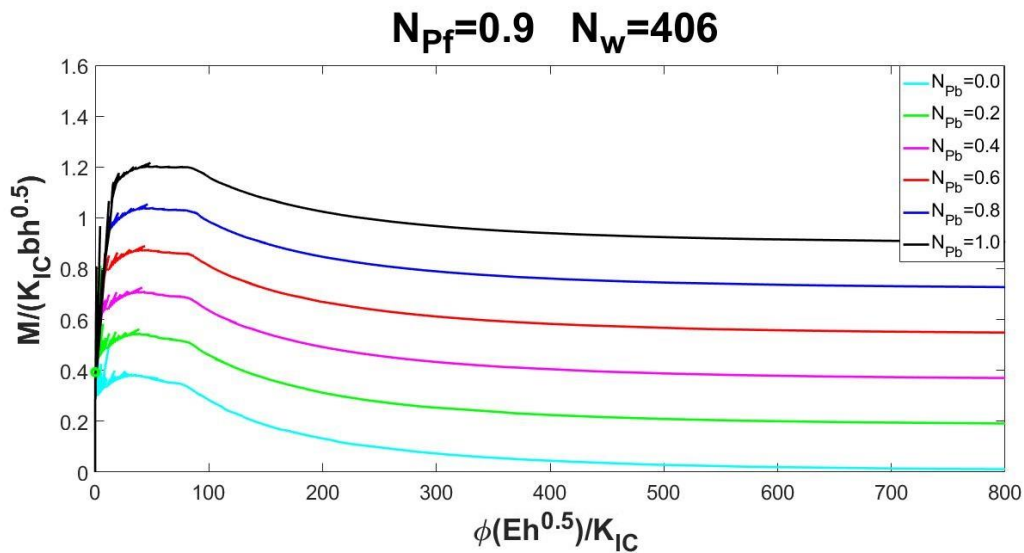


Figure 4.4 Influence of N_{Pb} on flexural response

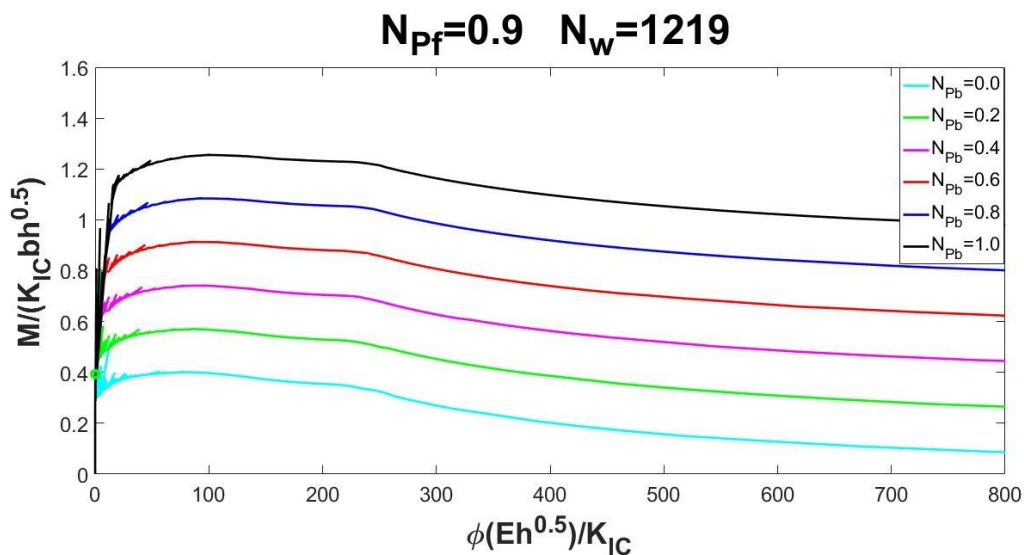


Figure 4.5 Influence of N_{Pb} on flexural response

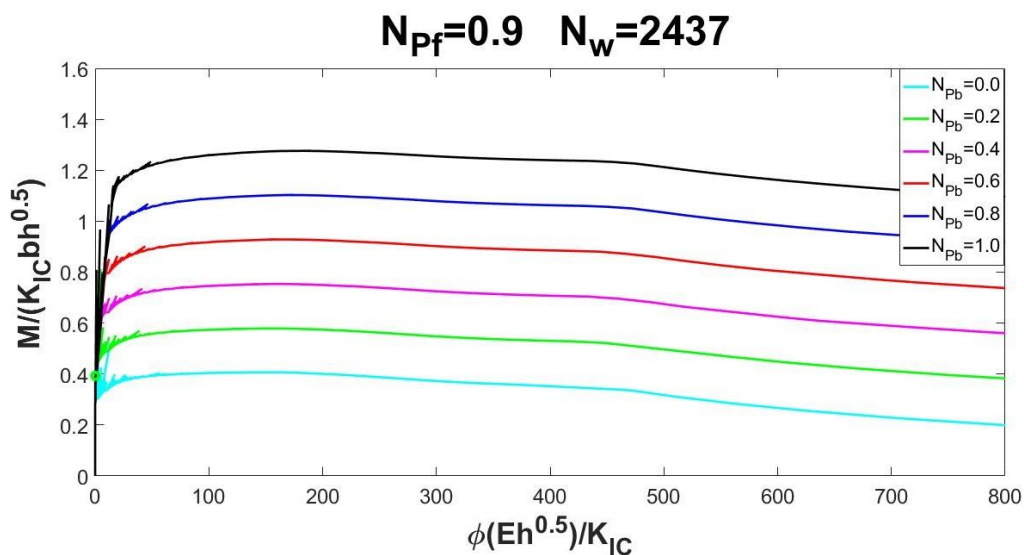


Figure 4.6 Influence of N_{Pb} on flexural response

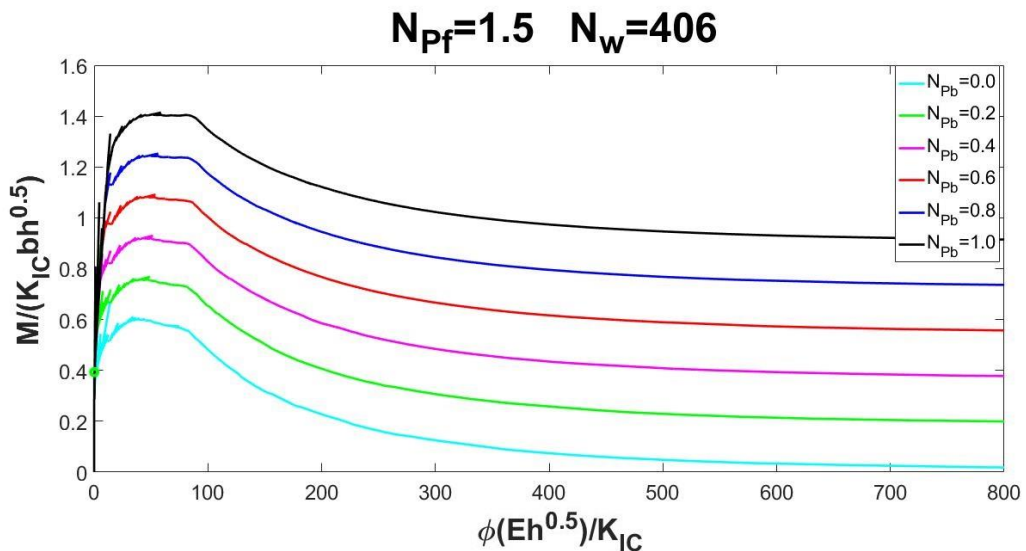


Figure 4.7 Influence of N_{Pb} on flexural response

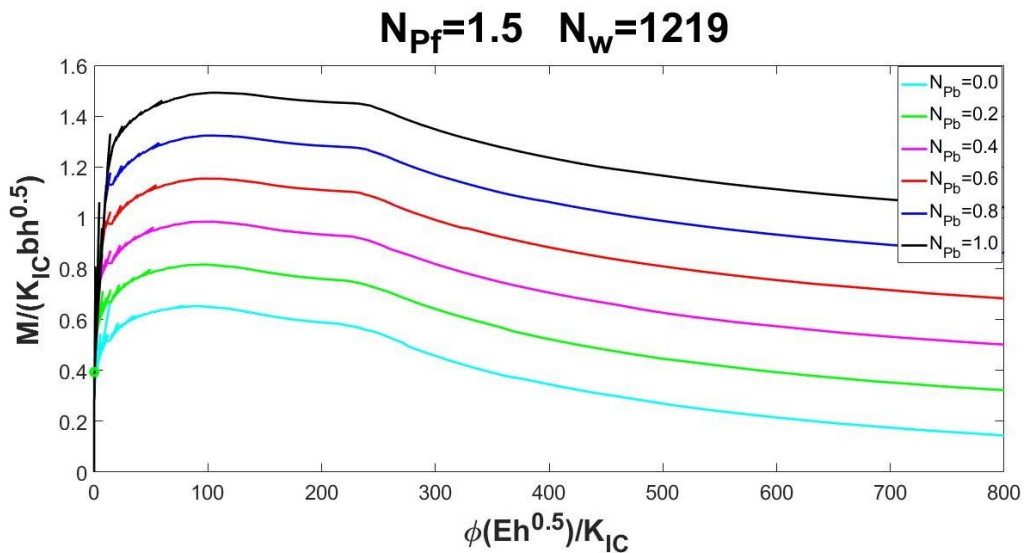


Figure 4.8 Influence of N_{Pb} on flexural response

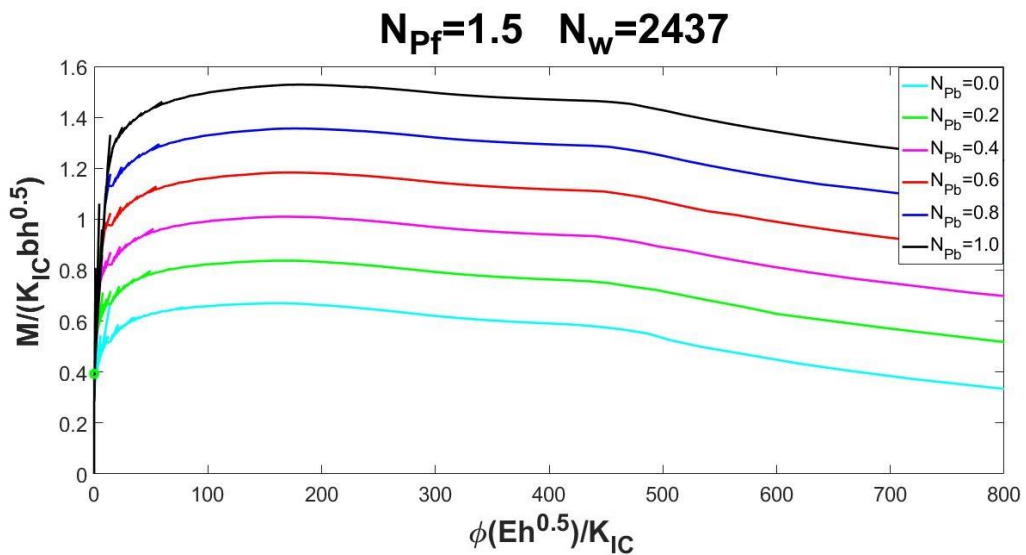


Figure 4.9 Influence of N_{Pb} on flexural response

As the graphs show, the *bars reinforcement brittleness number* mainly influences the level of the plastic plateau. In the fig 4.1, 4.2 and 4.3 it is noted how by increasing the value of N_{Pb} , the minimum reinforcement condition can be reached even with low values of N_{Pf} and N_w

4.3 Influence of N_{Pf} on the flexural response

To understand the role of the *fibre reinforcement brittleness number*, several TPBT numerical simulations are conducted. In each figure, the effect of N_{Pf} (ranging from 0 to 1.5) is evaluated for a specific combination of N_{Pb} and N_w . their value is choses from:

- $N_{Pb} = [0.2; 0.6; 1.0]$;
- $N_w = [406; 1219; 2437]$.

Geometrical and mechanical properties assumed for the prismatic specimen are summarized in Table 4.2. The slippage constitutive law of hooked-end fibre and the elastic-perfectly plastic law for bars are considered.

Beam thickness	b	[mm]	150
Beam depth	h	[mm]	150
Notch depth	a_0	[mm]	7.5
Dimensionless notch depth	a_0/h	[/]	0.05
Beam span	S	[mm]	500
Beam length	L	[mm]	550
Young's modulus	E	[MPa]	31500
Fracture toughness	K_{IC}	[kg/cm ^{1.5}]	23
Concrete compressive strength	f_{cm}	[MPa]	38
Fibre diameter	d_f	[mm]	0.75
Fibre length	l_f	[mm]	35
Fibre tensile strength	f_u	[MPa]	1100
Number of fibres modelling	n	[/]	40

Table 4.2 Geometrical and mechanical properties of the HRC specimen

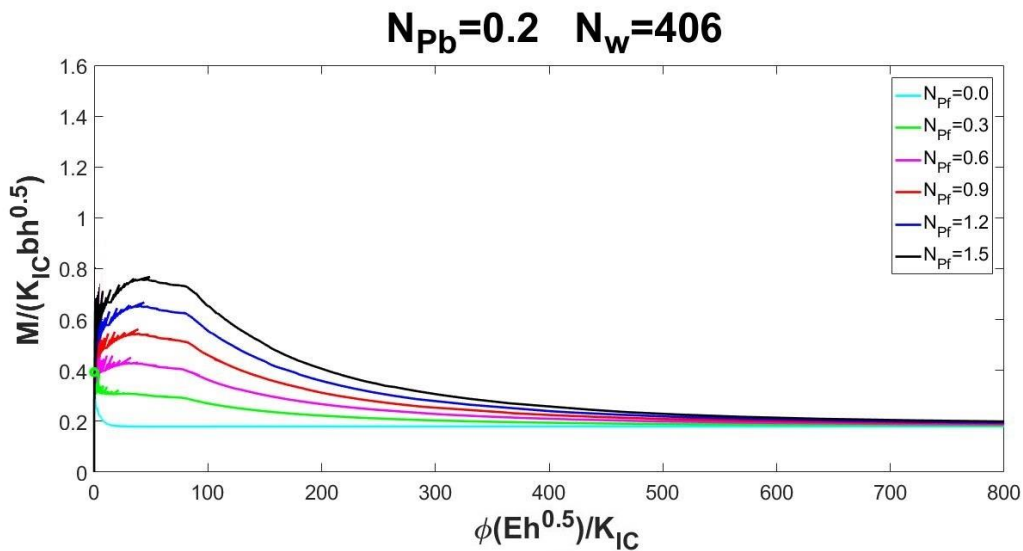


Figure 4.10 Influence of N_{pf} on flexural response

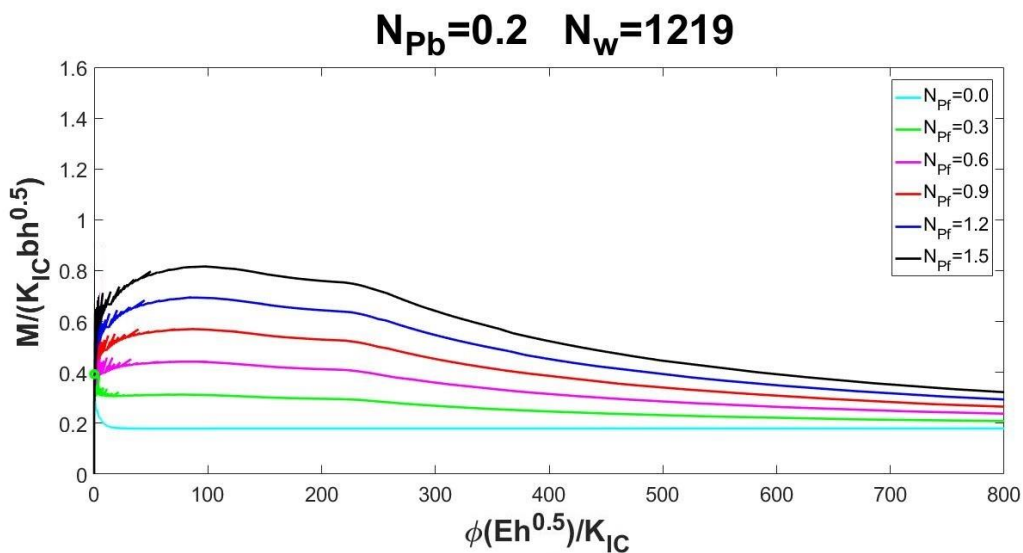


Figure 4.11 Influence of N_{pf} on flexural response

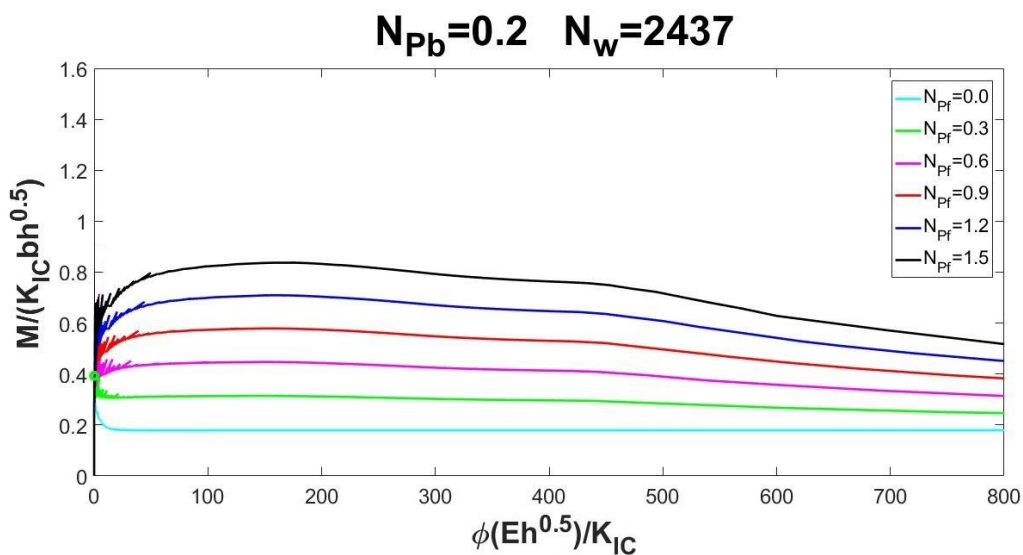


Figure 4.12 Influence of N_{pf} on flexural response

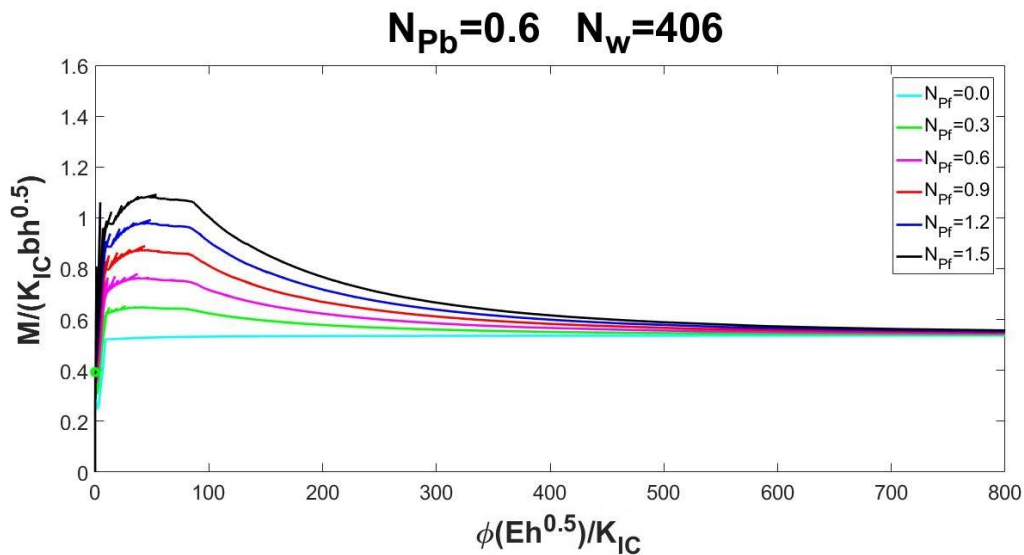


Figure 4.13 Influence of N_{pf} on flexural response

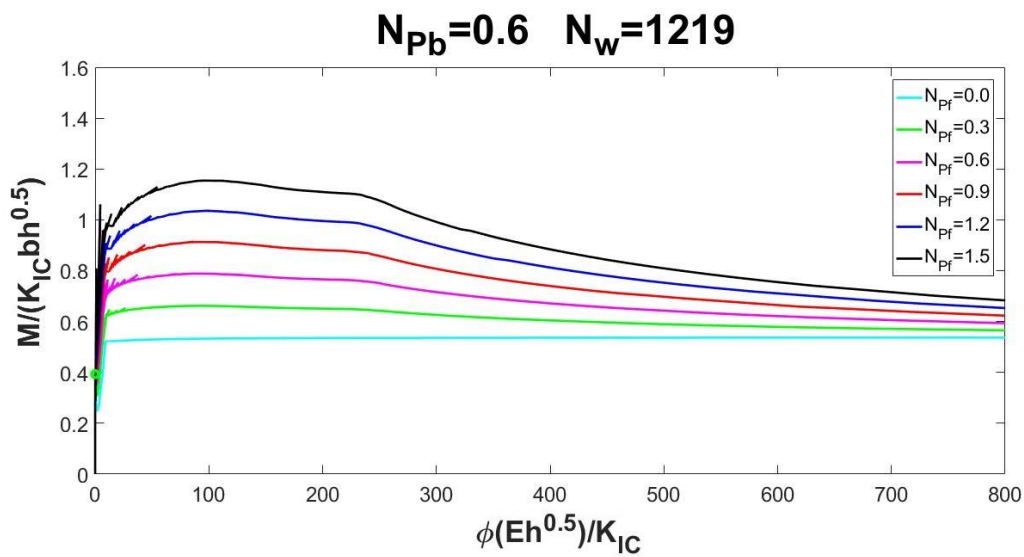


Figure 4.14 Influence of N_{pf} on flexural response

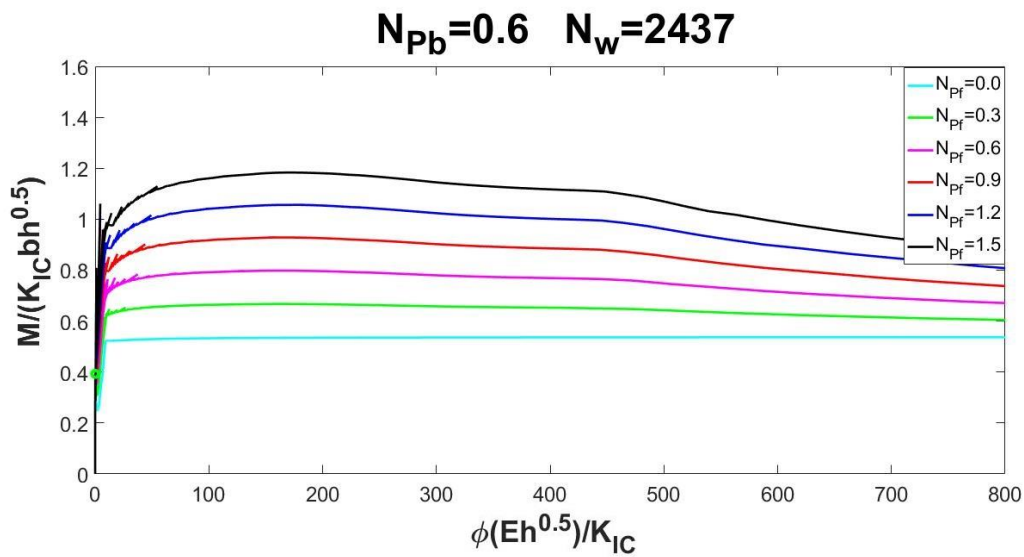


Figure 4.15 Influence of N_{pf} on flexural response

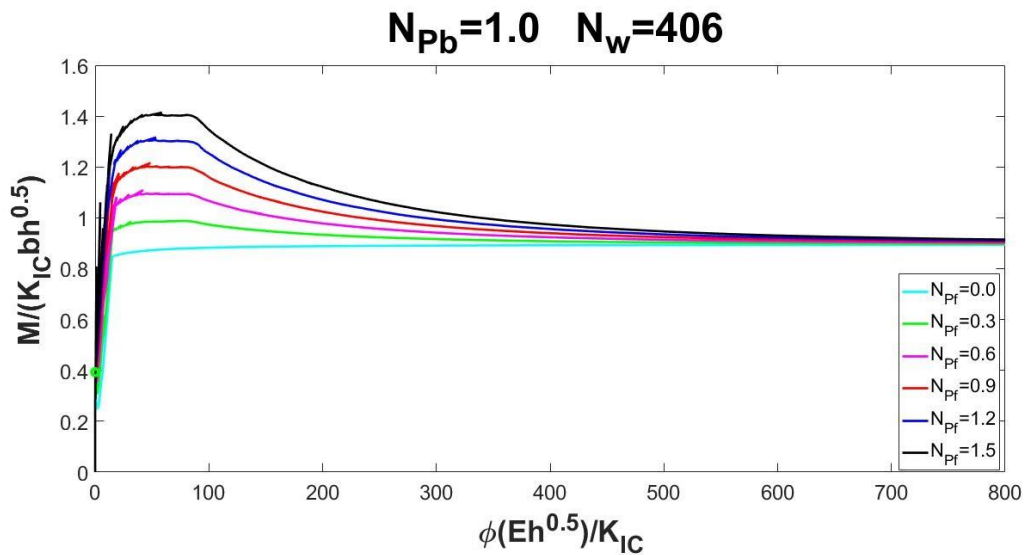


Figure 4.16 Influence of N_{pf} on flexural response

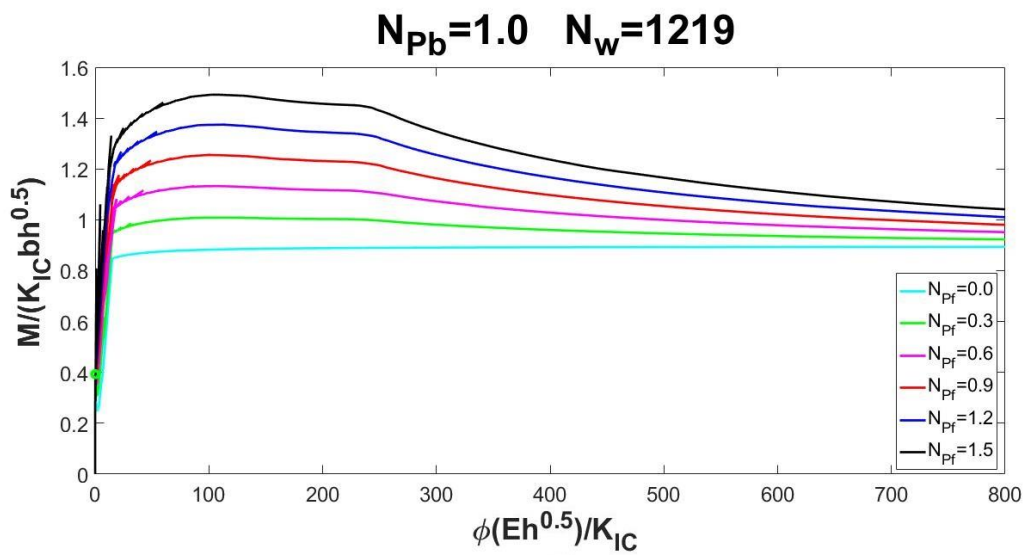


Figure 4.17 Influence of N_{pf} on flexural response

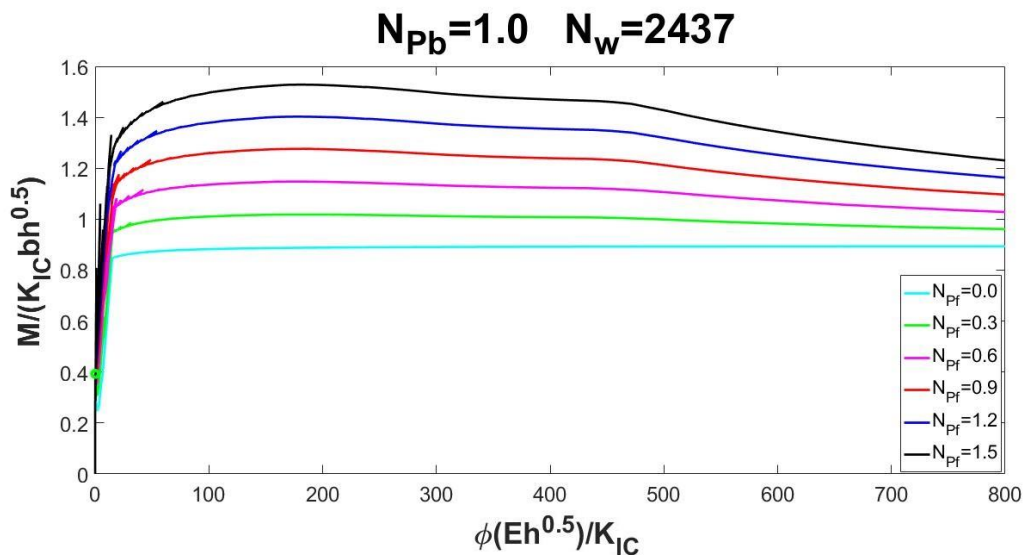


Figure 4.18 Influence of N_{pf} on flexural response

The value of N_{Pf} influences in particular the immediately post-cracking response. Fig. 4.10, 4.11 and 4.12 show how, by increasing N_{Pf} , there is a ductile-to-brittle transition regarding the Stage II of the response, even if the content of bars reinforcement is not sufficient to guarantee an hardening response. In all cases, the contribution of the fibres tends to vanish with the complete disconnection of the cracked cross-section, regardless of the value of N_{Pf} .

4.4 Influence of N_w on the flexural response

To understand the role of the *pull-out brittleness number*, several TPBT numerical simulations are conducted. In each figure, the effect of N_w (ranging from 203 to 2437) is evaluated for a specific combination of N_{Pb} and N_{Pf} . Their value is chosen from:

- $N_{Pb} = [0.2; 0.6; 1.0]$;
- $N_{Pf} = [0.3; 0.9; 1.5]$.

Geometrical and mechanical properties assumed for the prismatic specimen are summarized in Table 4.3. The slippage constitutive law of hooked-end fibre and the elastic-perfectly plastic law for bars are considered.

Beam thickness	b	[mm]	150
Beam depth	h	[mm]	150
Notch depth	a_0	[mm]	7.5
Dimensionless notch depth	a_0/h	[/]	0.05
Beam span	S	[mm]	500
Beam length	L	[mm]	550
Young's modulus	E	[MPa]	31500
Fracture toughness	K_{IC}	[kg/cm ^{1.5}]	23
Concrete compressive strength	f_{cm}	[MPa]	38
Fibre diameter	d_f	[mm]	0.75
Fibre length	l_f	[mm]	35
Fibre tensile strength	f_u	[MPa]	1100
Number of fibres modelling	n	[/]	40

Table 4.3 Geometrical and mechanical properties of the HRC specimen

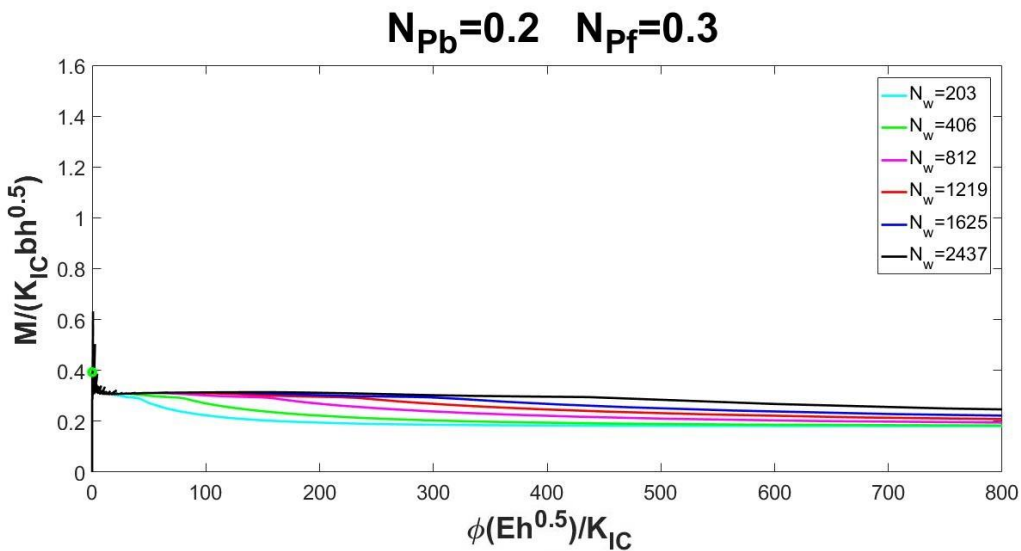


Figure 4.19 Influence of N_w on flexural response

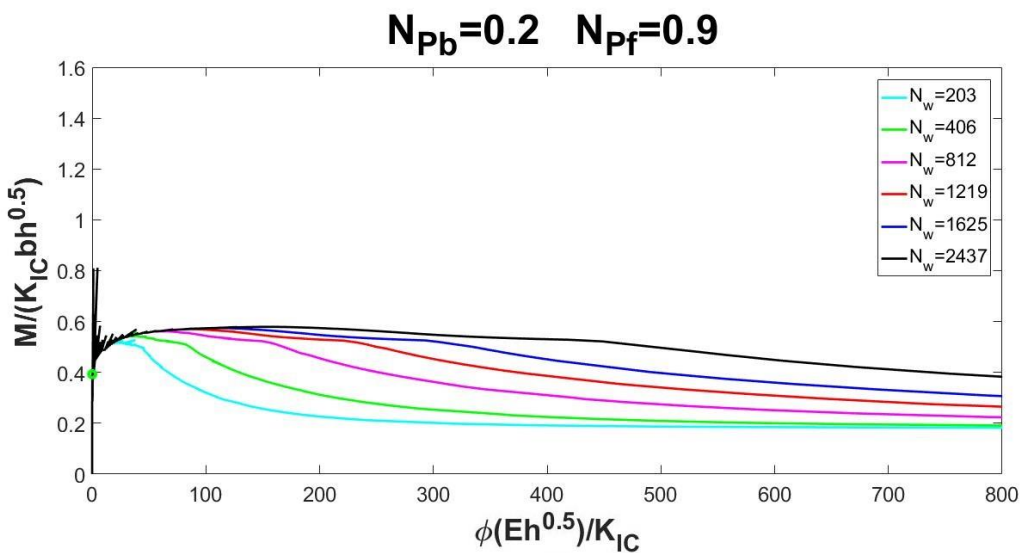


Figure 4.20 Influence of N_w on flexural response

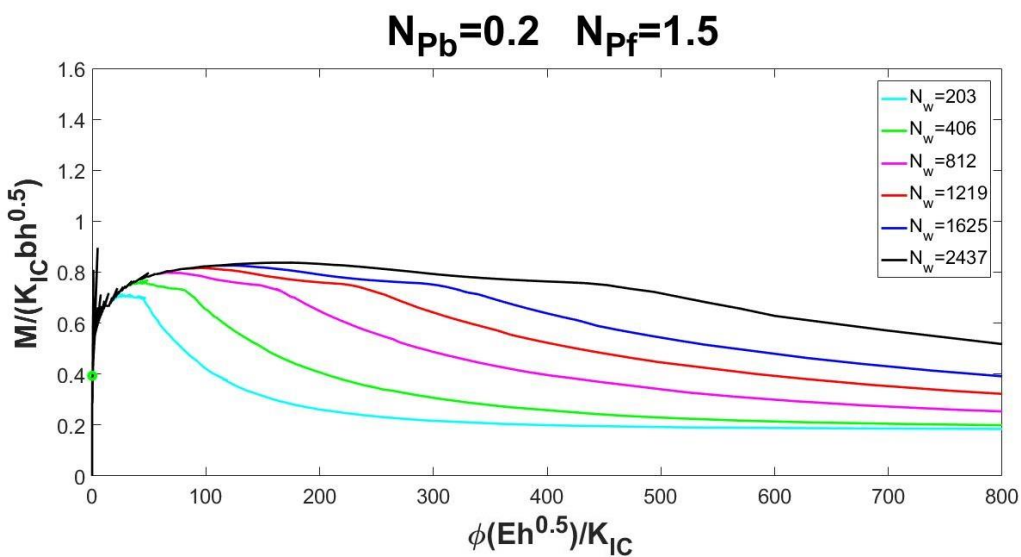


Figure 4.21 Influence of N_w on flexural response

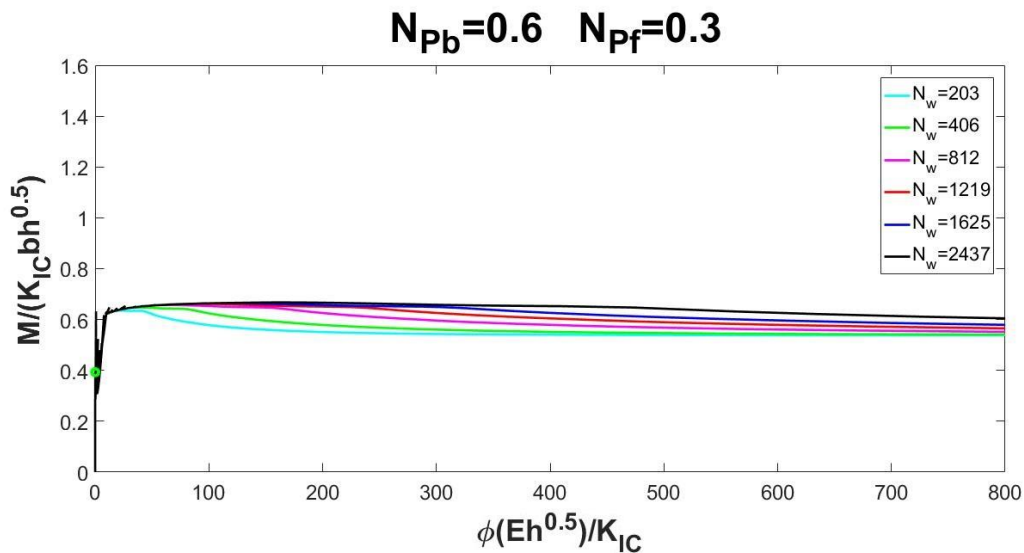


Figure 4.22 Influence of N_w on flexural response

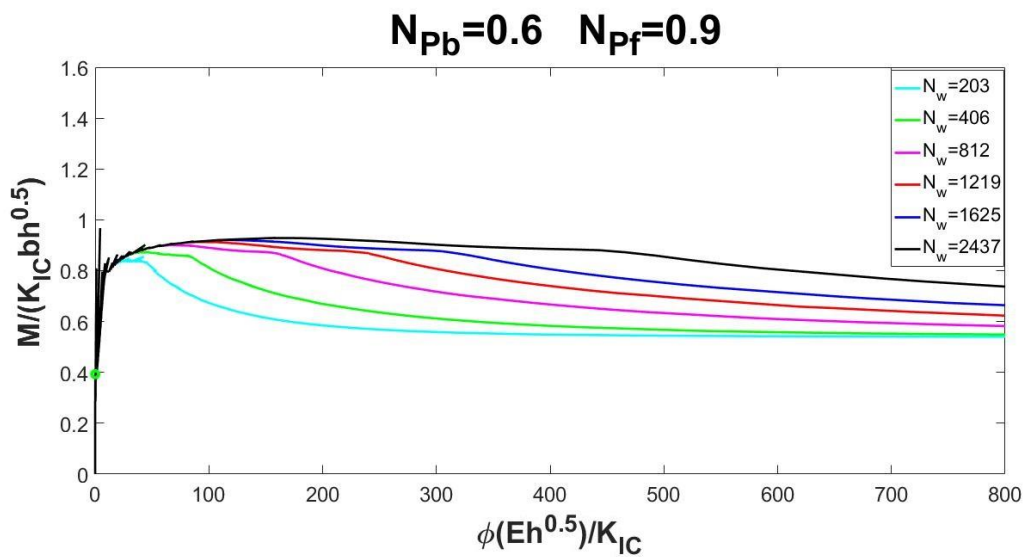


Figure 4.23 Influence of N_w on flexural response

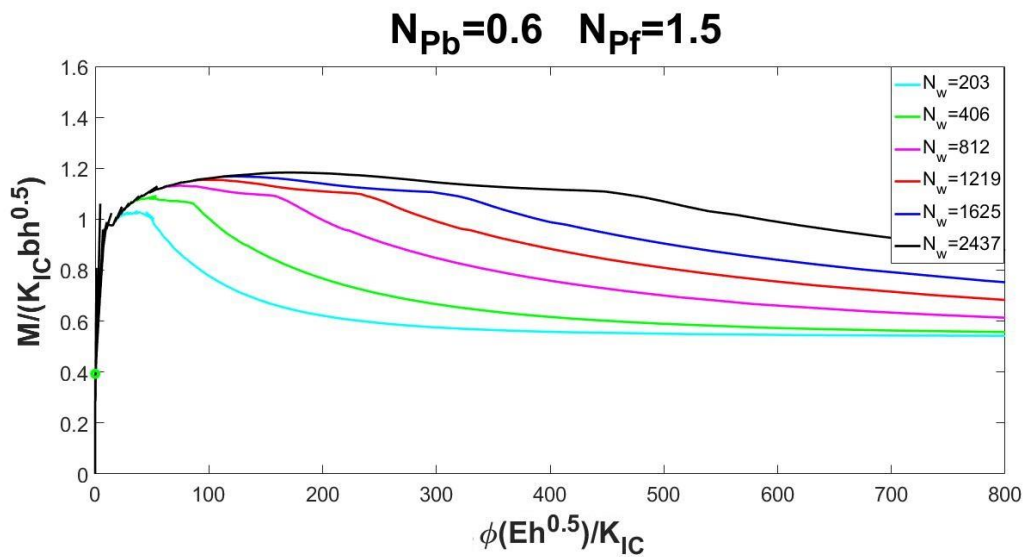


Figure 4.24 Influence of N_w on flexural response

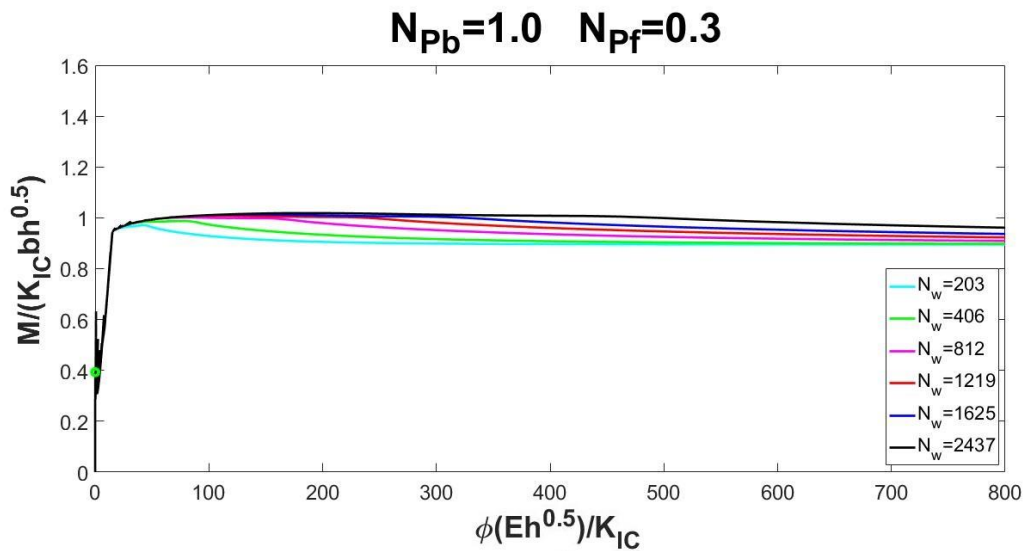


Figure 4.25 Influence of N_w on flexural response

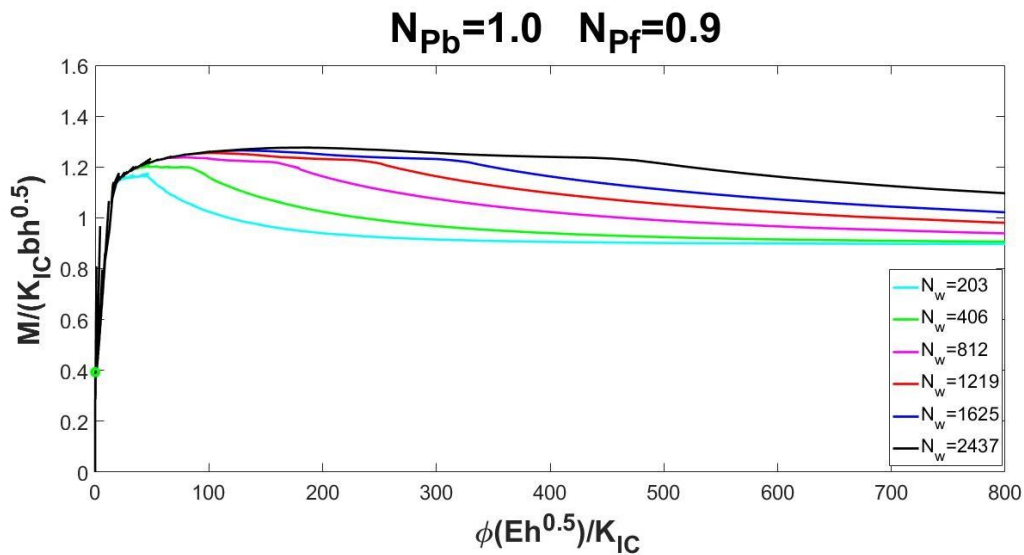


Figure 4.26 Influence of N_w on flexural response

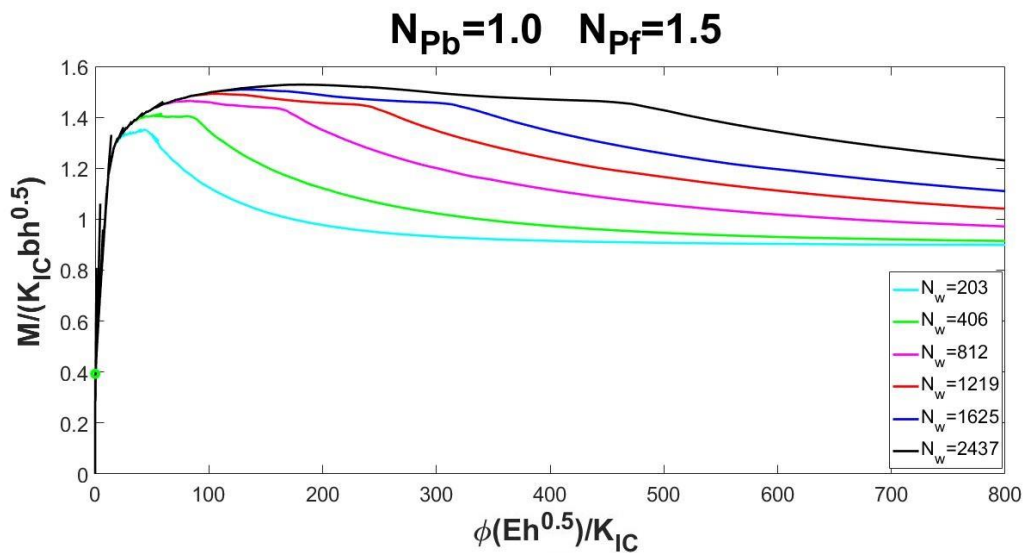


Figure 4.27 Influence of N_w on flexural response

The value of N_w influences the fibre's contribution; with a low value of N_w the effect of the fibres vanished quickly and the response of the element tends to the plastic plateau due to the bars reinforcement. Moreover, N_w becomes particularly relevant when the content of bars is low, as can be seen from the fig.4.19, 4.20 and 4.21.

4.5 Minimum reinforcement condition

By means of the Bridged Crack Model, the minimum reinforcement condition has been extensively discussed by assuming a rigid-perfectly plastic constitutive law to describe the yielding mechanism of the reinforcing layers (Carpinteri, 1984). The critical value of the brittleness number, N_{PC} , which governs the ductile-to-brittle transition, makes it possible to evaluate the minimum steel percentage that guarantees a stable post-peak response, as a function of the relative initial crack depth, a_0/h , and of the relative position of the reinforcement layer, c_0/h (c_0 being the thickness of the concrete cover).

Subsequently, a similar analysis was performed in the case of FRC elements, and it was shown that increasing the fibre volume ratio led to a brittle-ductile transition of the element's behaviour (Carpinteri, 1996). This transition is governed by two dimensionless numbers: the *fibre reinforcement brittleness number*, N_{Pf} , and the *pull-out brittleness number*, N_{Pb} .

On the other hand, the present numerical analysis shows that, to fully describe the post-cracking regime of the HRC cross-section, all these dimensionless parameter must be taken into account.

From Eq. 4.10, the critical value of the *reinforcement brittleness number* N_{PC} , can be reached with different combination of N_{Pb} and N_{Pf} . So, for a different values of a_0/h and c_0/h , the *condition of minimum reinforcement* is investigated. The results are shown in fig. 4.28 and 4.30. Instead, fig. 4.29 and 4.31 show how, by increasing the bar content (and therefore N_{Pb}), the minimum reinforcement condition can also be achieved using a lower fibre content than is necessary for an FRC element and vice versa for an RC element.

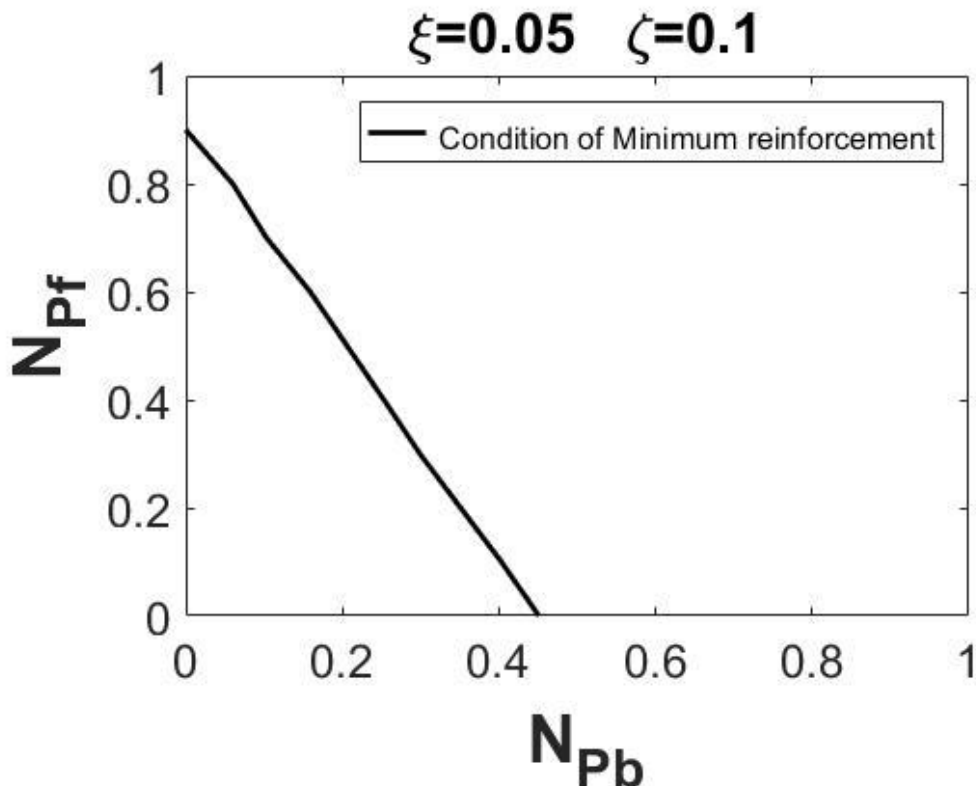


Figure 4.28 Minimum reinforcement condition, N_{Pf} – N_{Pb} diagram

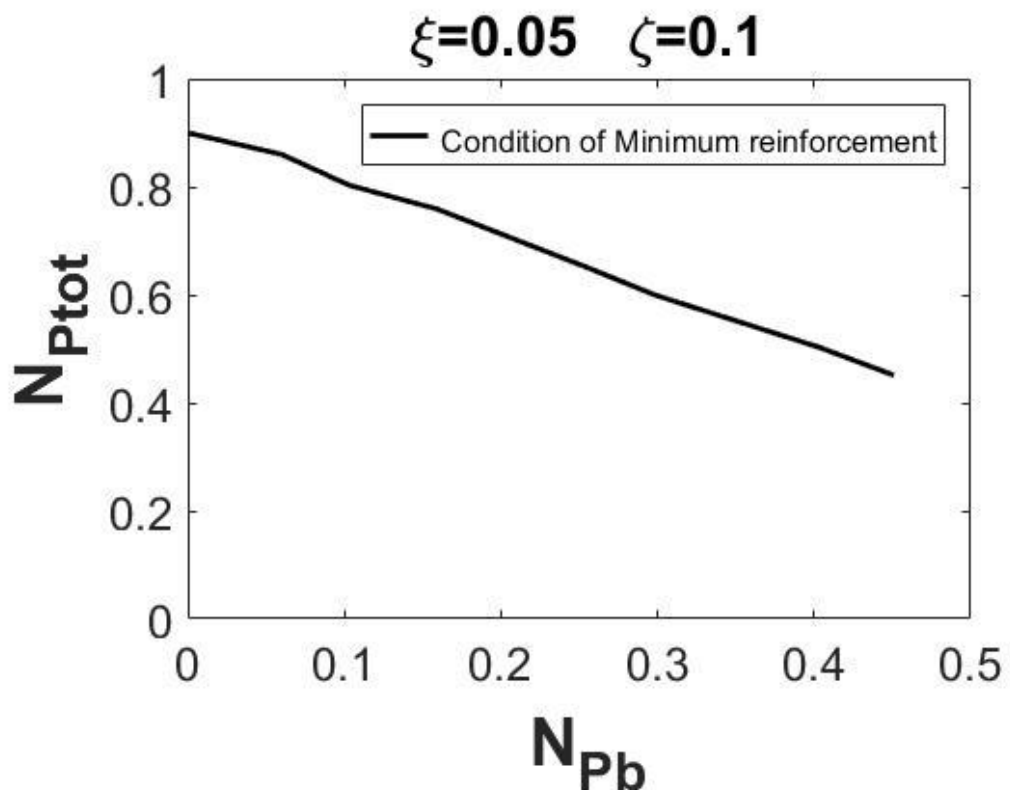


Figure 4.29 Minimum reinforcement condition, $N_{P\text{tot}} - N_{Pb}$ diagram

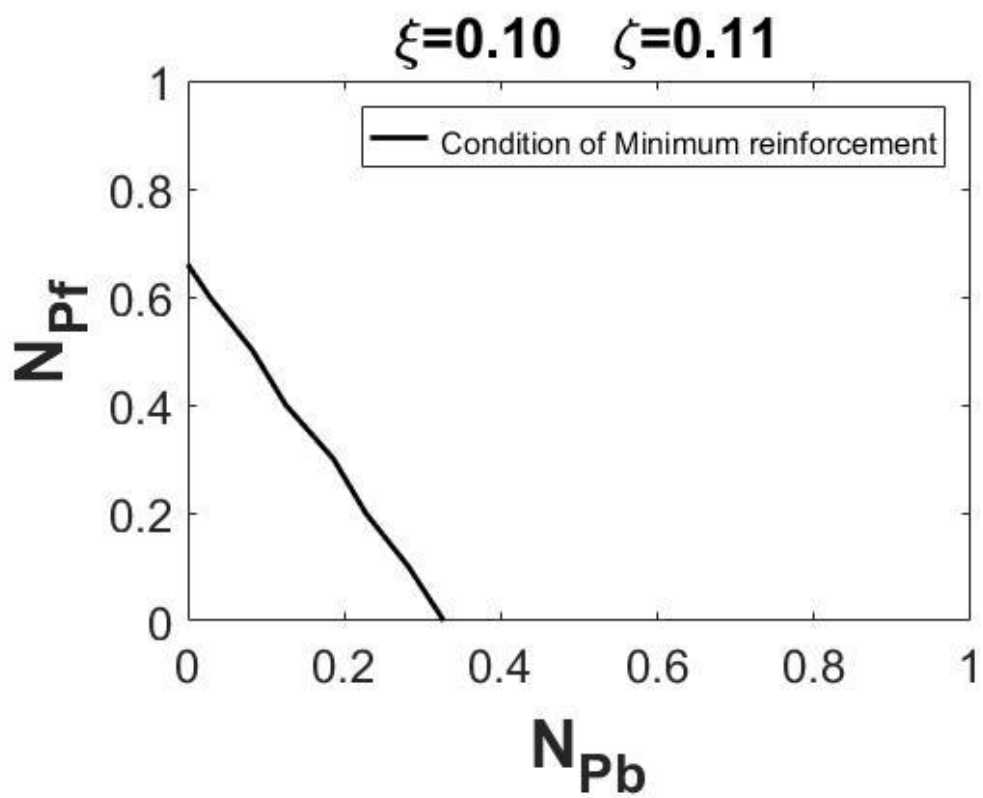


Figure 4.30 Minimum reinforcement condition, $N_{Pf} - N_{Pb}$ diagram

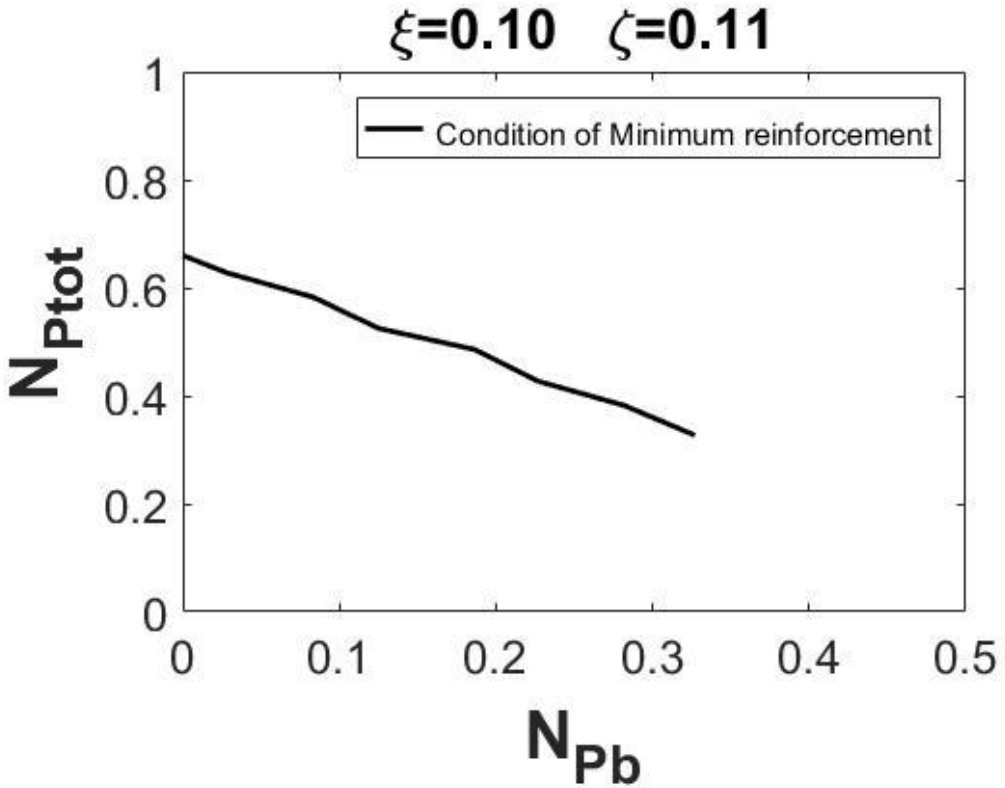


Figure 4.31 Minimum reinforcement condition, $N_{\text{Ptot}} - N_{\text{Pb}}$ diagram

As is shown in figure 4.28 and 4.30 the *minimum reinforcement condition* was investigated for a different combination of N_{Pb} and N_{Pf} . The two values can be connected with good approximation using a linear correlation, described by the following expression:

For $\xi = 0.05; \zeta = 0.10$:

$$N_{\text{Pb}} = -0.49N_{\text{Pf}} + 0.45 \quad (4.12)$$

For $\xi = 0.10; \zeta = 0.11$:

$$N_{\text{Pb}} = -0.49N_{\text{Pf}} + 0.32 \quad (4.12)$$

The two expressions have a similar angular coefficient, while the known term is equal to the value of N_{PC} that occurs in the presence of only reinforcement bars (that depends by a_0/h and c_0/h), that is, when:

$$N_{\text{Pf}} = 0; N_{\text{Pb}} = N_{\text{PC}}$$

5 Experimental results

5.1 Introduction

The design of HRC members requires wide experimental campaigns. Experimental tests are fundamental to define the mechanical properties of the constituent materials, and to provide the so-called mix design of the composite. Once these parameters have been defined it's possible use the bridged crack model to search for the minimum reinforcement condition.

This argument has been extensively discussed in the past, in the case of ordinary reinforced concrete beams and fibre reinforced concrete beam. In the first case (RC beams) the minimum reinforcement condition is uniquely described by the reinforcement brittleness number, N_{Pb} (Bosco and Carpinteri, 1990). The latter, in case of yielding bridging mechanism of the steel rebars, is a function of steel yielding stress, concrete fracture toughness, steel area percentage, and beam depth, making possible the evaluation of the size effects on the phenomenon.

Subsequently, the definition of the minimum reinforcement condition was extended to FRC structural elements. As discussed in the previous section, another geometrical property has to be considered in the dimensional analysis: the embedded length of the fibre, w_c . Thus, there are finally two dimensionless parameters to describe completely the flexural response: N_w and N_{Pf} . Reinforcement geometry, its resistance and finally its volume ratio can be thus defined on the basis of these dimensionless parameters, keeping also the effect of the size variation among test specimen and structural element.

In this work, the discussion about the minimum reinforcement condition is extended to HRC structural elements. The simultaneous presence of bars and fibres means that the response of the HRC element has aspects common to those of the FRC and RC ones. Therefore, in this case, the flexural response is briefly described by all three parameters previously seen: N_{Pb} , N_{Pf} and N_w

In this Chapter three experimental campaigns, conducted by other Authors, are analysed. The main features characterizing each work are the matrix concrete composition, the fibre type and the amount of reinforcing fibres, the bars type and the range of steel percentage considered, the presence or absence of the initial notch, and finally the test setup. For each work, these main features are described. Then, the results of recognizing of material properties are summarized.

By applying this procedure to the experimental $P - \delta$ curves of the FRC elements it was possible to identify the parameters relating to the concrete matrix and to the reinforcing fibres (σ_s , w_c). The fracture toughness, K_{IC} , is directly connected to the first cracking moment. On the other hand, by analyzing the post-cracking regime of the composite, fibre slippage strength, σ_s , and its embedded length, w_c , are estimated. Particularly, the embedded length governs mainly the softening branch, in which the slippage phenomenon is prevalent. It is worth notice that the matrix properties are uniquely defined, whereas the bridging force and the fibre embedded length depends on the fibre distribution. Subsequently, considering the average of the three parameters, the same procedure was repeated on the experimental $P - \delta$ curves of the HRC elements in order

to estimate the mechanical parameters of the bars, namely the crack opening corresponding to the yielding of the bar, w_y , and the yield strength, σ_y .

Thus, on the bases of these five estimated parameters, the dimensionless quantities N_{Pb} , N_{Pf} and N_w are computed and the numerical $P - \delta$ curves were reproduced again, which showed a good correspondence with the experimental ones. The same procedure is repeated for each experimental curve.

7

5.2 Comparison with experimental data

5.2.1 Holschemacher et al. experimental work

In the experimental campaign carried out by Holschemacher et al. (2010), the influence of geometry and tensile strength of fibres, as well as the effects of different reinforcement ratios was investigated. The fibre contents were 0, 20, 40 and 60 Kg\m³ for two different type of fibres (F1 type and F2 type). Instead, the steel bars reinforcement percentages were 0.00, 0.25 and 1.00% for a total of 24 tested specimens. To determine the fracture parameters of the HRC composite, unnotched beams were tested under four point loading according to the German regulations for SFRC on small beams ($15 \times 15 \times 70 \text{ cm}$). In the following, the main variables of the experimental campaign, including the results, are summarized.

- **MATERIALS**

- **Matrix**

The matrix mixture presents a compressive strength of 86 Mpa.

- **Fibre**

Two type of Steel hooked-end Fibres (SF) were used. Their mechanical and geometrical properties are reported in Table 5.1.

			F1	F2
Fibre diameter	d_f	[mm]	1	1
Fibre length	l_f	[mm]	50	50
Fibre aspect ratio	λ	[-]	50	50
Fibre tensile strength	f_u	[MPa]	1100	1900

Table 5.1 Fibre mechanical and geometrical properties.

- TEST SETUP

Casting of the specimens, their curing and the experimental setup were chosen according to the German regulations. Accordingly, the beams were loaded orthogonal to the casting direction. The load was controlled using a displacement method with a rate of 0.2 mm/min. The deflection was recorded by two LVDTs (one of each side of the beam). Eighteen small beams ($15 \times 15 \times 70 \text{ cm}$) were casted for each fibre content. Among them 12 were with two different steel bar reinforcement ratios (six with 0.25% and six with 1.0%) and six beams without steel reinforcement. The distance between the bottom edge of the reinforcing steel and the concrete surface was 2 cm. Longitudinal tensile reinforcement had hooks at the beam ends to ensure adequate anchorage. The hardened properties of the mixture were tested 28 days after casting. The specimens are unnotched, so during the modelling will be considered a fictitious initial notch of:

$$\frac{a_0}{h} = 0.05 = 7.5 \text{ mm}$$

And the bar's concrete cover is equal to 20 mm, so:

$$\frac{c_0}{h} = 0.13 = 20 \text{ mm}$$

A scheme of the test setup is shown in Fig. 5.1.

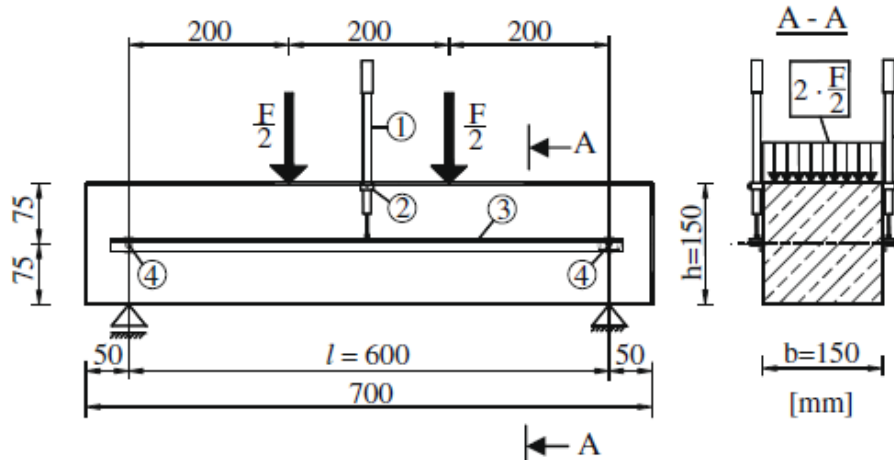


Figure 5.1 FPBT setup on specimen, Holschemacher (2010)

- IDENTIFICATION

- Part 1 (FRC)

For each experimental $P - \delta$ curves of the FRC elements, a best fitting procedure was applied in order to defining the average values of K_{IC} , σ_s , and w_c .

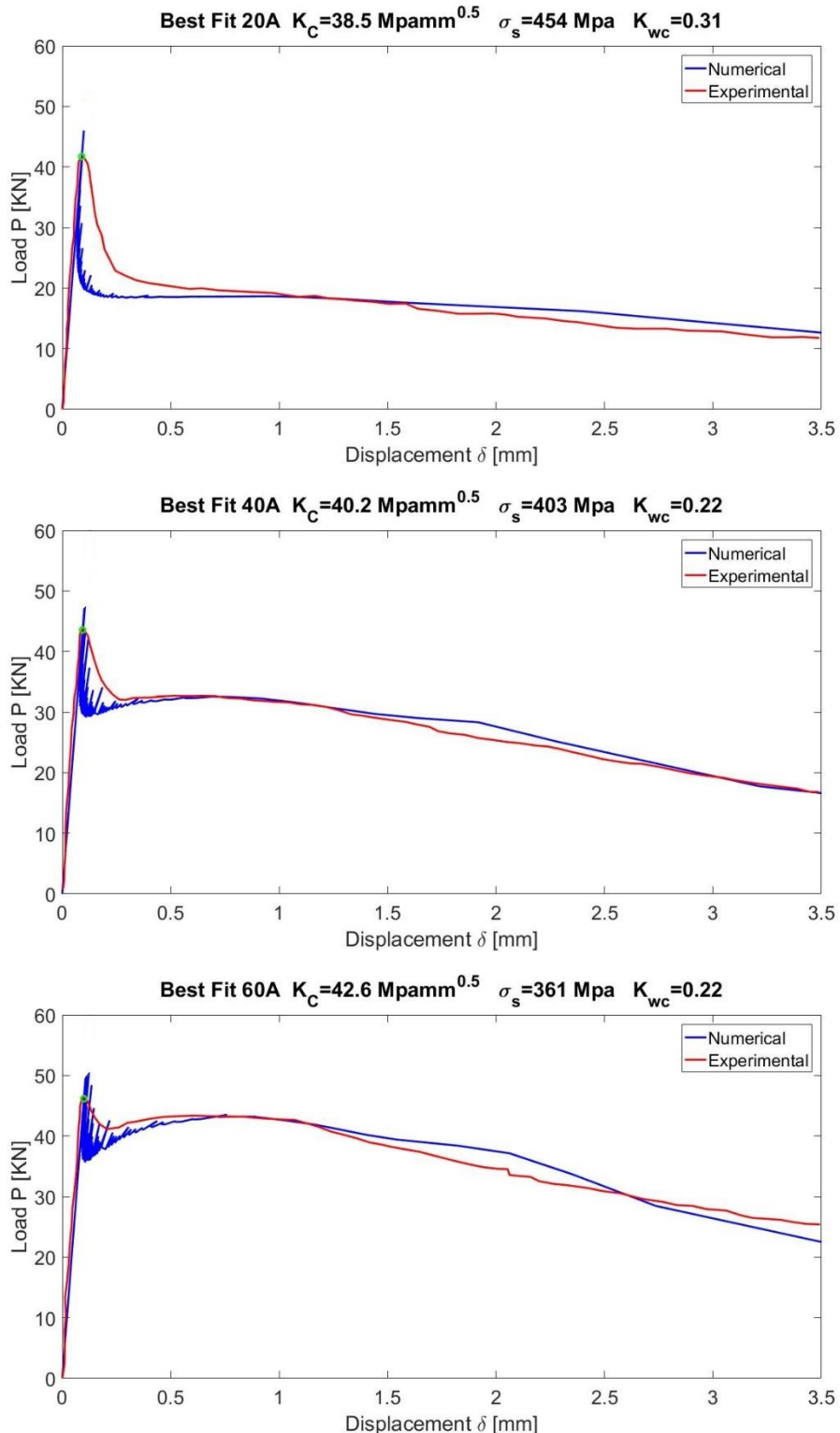


Figure 5.2 Best fitting for curves A, respectively with 20,40 and 60 kg/m³ of fibre content

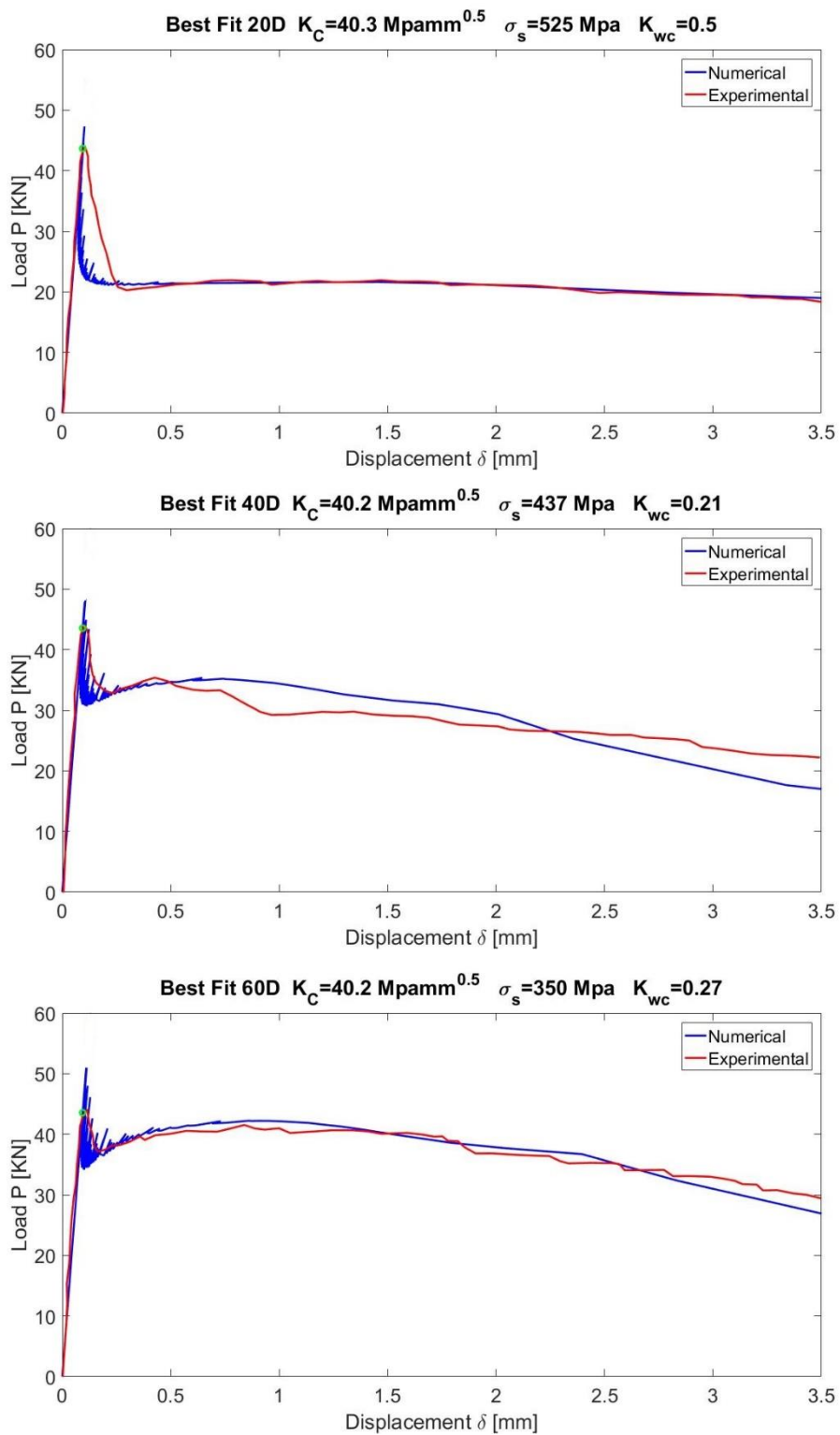


Figure 5.3 Best fitting for curves D, respectively with 20, 40 and 60 kg/m³ of fibre content

The identifying parameters are collected in Table 5.2 and 5.3.

ID	K _{IC}	σ_s	K _{wc}
20 A	38.5	454	0.31
40 A	40.2	403	0.22
60 A	42.6	361	0.22
AVG	40.4	406	0.25

Table 5.2 Average value of mechanical parameters

On the hand, for fibre-type F2:

ID	K _{IC}	σ_s	K _{wc}
20 D	40.3	525	0.50
40 D	40.2	437	0.21
60 D	40.2	350	0.27
AVG	40.2	437	0.33

Table 5.3 Average value of mechanical parameters

➤ Part 2 (HRC)

For each experimental $P - \delta$ curves of the HRC elements, a best fitting procedure was applied in order to defining the average values of σ_y , and w_y

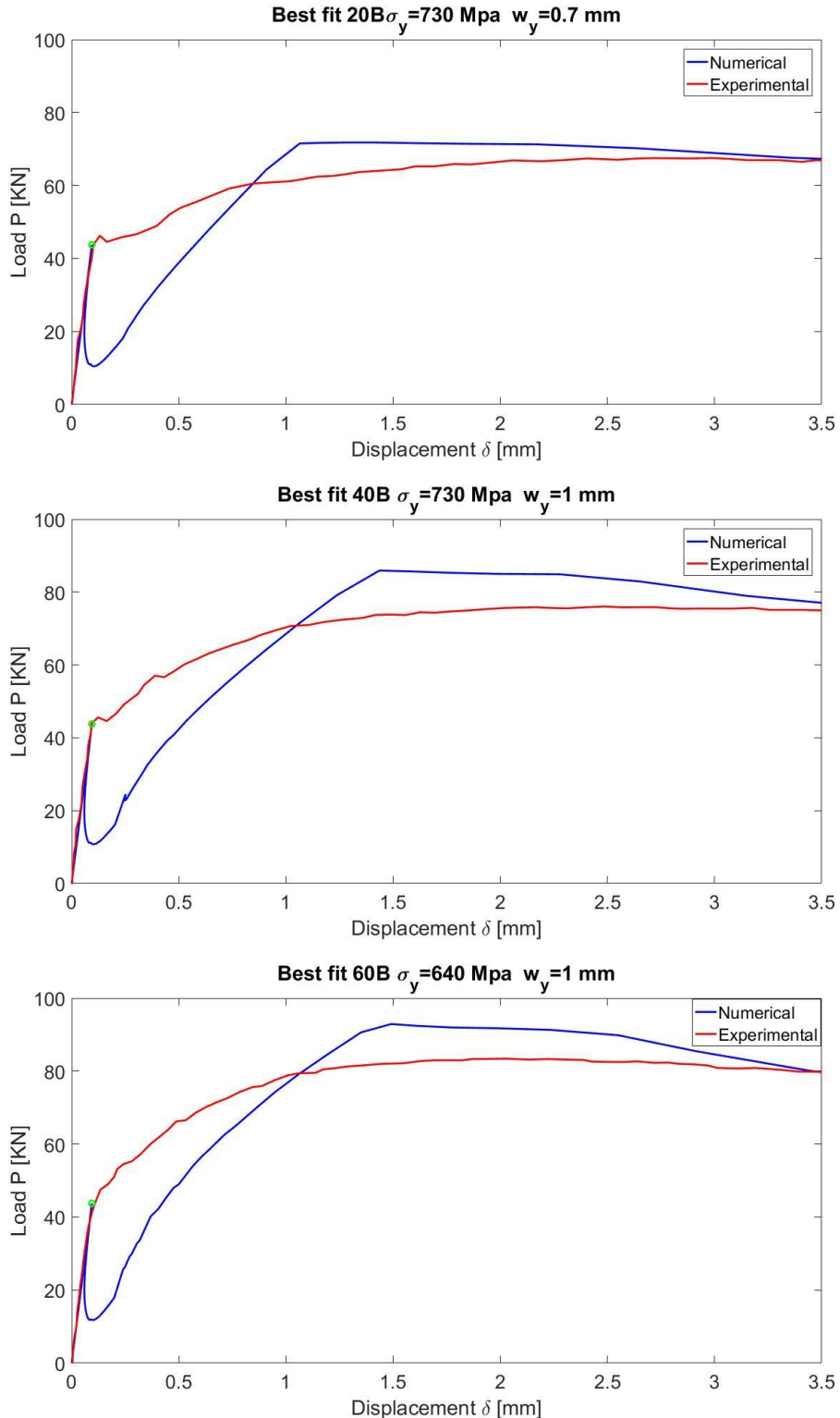


Figure 5.4 Best fitting for curves B (bar reinforcement 2Φ6), respectively with 20, 40 and 60 kg/m³ of fibre content

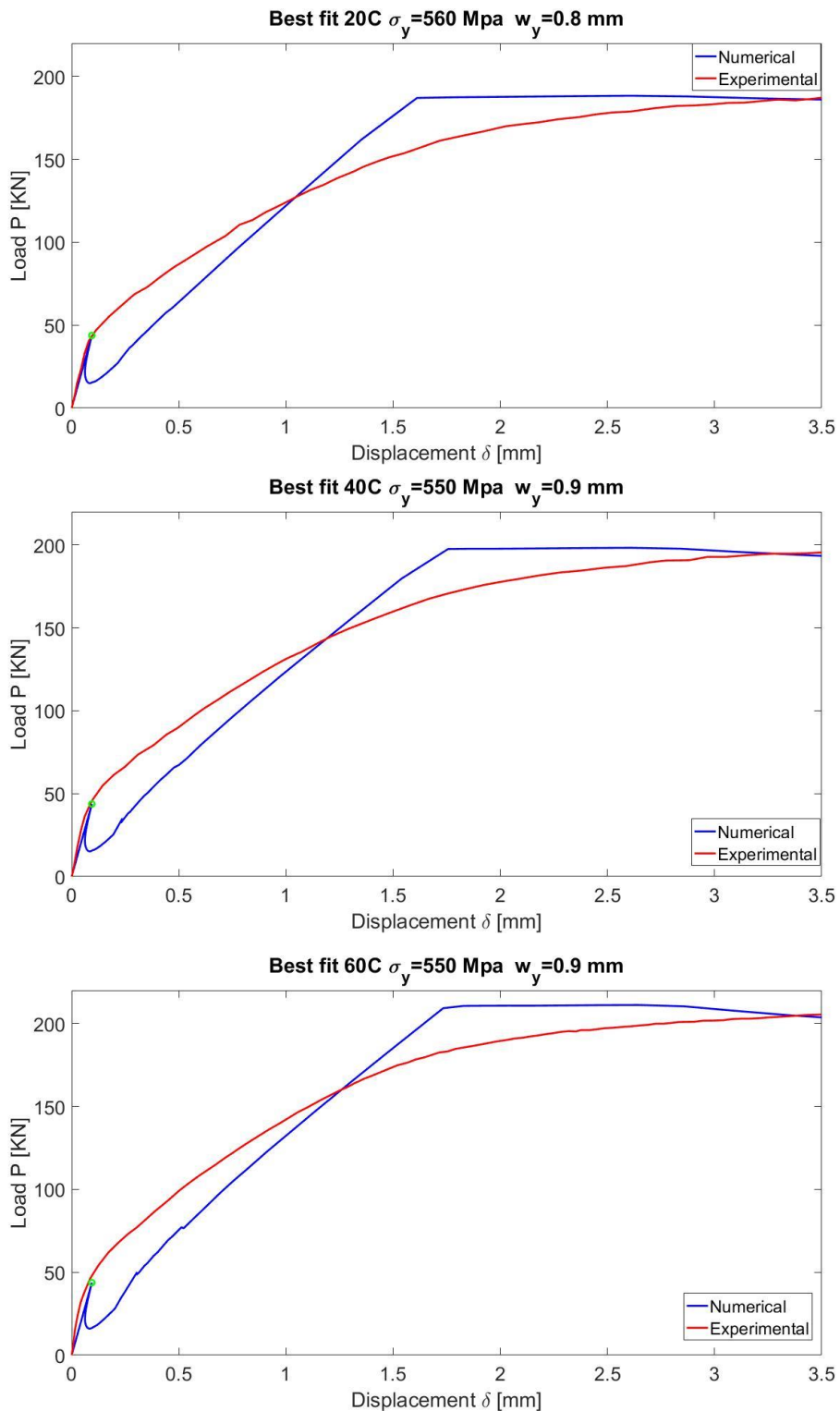


Figure 5.5 Best fitting for curves C (bar reinforcement 2Φ12), respectively with 20, 40 and 60 kg/m³ of fibre content

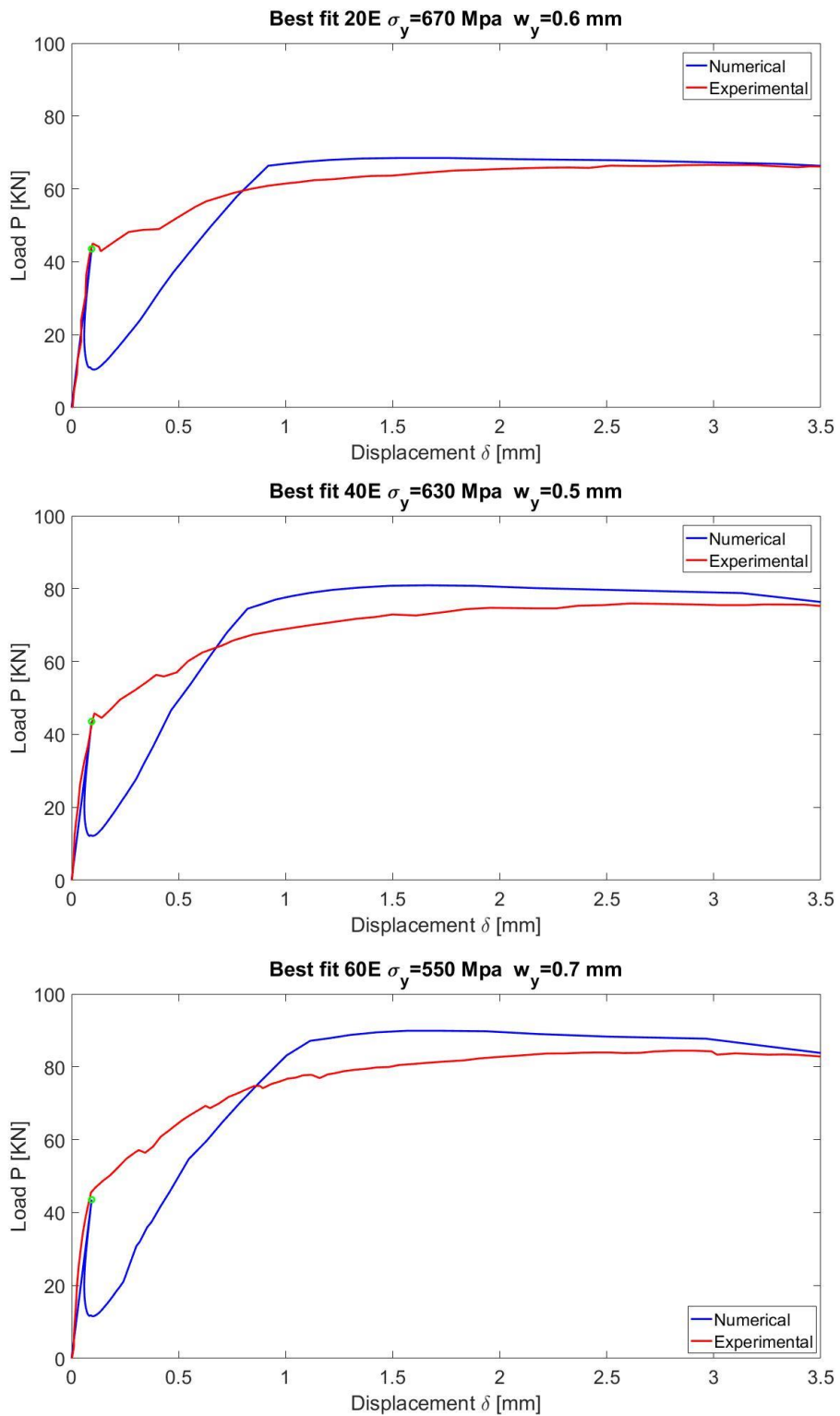


Figure 5.6 Best fitting for curves E (bar reinforcement 2Φ6), respectively with 20,40 and 60 kg/m³ of fibre content

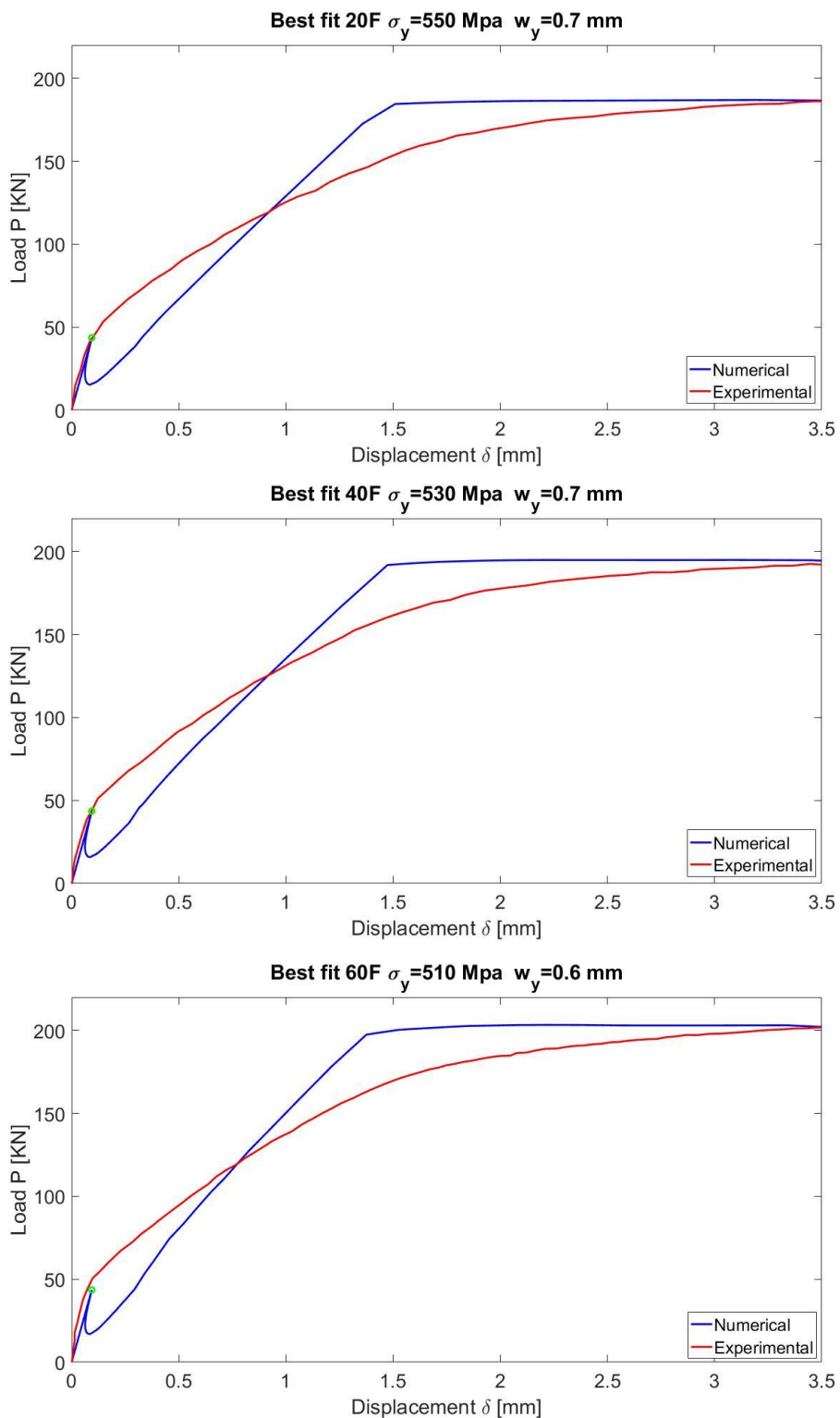


Figure 5.7 Best fitting for curves F (bar reinforcement 2Φ12), respectively with 20,40 and 60 kg/m³ of fibre content

The identifying parameters are collected in Table from 5.4 to 5.7:

ID	w_y	σ_y
20 B	0.7	730
40 B	1	730
60 B	1	640
AVG	0.9	700

Table 5.4 Average value of mechanical parameters

ID	w_y	σ_y
20 C	0.8	560
40 C	0.9	550
60 C	0.9	550
AVG	0.87	553

Table 5.5 Average value of mechanical parameters

ID	w_y	σ_y
20 E	0.6	670
40 E	0.5	630
60 E	0.7	550
AVG	0.6	616

Table 5.6 Average value of mechanical parameters

ID	w_y	σ_y
20 F	0.7	550
40 F	0.7	530
60 F	0.6	510
AVG	0.67	530

Table 5.7 Average value of mechanical parameters

- **PREDICTION**

using the average parameters obtained from the best fitting procedure, the $P - \delta$ experimental curves of the HRC elements were reproduced and are showed in following figures.

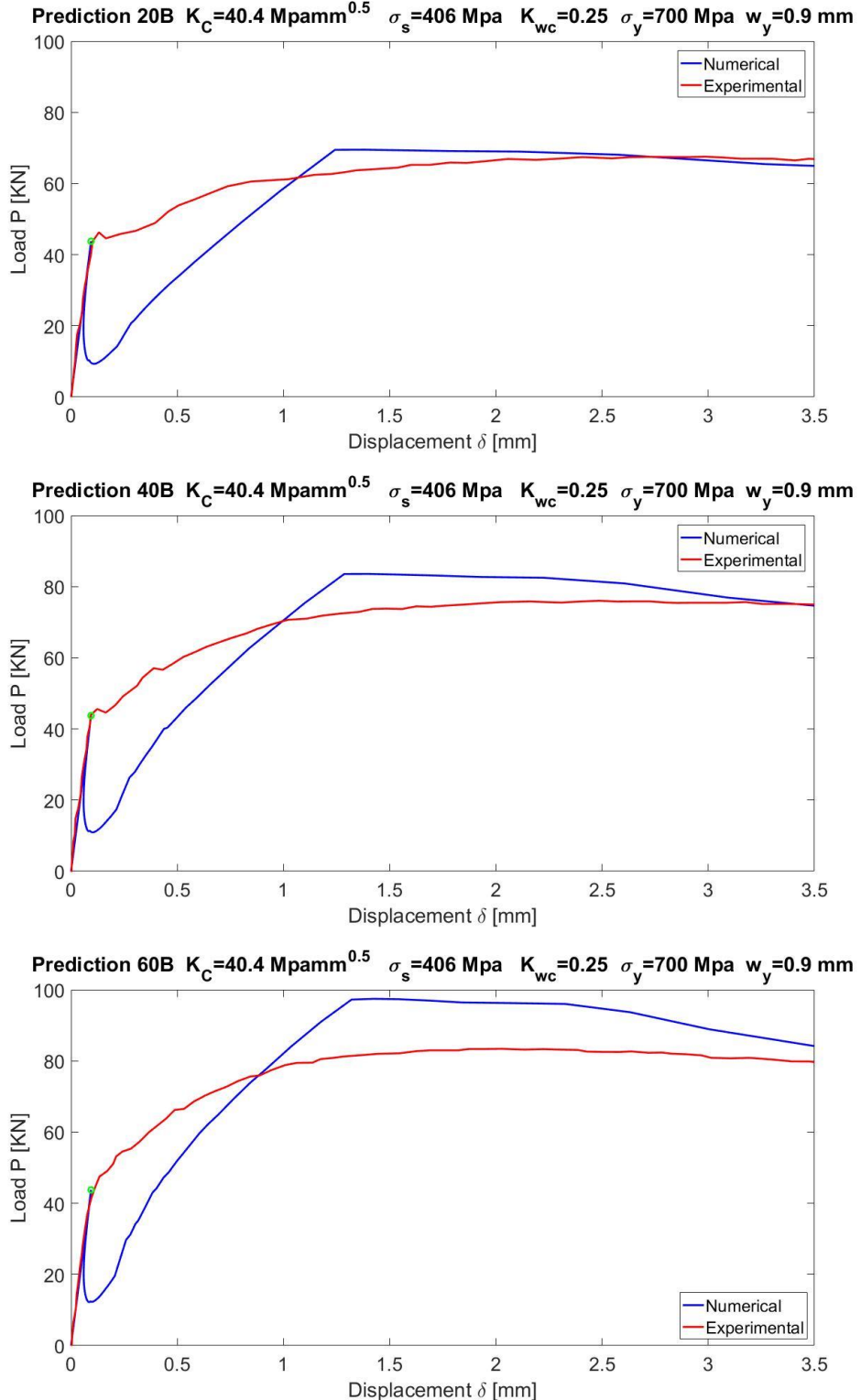


Figure 5.8 Predictions for curves B (bar reinforcement 2Φ6), respectively with 20, 40 and 60 kg/m³ of fibre content

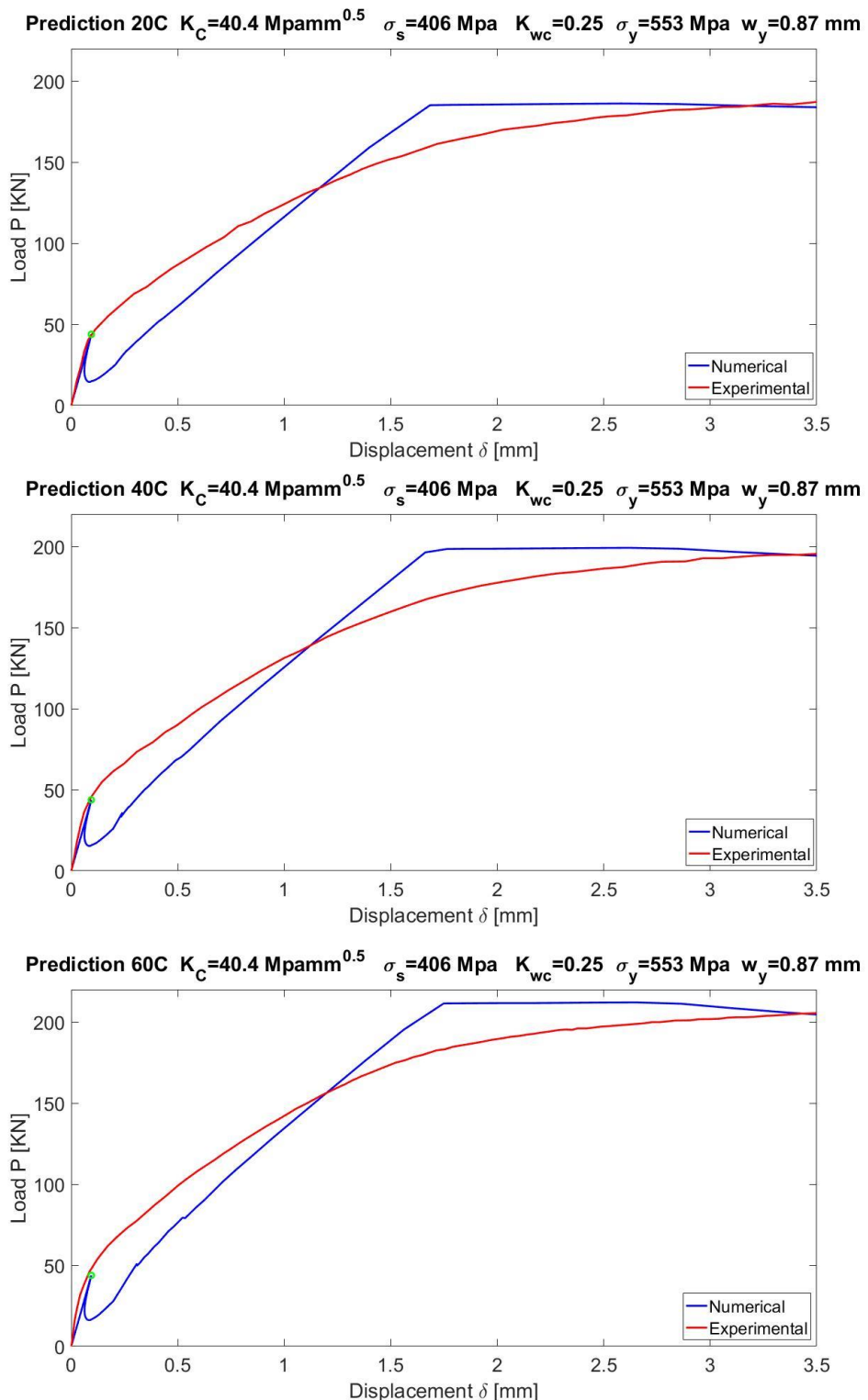


Figure 5.9 Predictions for curves C (bar reinforcement 2Φ12), respectively with 20, 40 and 60 kg/m³ of fibre content

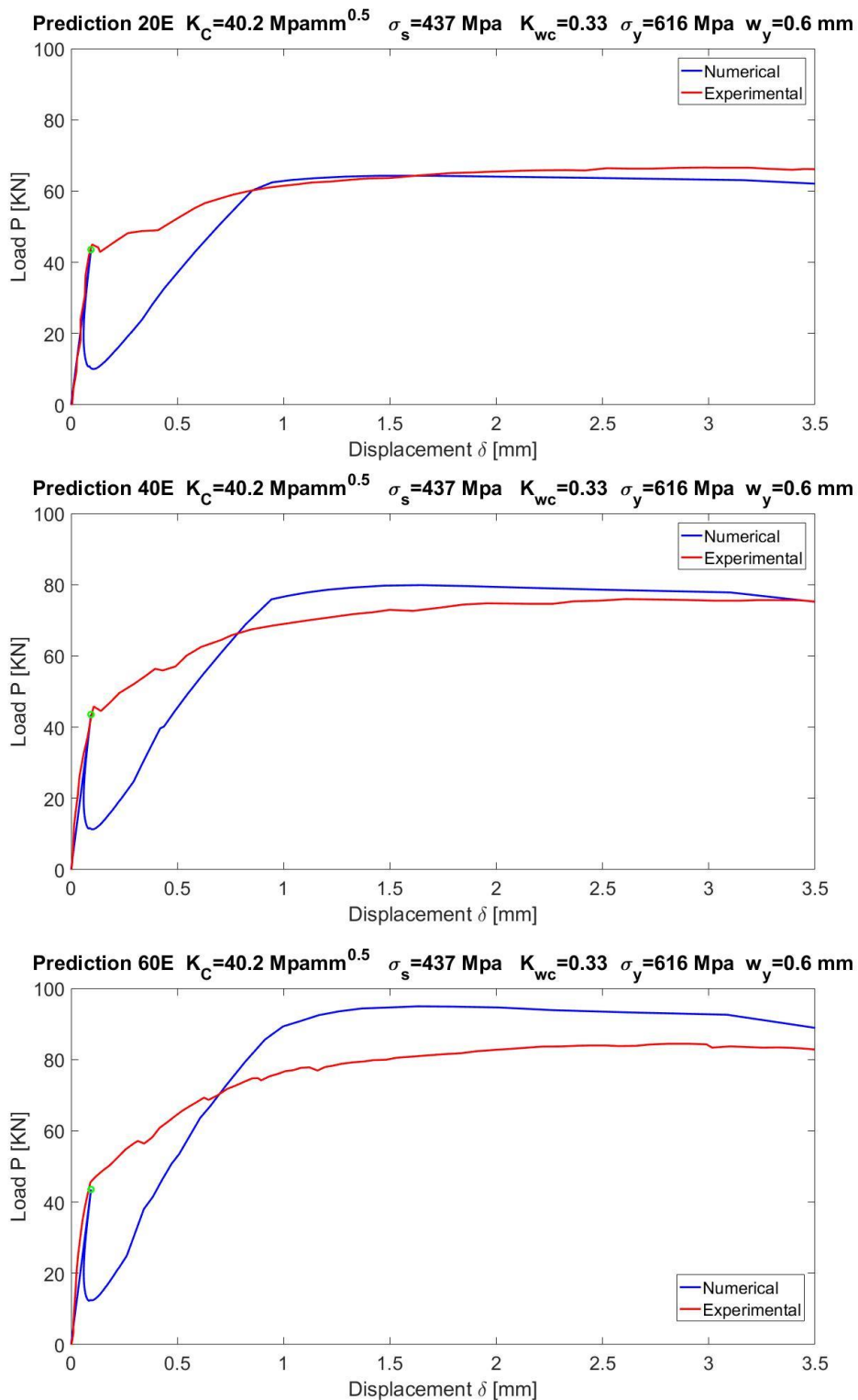


Figure 5.10 Predictions for curves E (bar reinforcement 2Φ6), respectively with 20,40 and 60 kg/m³ of fibre content

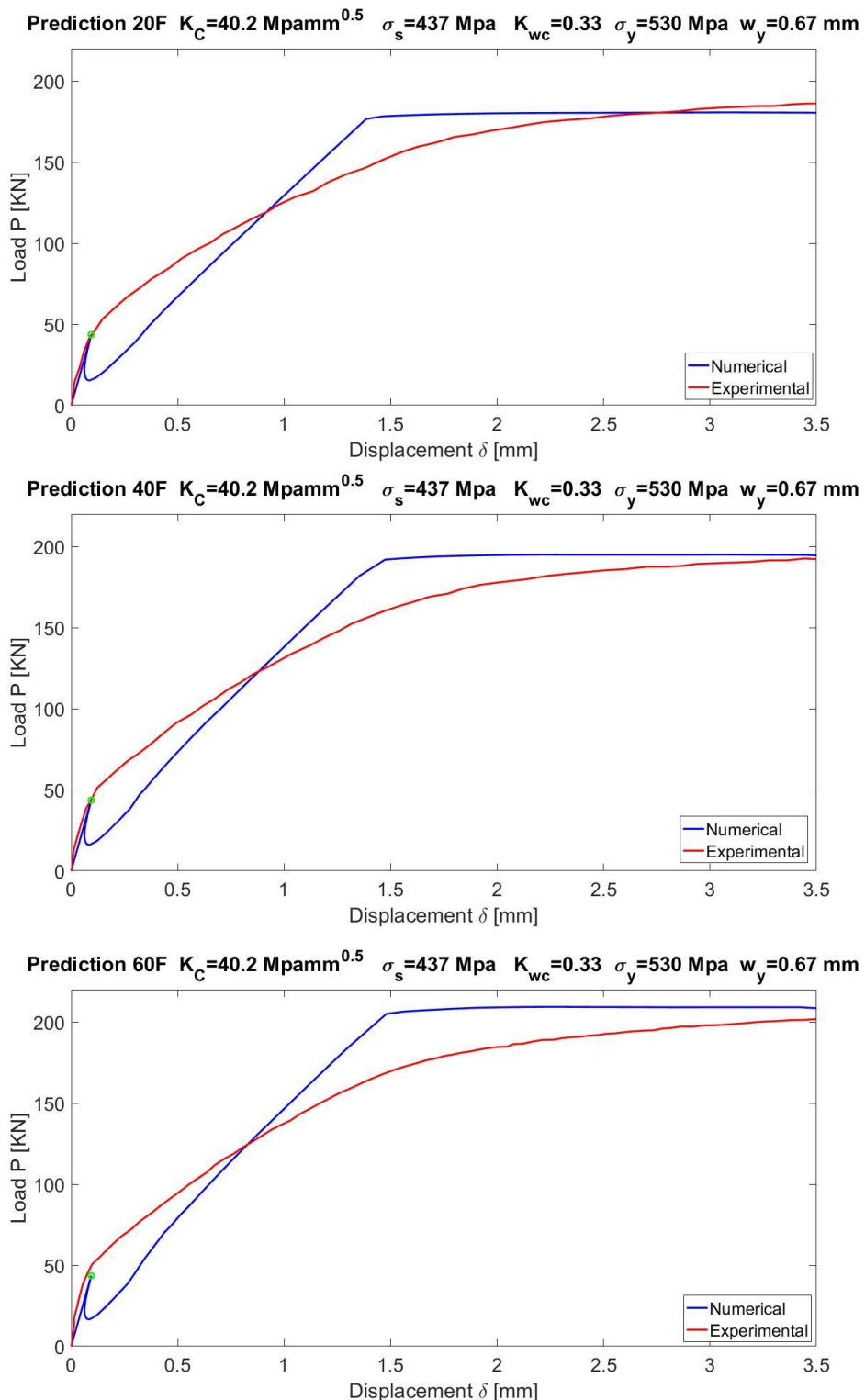


Figure 5.11 Predictions for curves F (bar reinforcement 2Φ12), respectively with 20,40 and 60 kg/m³ of fibre content

5.2.2 Mobasher et al. experimental work

In the experimental campaign conducted by Mobasher et al. (2015), the influences of geometry and tensile strength of fibres as well as the effects of different reinforcement ratios were investigated. The fibre contents were 25, 50 and 60 Kg\m³. Normal strength concrete used fibre type RC 65/60 BN at 25 and 50 Kg\m³ while HSC used fibre type RC 80/60 BP at 60 Kg\m³. Instead, the steel bars reinforcement percentages used were 0.00, 0.25, 0.56 and 1.00% for a total of 12 beams studied. All beams had a cross section of 0.20x0.20 m, with two different span lengths of 1.0 and 2.0 m. To determine the fracture parameters of the HRC composite, unnotched beams were tested under four point loading according to full scale beam test from Brite/Euram project BRPR-CT98_0813.

In the following, the main variables of the experimental campaign, including the results, are summarized.

- **MATERIALS**

- **Matrix**

There are two different mixtures of concrete used in this work: a normal (NSC) and an high strength concrete (HSC). Normal strength concrete used fibre type RC 65/60 BN at 25 and 50 Kg\m³ while HSC used fibre type RC 80/60 BP at 60 Kg\m³.

- **Fibre**

Steel hooked-end Fibres (SF) were used. Their mechanical and geometrical properties, and their volume ratio are reported in Tables 5.9.

Fibre diameter	d_f	[mm]	0.75
Fibre length	l_f	[mm]	35
Fibre aspect ratio	λ	[$-$]	47
Fibre tensile strength	f_u	[MPa]	1100

Table 5.8 Fibre mechanical and geometrical properties.

Table 5.10 provides the details of the 12 beam series.

Beam test series.

Beam	Mix	Fiber content (kg/m ³)	Span (m)	Rebar
B1	NSC	25	1.0	–
B2	NSC	25	2.0	–
B3	NSC	50	1.0	–
B4	NSC	50	2.0	–
B5	HSC	60	1.0	–
B6	HSC	60	2.0	–
B7	NSC	25	1.0	2-φ8
B8	NSC	25	2.0	2-φ8
B9	NSC	50	1.0	2-φ12
B10	NSC	50	2.0	2-φ12
B11	HSC	60	1.0	2-φ16
B12	HSC	60	2.0	2-φ16

Table 5.9 details of beam series

- TEST SETUP

Normal strength concrete reinforced with fibre type RC 65/60 BN at 25 and 50 Kg\m³ while HSC used fibre type RC 80/60 BP at 60 Kg\m³. All beams had a cross section of 0.20x0.20 m, with two different span lengths of 1.0 and 2.0 m and tested under four point bending set up with a constant spacing between the two point loads at 0.2 m. the first half of the series (B1-B6) contains no rebar and the other half contained two rebars of size 8, 12 and 16 mm. Steel parameters were Young's modulus of 200 GPa and a concrete cover of 15 mm. The specimens are unnotched, so during the modelling will be considered a fictitious initial notch of:

$$\frac{a_0}{h} = 0.05 = 10 \text{ mm}$$

And the bar's concrete cover is equal to 15 mm, so:

$$\frac{c_0}{h} = 0.075 = 15 \text{ mm}$$

A scheme of the test setup is shown in Fig. 5.12.

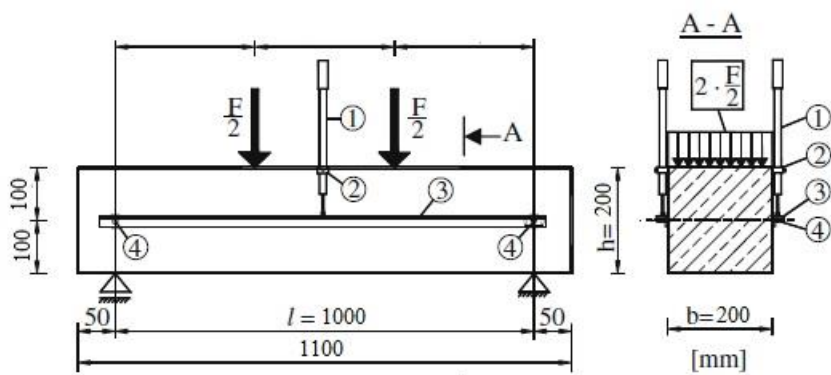


Figure 5.12 FPBT setup on specimen, Mobasher (2015)

➤ Part 1 (FRC)

For each experimental $P - \delta$ curves of the FRC elements, a best fitting procedure was applied in order to defining the average values of K_{IC} , σ_s , and w_c .

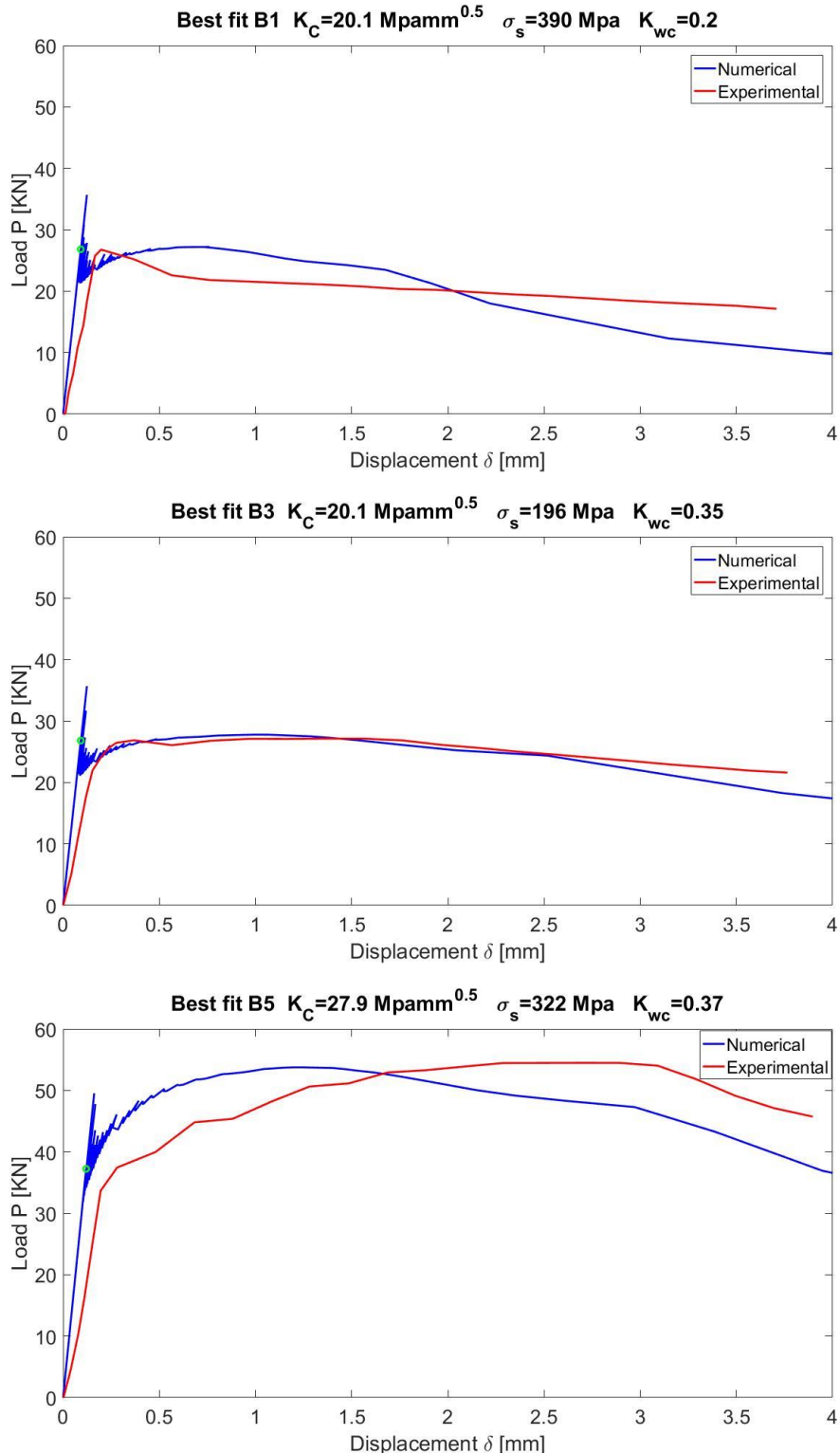


Figure 5.13 Best fitting for curves B1, B3 and B5, respectively with 25, 50 and 60 kg/m³ of fibre content

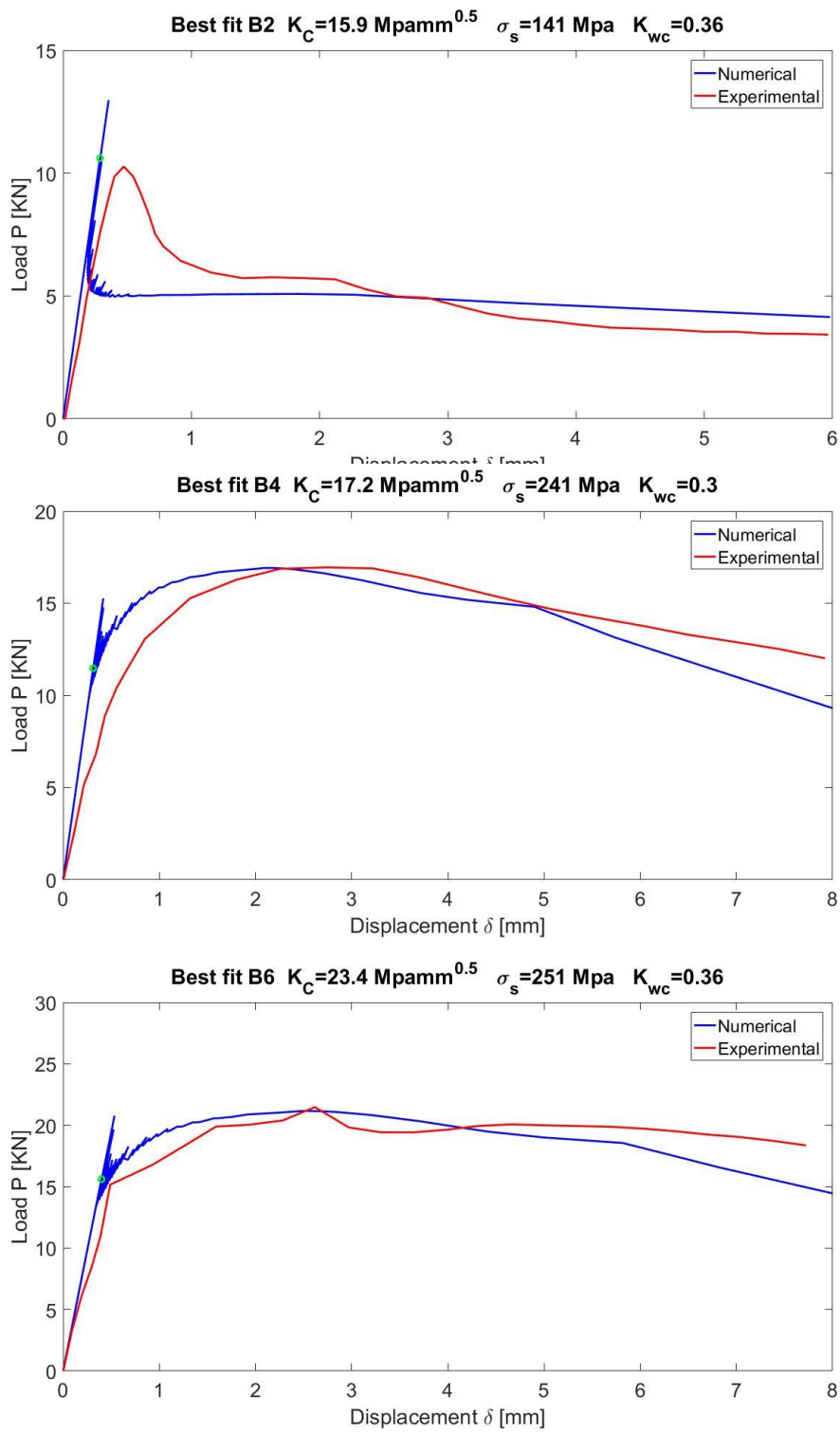


Figure 5.14 Best fitting for curves B2, B4 and B6, respectively with 25, 50 and 60 kg/m³ of fibre content

ID	σ_s	K_{wc}
B1	385	0.20
B3	190	0.40
B5	320	0.38
B2	150	0.30
B4	240	0.30
B6	251	0.36
AVG	256	0.32

Table 5.10 Average value of mechanical parameters

ID	K_{IC}	AVG
B1	20.1	18.3
B3	20.1	
B2	15.9	
B4	17.2	
B5	27.9	25.7
B6	23.4	

Table 5.11 Average value of fracture toughness

➤ Part 2 (HRC)

For each experimental $P - \delta$ curves of the HRC elements, a best fitting procedure was applied in order to defining the average values of σ_y , and w_y

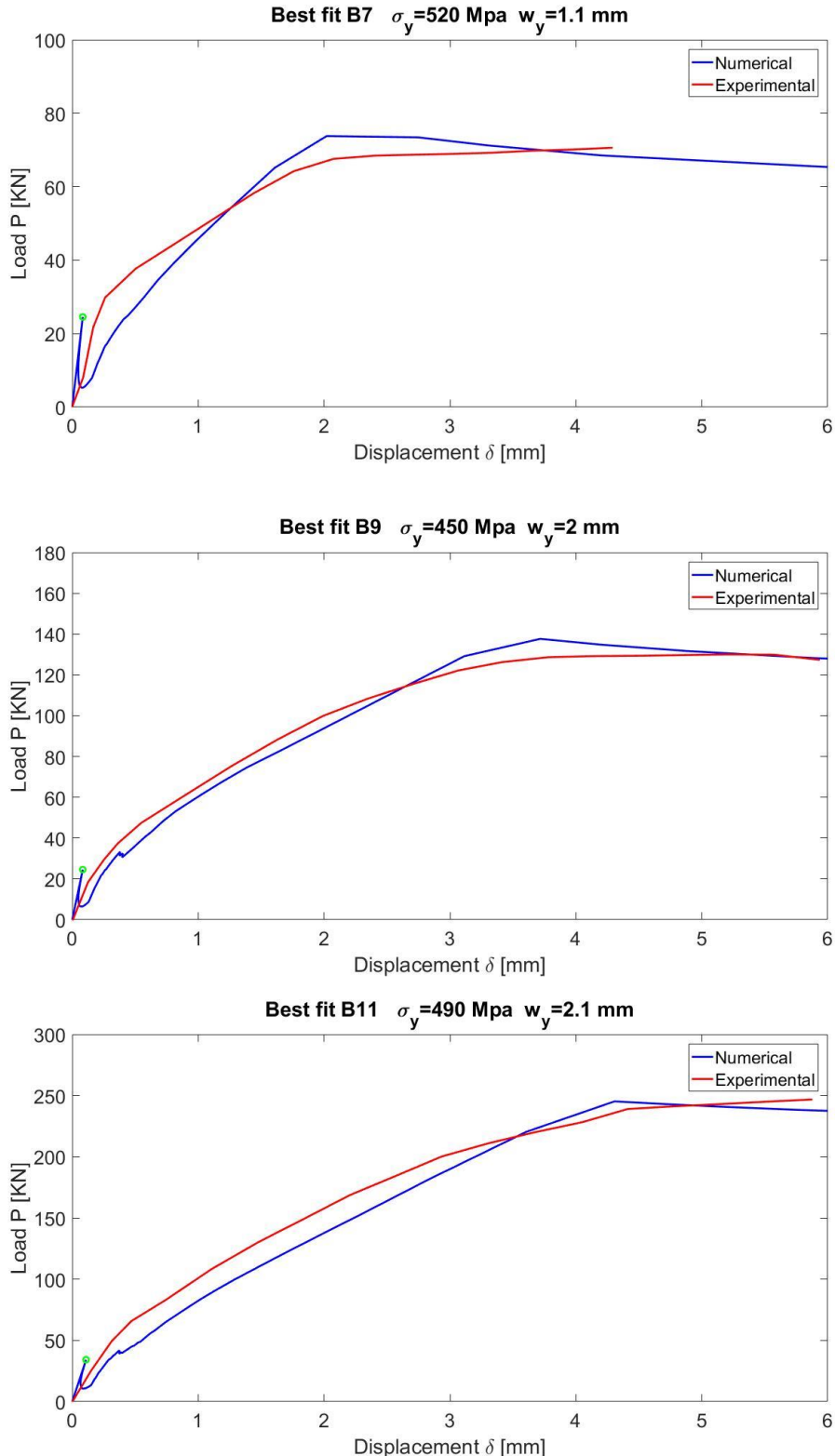


Figure 5.15 Best fitting for curves B7, B9 and B11 , respectively with 25,50 and 60 kg/m³ of fibre content

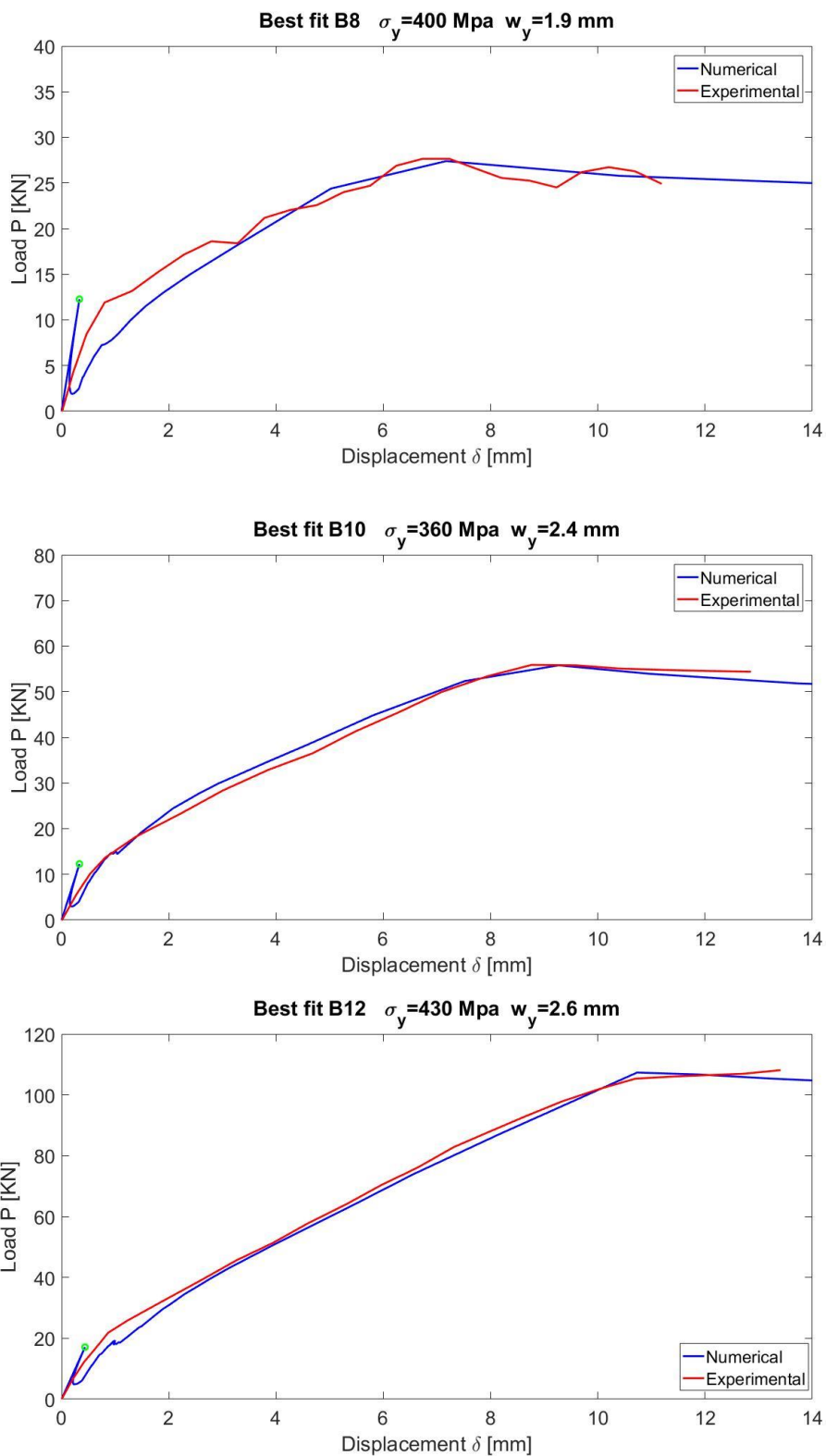


Figure 5.16 Best fitting for curves B8, B10 and B12 , respectively with 25,50 and 60 kg/m³ of fibre content

The identifying parameters are collected in Tables 5.12 and 5.13:

ID	w_y	σ_y
B7	1.1	520
B9	2	450
B11	2.1	490
AVG	1.7	487

Table 5.12 Average value of mechanical parameters

ID	w_y	σ_y
B8	1.9	380
B10	2.4	360
B12	2.6	430
AVG	2.3	390

Table 5.13 Average value of mechanical parameters

- **PREDICTION**

using the average parameters obtained from the best fitting procedure, the $P - \delta$ experimental curves of the HRC elements were reproduced and are showed in following figures.

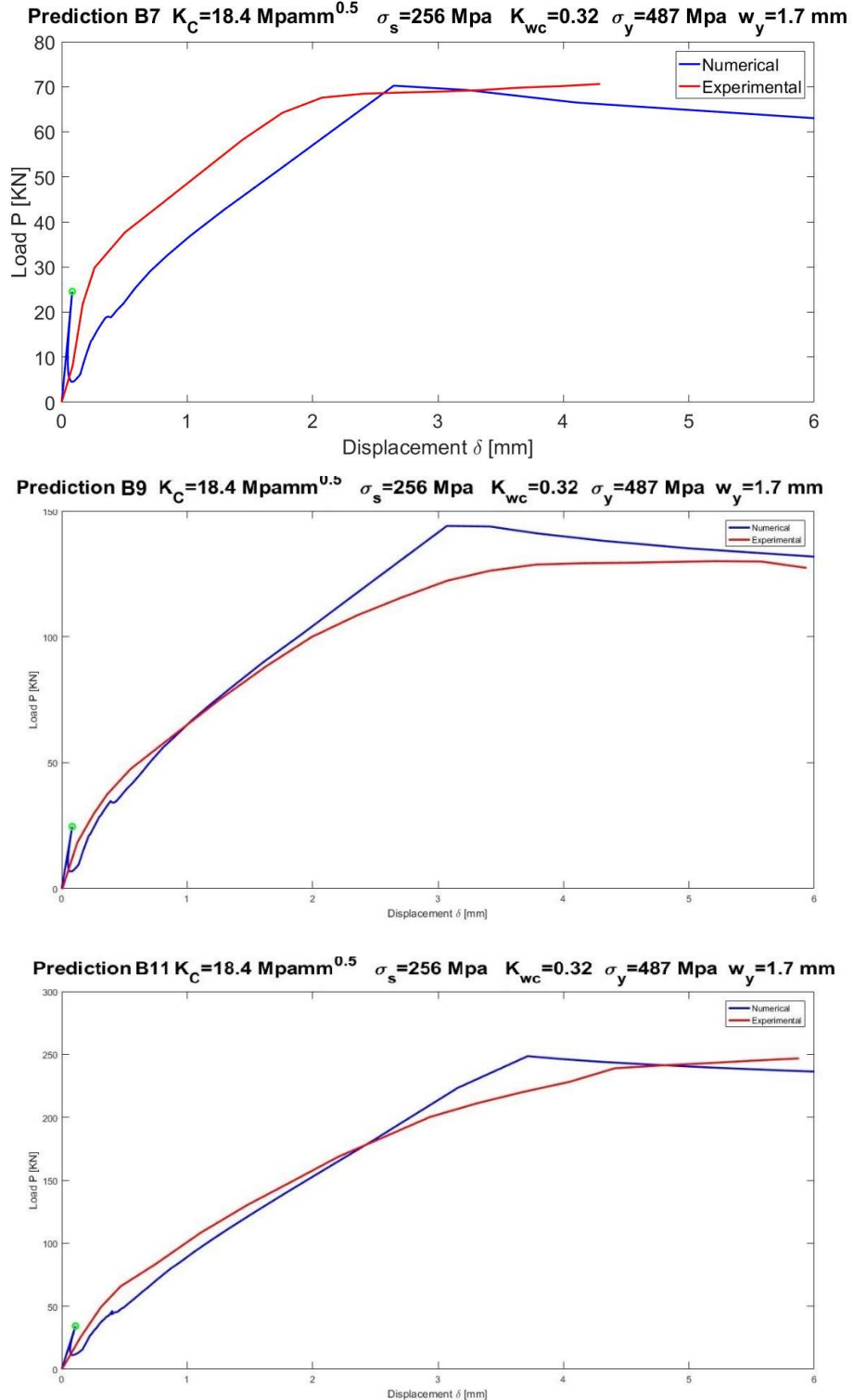


Figure 5.17 Predictions for curves B7(2Φ8), B9(2Φ12), B11(2Φ16), respectively with 25, 50 and 60 kg/m³ of fibre content

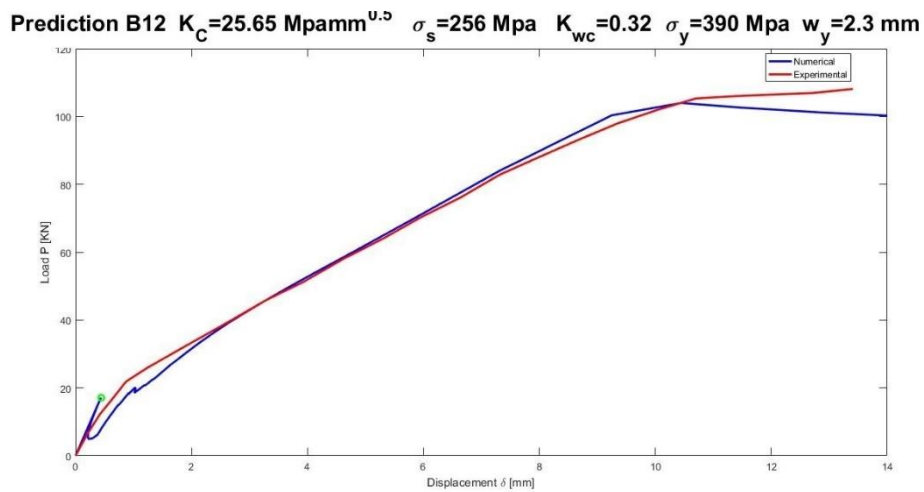
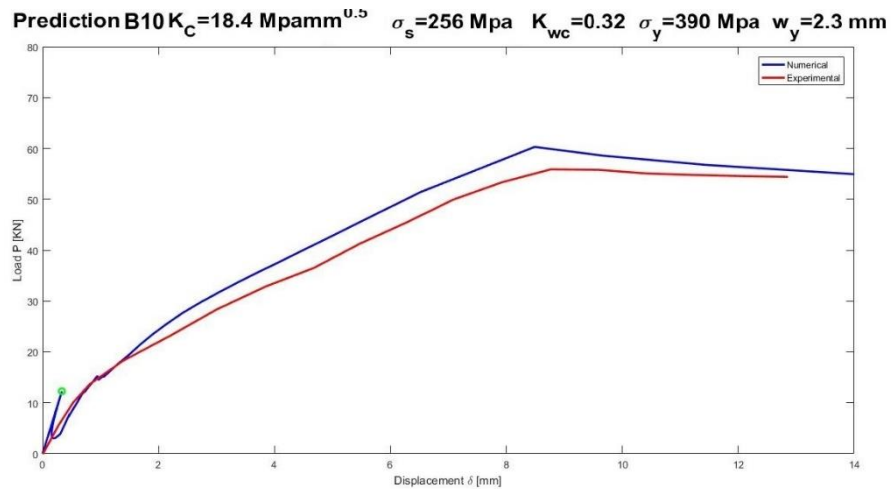
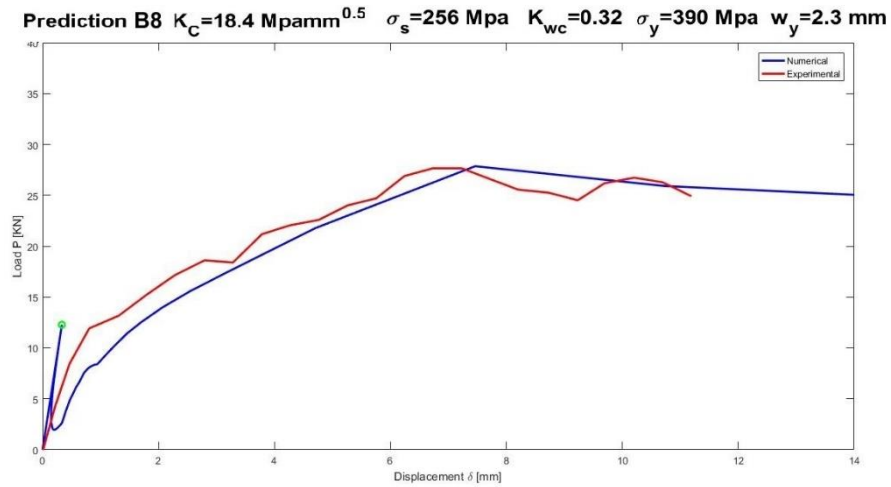


Figure 5.18 Predictions for curves B8(2Φ8), B10(2Φ12), B12(2Φ16), respectively with 25,50 and 60 kg/m³ of fibre content

5.2.3 Fantilli et al. experimental work

In the experimental campaign conducted by Fantilli et al. (2020), the influence of geometry and tensile strength of fibres as well as the effects of different reinforcement ratios was investigated. The fibre contents were 0.00, 0.50 and 0.75% for two different type of fibres (Type 1 and Type2). Instead, the steel bars reinforcement percentages used was 0.00 and 0.12%; for each combination were tested 3 beams for a total of 24 beams studied. To determine the fracture parameters of the HRC composite, unnotched beams were tested under three point loading using an MTS testing machine.

In the following, the main variables of the experimental campaign, including the results, are summarized.

- MATERIALS

- Matrix

The matrix mixture presents a compressive strength of 50 Mpa.

- Fibre

Two type of Steel hooked-end Fibres (SF) were used. Their mechanical and geometrical properties, and their volume ratio are reported in Tables 5.14.

			Type 1	Type 2
Fibre diameter	d_f	[mm]	0.38	0.71
Fibre length	l_f	[mm]	30	60
Fibre aspect ratio	λ	[-]	79	84
Fibre tensile strength	f_u	[MPa]	3070	2600

Table 5.14 Fibre mechanical and geometrical properties.

- TEST SETUP

The beams were tested in three-point bending test by using an MTS testing machine. As linear supports (at distance of 600 mm), and for the application of load as well, steel cylinders were used. A load cell of 100 kN was used to apply the load P , and two LVDT's measured the midspan deflection δ on the two sides of the beam (deprated by the support settlements). The bending test were performed under displacement control, at the velocity of 0.08 mm per minute up to the maximum load. Afterword, the velocity increased to 0.20 mm per minute.

Six small beams ($15 \times 15 \times 70 \text{ cm}$) were casted for each fibre content. Among them three were with steel bar reinforcement ratios of 0.12% and six beams without steel reinforcement. The distance between the bottom edge of the reinforcing steel and the concrete surface was 1.5 cm. The hardened properties of the mixture were tested 28 days after casting. The specimens are unnotched, so during the modelling will be considered a fictitious initial notch of:

$$\frac{a_0}{h} = 0.05 = 7.5 \text{ mm}$$

And the bar's concrete cover is equal to 15 mm, so:

$$\frac{c_0}{h} = 0.10 = 15 \text{ mm}$$

A scheme of the test setup is shown in Fig. 5.19.

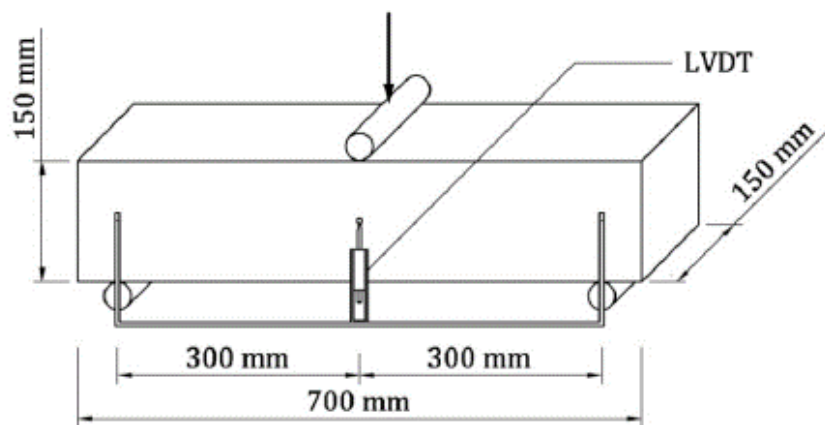


Figure 5.19 FPBT setup on specimen, Fantilli (2020)

- IDENTIFICATION

- Part 1 (FRC)

For each experimental $P - \delta$ curves of the FRC elements, a best fitting procedure was applied in order to defining the average values of K_{IC} , σ_s , and w_c .

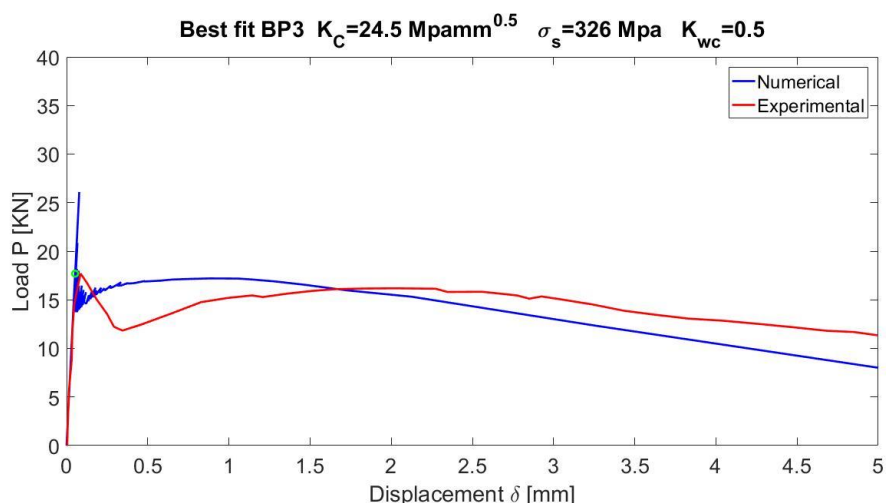
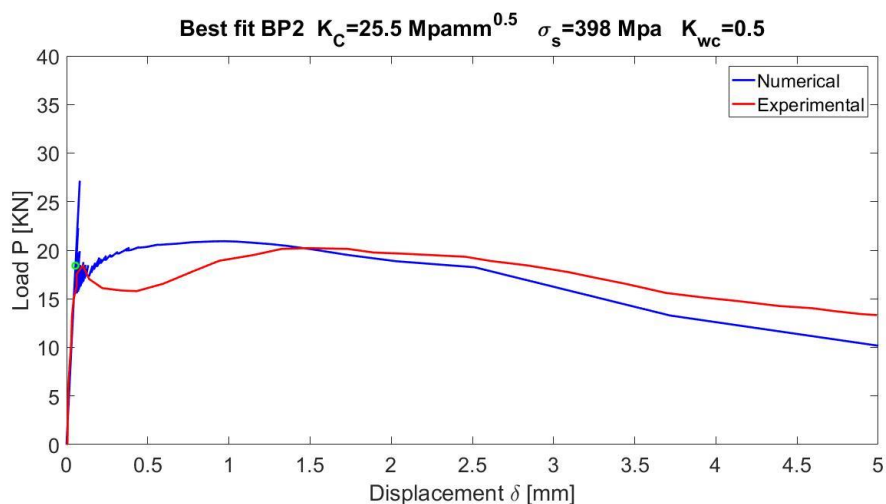
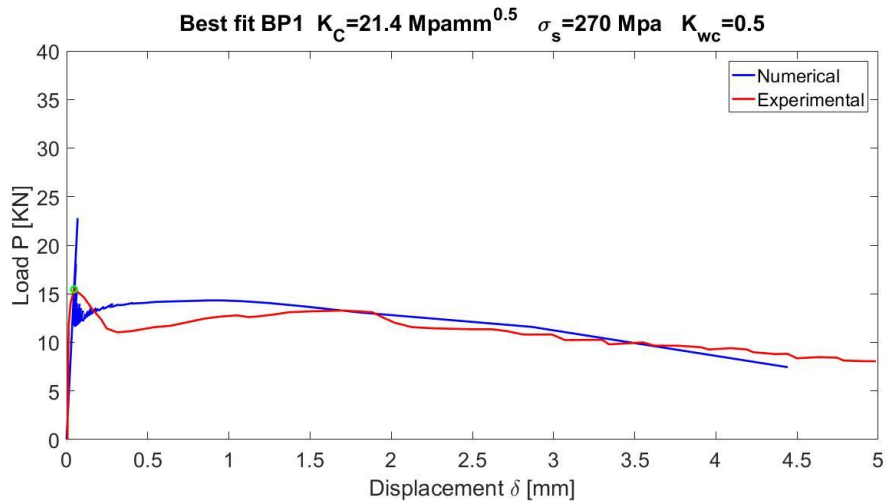


Figure 5.20 Best fitting for curves serie BP

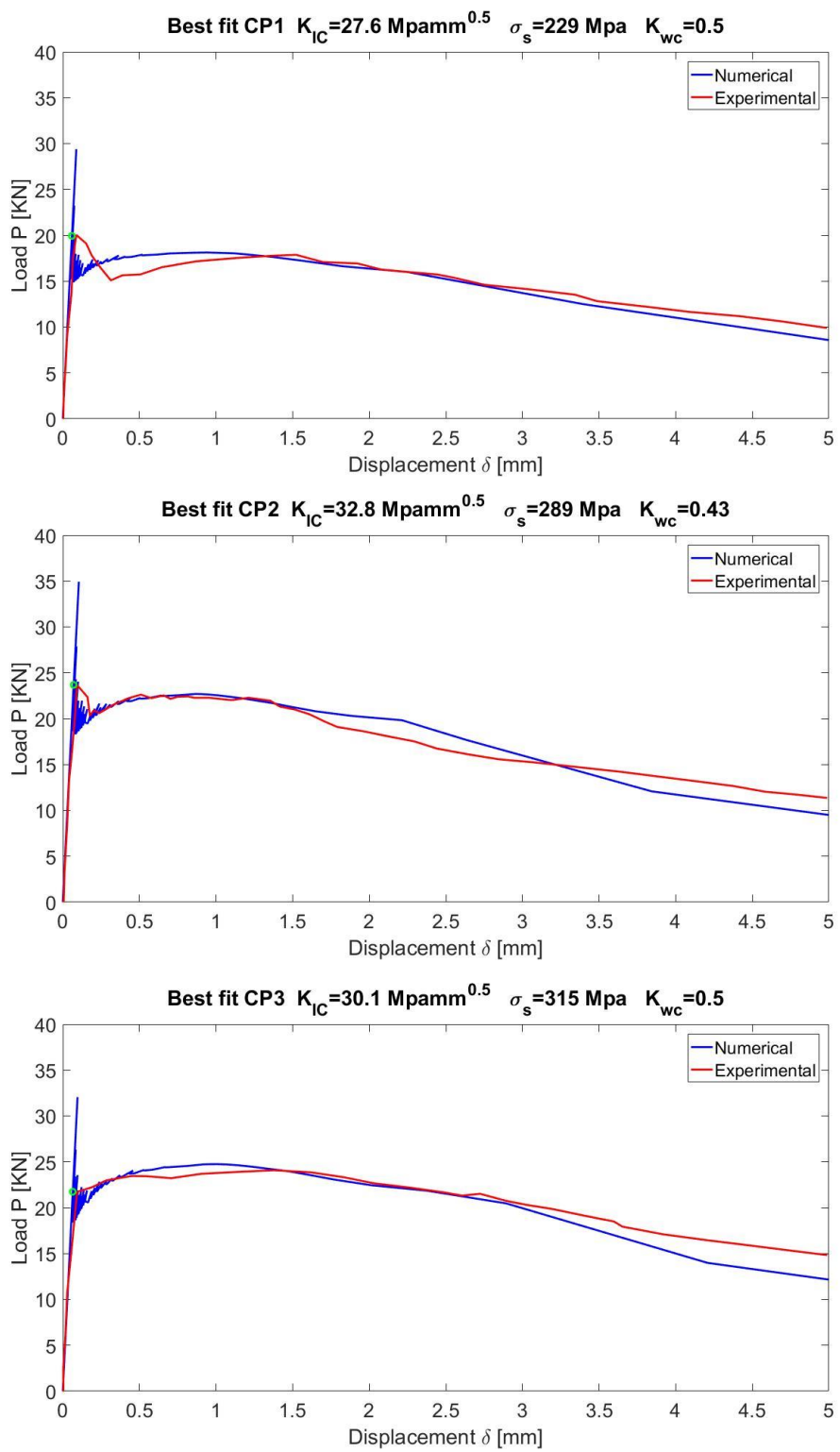


Figure 5.21 Best fitting for curves serie CP

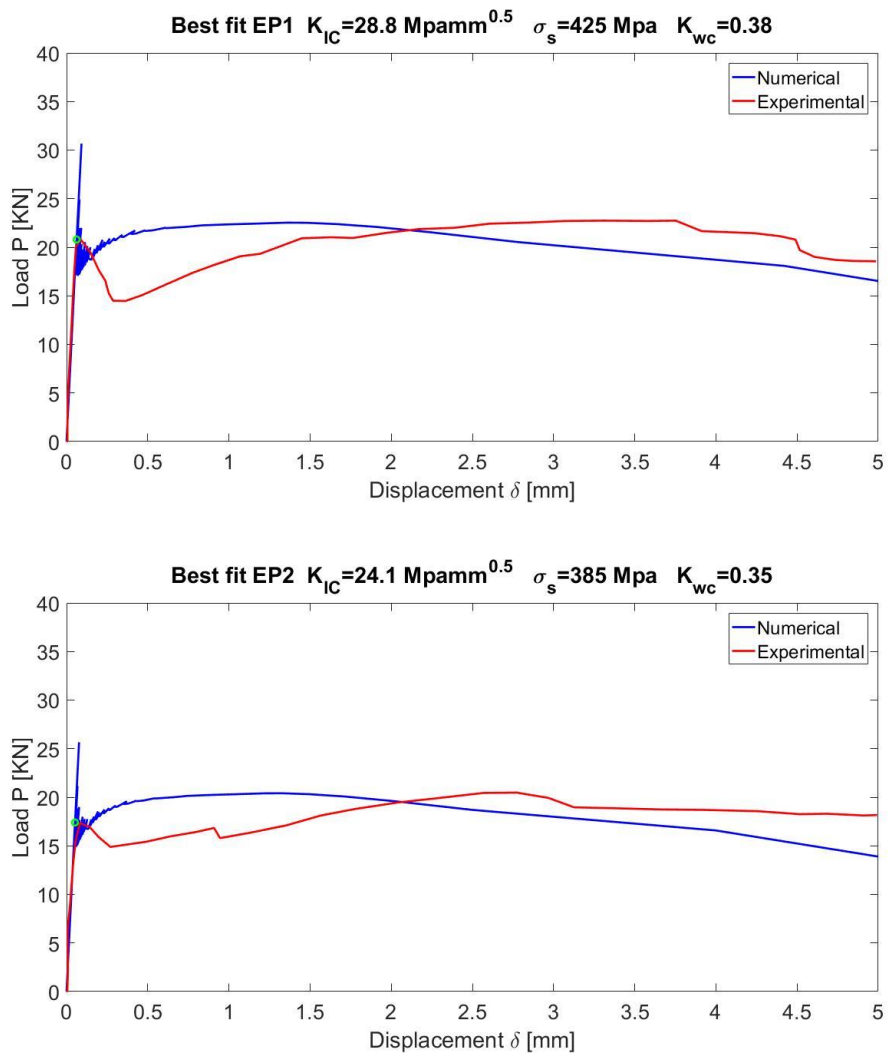


Figure 5.22 Best fitting for curves serie EP

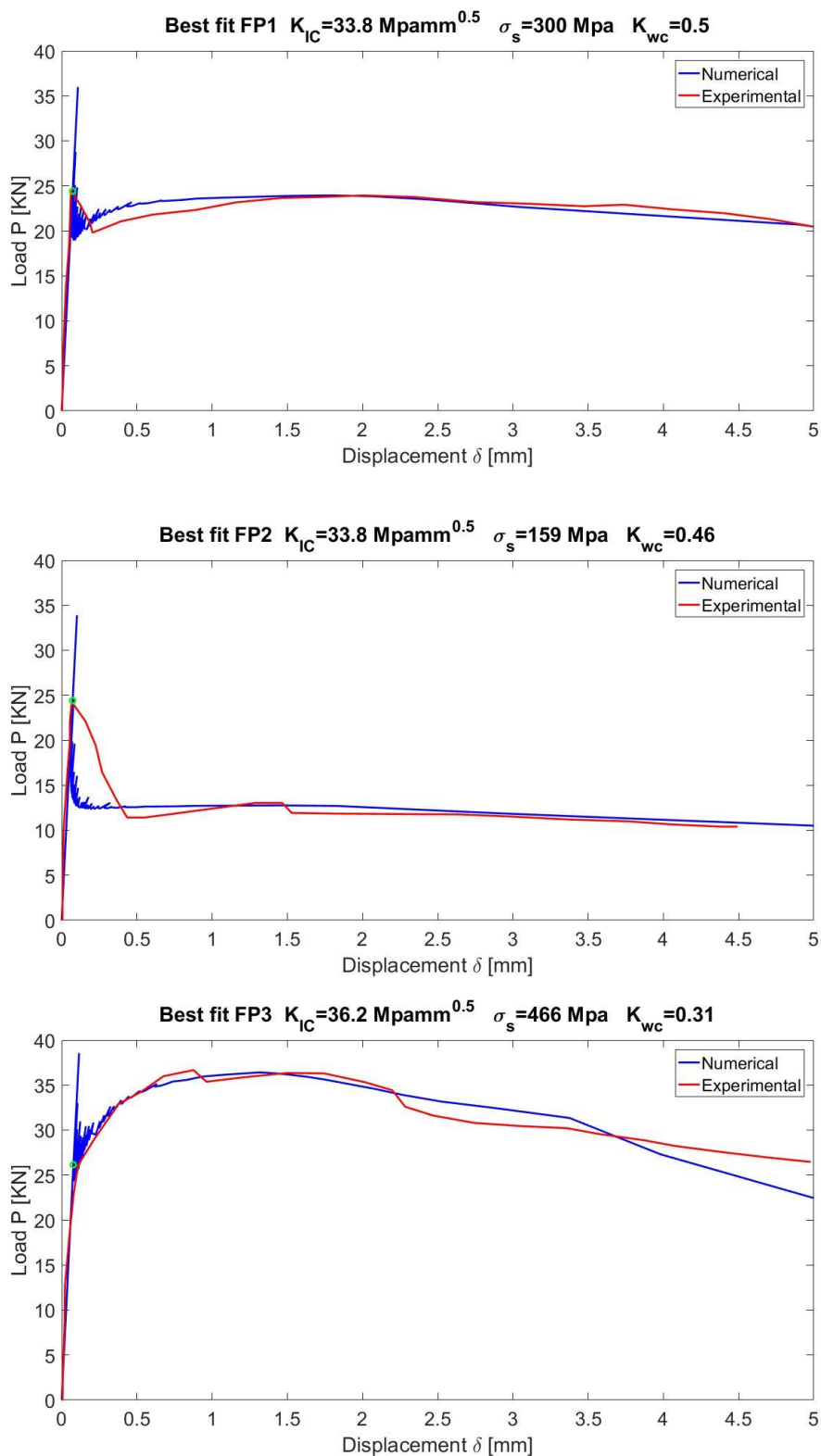


Figure 5.23 Best fitting for curves serie FP

The identifying parameters are collected in Tables 5.15 and 5.16:

ID	K _{IC}	σ_s	K _{wc}
BP1	21.4	270	0.50
BP2	25.5	398	0.50
BP3	24.5	326	0.50
CP1	27.6	229	0.50
CP2	32.8	289	0.43
CP3	30.1	315	0.5
AVG	27.0	305	0.49

Table 5.15 Average value of mechanical parameters

ID	K _{IC}	σ_s	K _{wc}
EP1	28.8	425	0.38
EP2	24.1	385	0.35
EP3	-	-	-
FP1	33.8	300	0.50
FP2	33.8	159	0.46
FP3	36.2	466	0.31
AVG	31.3	347	0.40

Table 5.16 Average value of mechanical parameters

➤ Part 2 (HRC)

For each experimental $P - \delta$ curves of the HRC elements, a best fitting procedure was applied in order to defining the average values of σ_y , and w_y

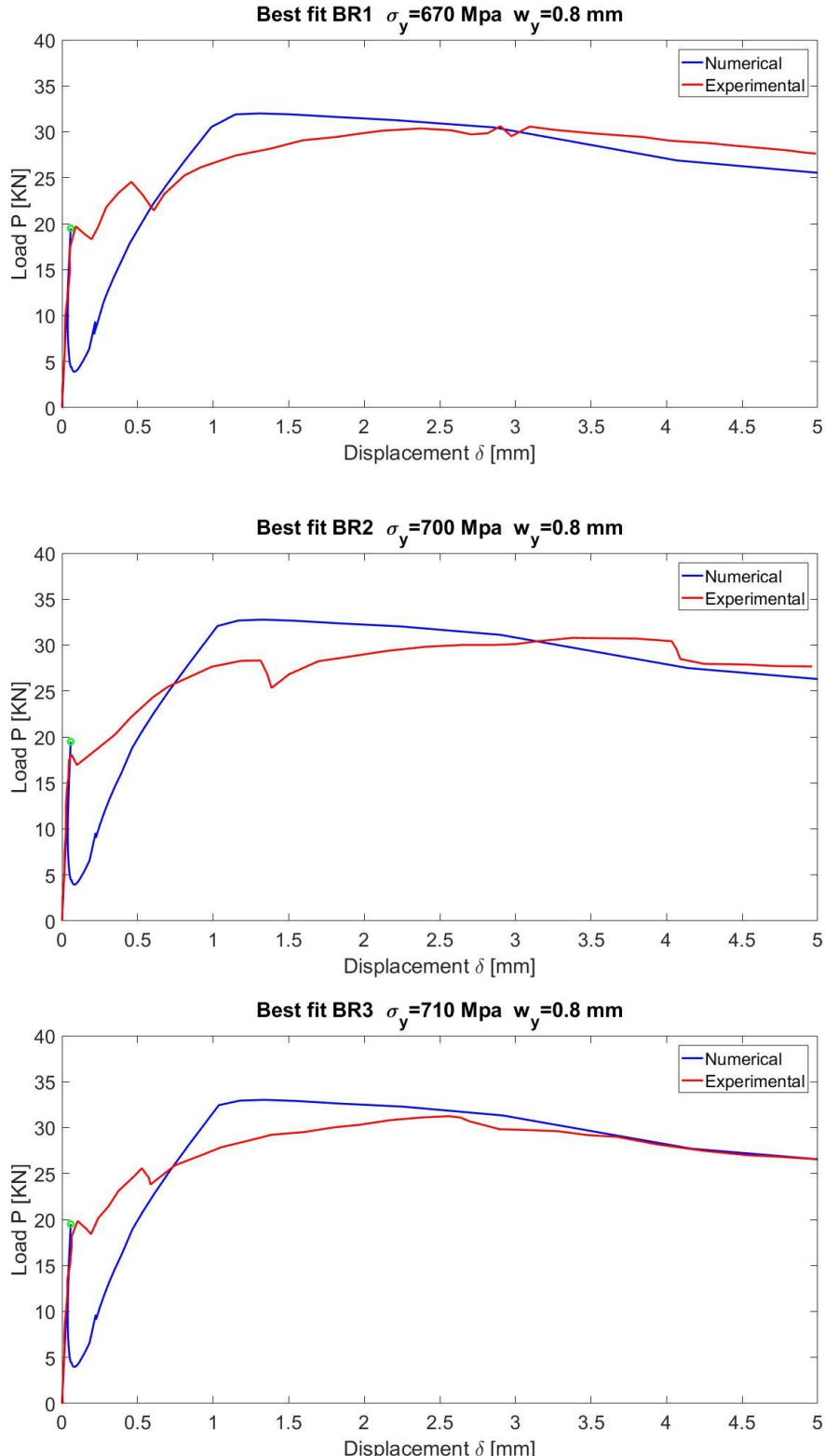


Figure 5.24 Best fitting for curves serie BR

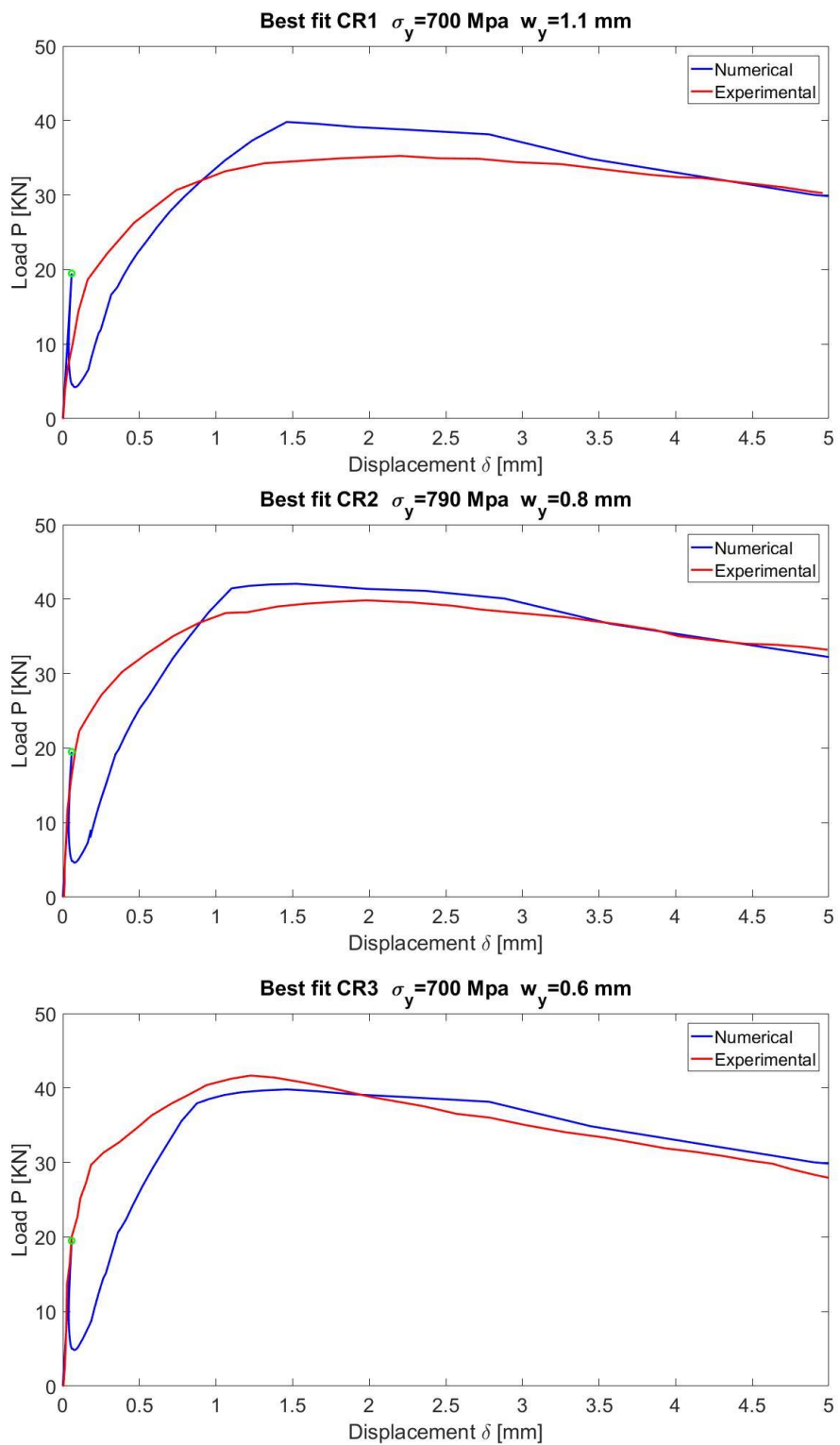


Figure 5.25 Best fitting for curves serie CR

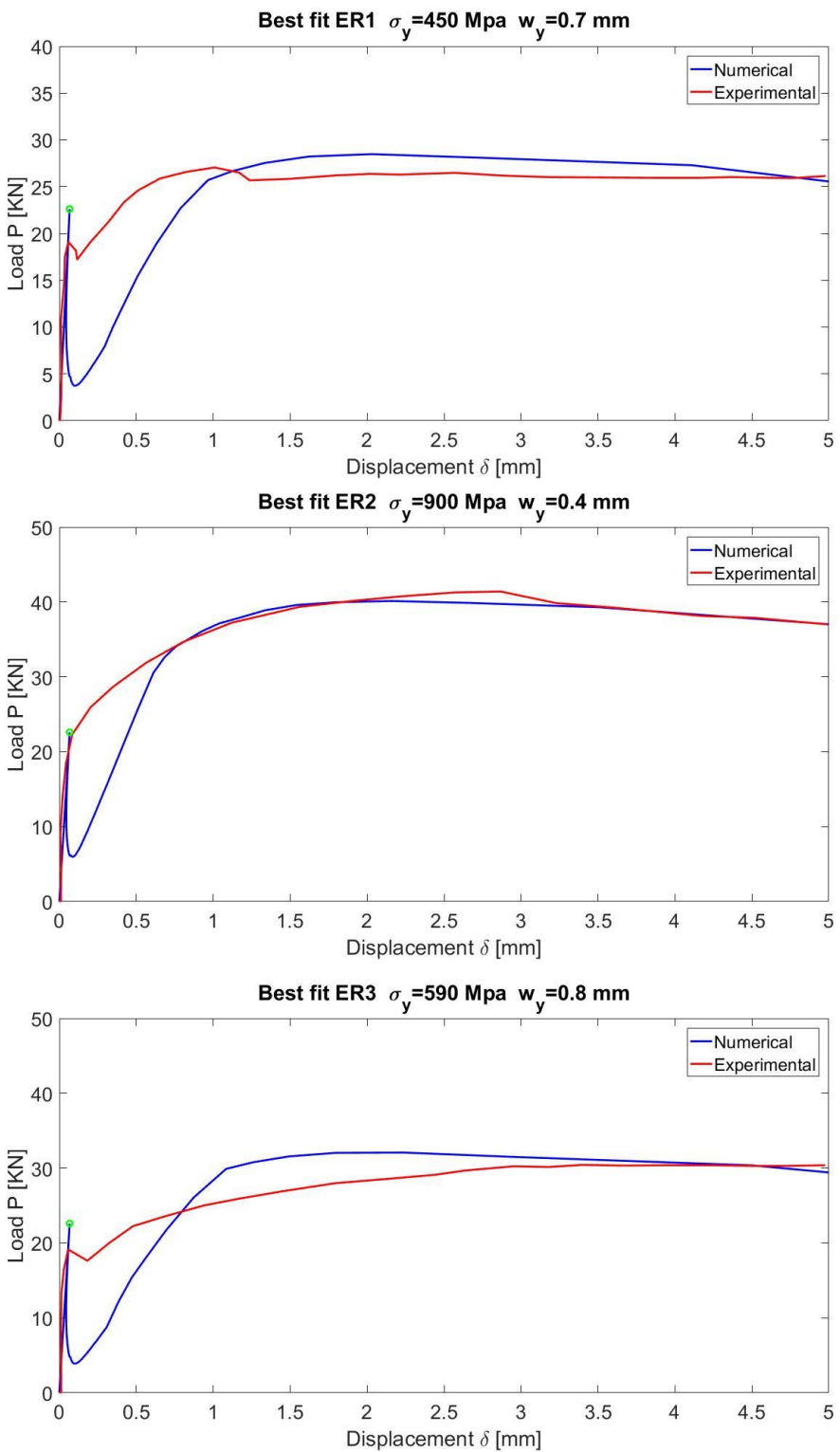


Figure 5.26 Best fitting for curves serie ER

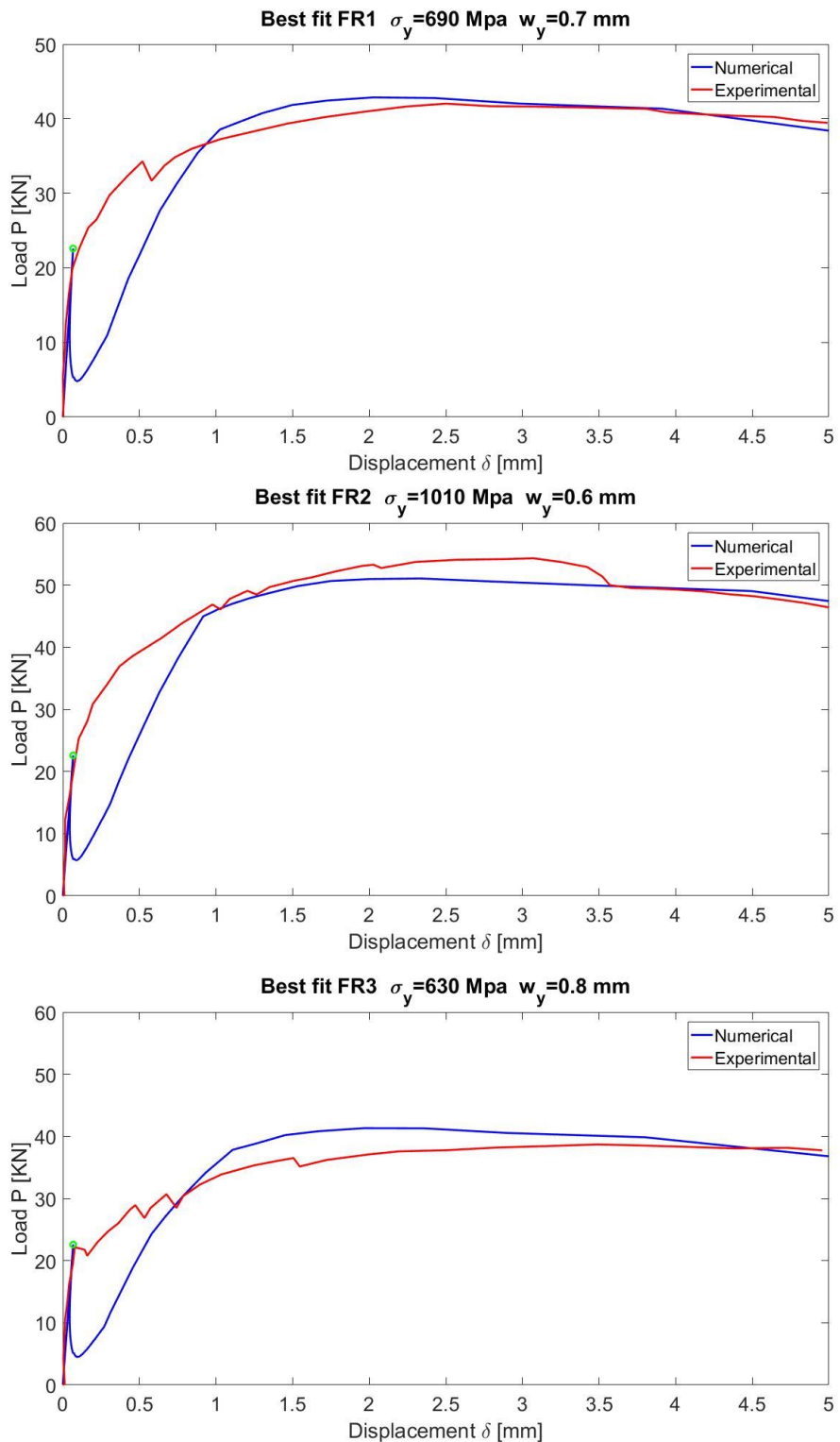


Figure 5.27 Best fitting for curves serie FR

The identifying parameters are collected in Tables from 5.17 and 5.20:

ID	w_y	σ_y
BR1	0.8	670
BR2	0.8	700
BR3	0.8	710
AVG	0.8	693

Table 5.17 Average value of mechanical parameters

ID	w_y	σ_y
CR1	1.1	700
CR2	0.8	790
CR3	0.6	700
AVG	0.8	730

Table 5.18 Average value of mechanical parameters

ID	w_y	σ_y
ER1	0.7	450
ER2	0.4	900
ER3	0.8	590
AVG	0.6	647

Table 5.19 Average value of mechanical parameters

ID	w_y	σ_y
FR1	0.7	690
FR2	0.6	-
FR3	0.8	630
AVG	0.7	652

Table 5.20 Average value of mechanical parameters

- **PREDICTION**

using the average parameters obtained from the best fitting procedure, the $P - \delta$ experimental curves of the HRC elements were reproduced and are showed in following figures.

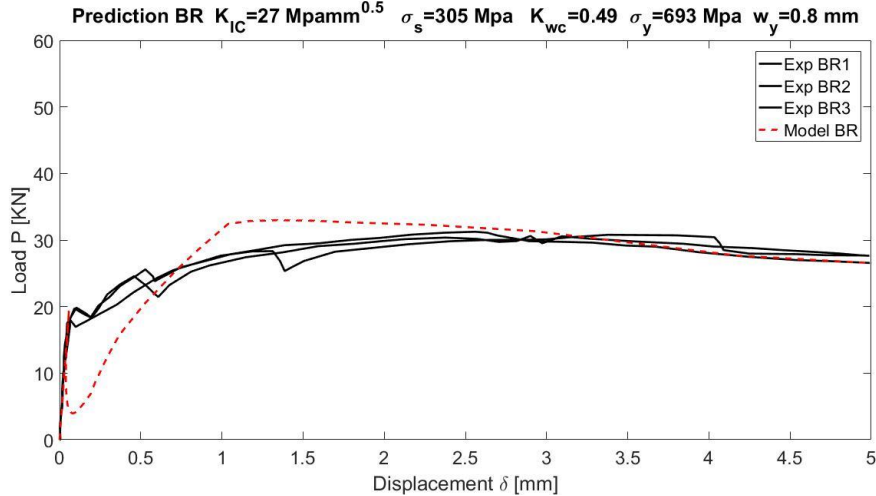


Figure 5.28 Predictions for curve BR (bar reinforcement 1Φ6)

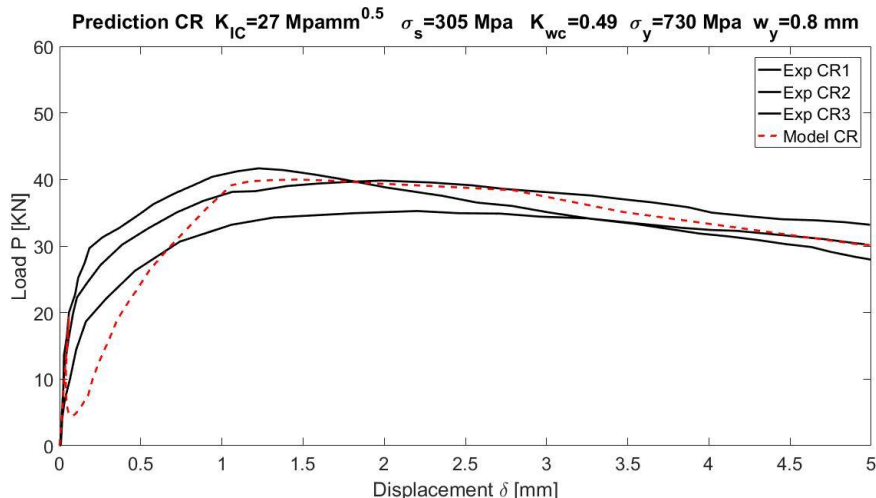


Figure 5.29 Predictions for curve CR (bar reinforcement 1Φ6)

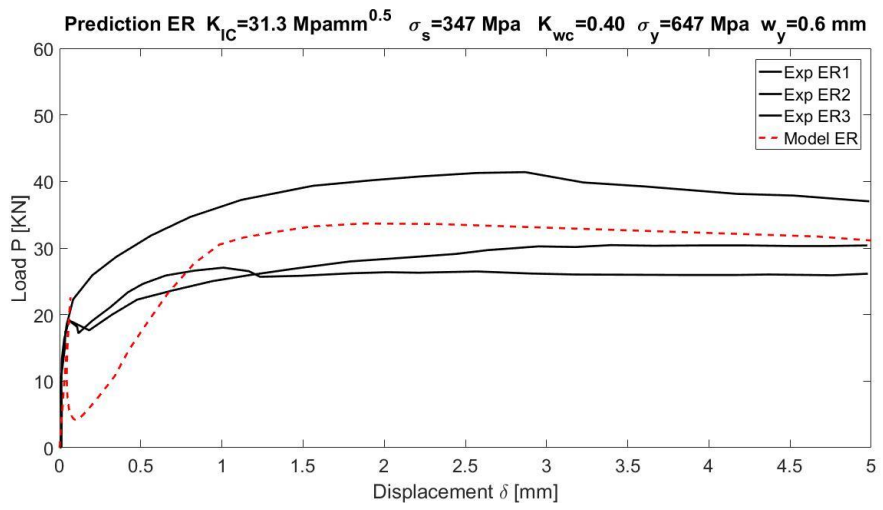


Figure 5.30 Predictions for curve ER (bar reinforcement 1Φ6)

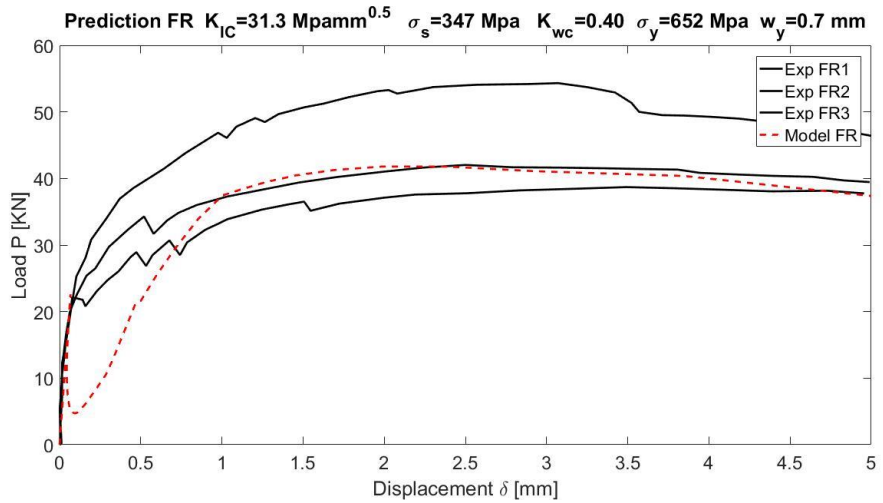


Figure 5.31 Predictions for curve FR (bar reinforcement 1Φ6)

6 Conclusions

The aim of this work was to enable the Bridged Crack Model to analyse the behaviour of HRC elements. The model assumes the crack propagation condition in according to LEFM, considering only the Mode I opening, that occurs when the stress-intensity factor, K_I , reaches its critical value, K_{IC} .

This was possible due to the implementation of two already existing constitutive laws within the algorithm. In addition, three scale-dependent dimensionless numbers have been defined, which synthetically describe the response of the HRC element.

The first one, the *bars reinforcement brittleness number*, N_{Pb} , shows this expression:

$$N_{Pb} = \rho \frac{\sigma_y}{K_{IC}} h^{0.5}$$

The second dimensionless parameter, the *fibre reinforcement brittleness number*, has the following expression:

$$N_{Pf} = V_f \frac{\sigma_s}{K_{IC}} h^{0.5}$$

The last dimensionless parameter is the *pull-out brittleness number* and has the following expression:

$$N_w = \frac{Ew_c}{K_{IC}h^{0.5}}$$

The influence of these parameters on the flexural response was widely discussed by means of numerical analyses. The *bars reinforcement brittleness number* defines the final plastic plateau; increasing the value of N_{Pb} , the minimum reinforcement condition can be reached even with low values of N_{Pf} and N_w .

The value of N_{Pf} influences in particular the post-cracking response; by increasing N_{Pf} , there is a ductile-to-brittle transition regarding the Stage II of the response, even if the content of bars reinforcement is not sufficient to guarantee an hardening response.

The value of N_w influences the fibre's contribution; with a low value of N_w the effect of the fibres vanishes quickly and the response of the element tends to the plastic plateau due to the bars reinforcement.

Finally, the comparison with the experimental campaigns reported in the literature confirmed the effectiveness of the model is able in reproducing the experimental responses experimentally verified.

7 References

- Abdallah S., Fan M. and Rees D. W. A. (2018), “Bonding Mechanisms and Strength of Steel Fiber–Reinforced Cementitious Composites: Overview”, *Journal of Materials in Civil Engineering*, Vol. 30
- Altun F., Haktanir T., Ari K. (2007), “Effects of steel fiber addition on mechanical properties of concrete and RC beams”, *Construction and Building Materials*, Vol.21, pp 654-661
- Barenblatt G.I., (1962), “The Mathematical Theory of Equilibrium Cracks in Brittle Fracture”, *Advances in Applied Mechanics*, Vol.7, pp 55-129
- Barros J.A.O.; Taheri M., Salehian H., (2015), “A model to simulate the moment-rotation and crack width of FRC members reinforced with longitudinal bars”, *Engineering Structures*, Vol. 100, pp. 43-56
- Behbehani H.P., Nematollahi B., Mohd A. R., Lai F. C., (2012), “Flexural Behavior of Steel -Fiber-Added-RC (SFARC) Beams with C30 and C50 Classes of Concrete”, *International Journal of Sustainable Construction Engineering & Technology*, Vol.3, pp. 54-64
- Ballarini R. and Muju S., (1993), “Stability Analysis of Bridged Cracks in Brittle Matrix Composites, *Journal of Engineering for Gas Turbines and Power*, Vol. 115, pp. 127-138
- Blanco A., Pujadas P., De la Fuente A., Calavaro S., Aguado A., (2013), “Application of constitutive models in European codes to RC-FRC”, *Construction and Building Materials*, Vol. 40, pp. 246-259
- Bosco C. and Carpinteri A. (1991), “Fibre toughening and crack growth stability in fibre reinforced disordered materials”, *Fracture process in Concrete, Rock and Ceramics*
- Bosco C. and Carpinteri A. (1991), “Fibre toughening and crack growth stability in fibre reinforced disordered materials”, *Fracture process in Concrete, Rock and Ceramics*
- Carpinteri A. (1981), “A Fracture Mechanics Model for Reinforced Concrete Collapse”, in *Proceedings of the IABSE colloquium on advanced mechanics of reinforced concrete*, Delft
- Carpinteri A. (1984), “Stability of fracturing process in R.C. beams”, *Journal of Structural Engineering (ASCE)*, Vol. 110, pp. 544-558

Carpinteri A. (1994) “Scaling laws and renormalization groups for strength and toughness of disordered materials”, *International Journal of Solids and Structures*, Vol. 31, pp. 291-302

Carpinteri A. and Carpinteri An. (1984), “Hysteretic behaviour of R.C. beams”, *Journal of Structural Engineering* (ASCE), Vol. 110, pp. 2073-2084

Carpinteri A. and Massabò R. (1996), “Bridged versus cohesive crack in the flexural behavior of brittle-matrix composites”, *International Journal of Fracture*, Vol. 81, pp. 125-145

Carpinteri A. and Massabò R. (1997), “Continuous vs discontinuous bridged crack model of fiber-reinforced materials in flexure”, *International Journal of Solids and Structures*, Vol. 34, pp. 2321-2338

Carpinteri A. and Massabò R. (1997), “Reversal in failure scaling transition of fibrous composites”, *Journal of Engineering Mechanics* (ASCE), Vol. 123, pp. 107-114

Carpinteri A., Ferro G., Ventura G., (2003), “Size effects on flexural response of reinforced concrete elements with a nonlinear matrix”, *Engineering Fracture Mechanics*, Vol. 70, pp 995-1013

Carpinteri A., Ferro G., Ventura G., (2007), “Minimum reinforcement in concrete structures and material/structural instability”, *International Journal of Fracture*, Vol. 146, pp. 213-231

Carpinteri A. and Puzzi S. (2007), “The Bridged Crack Model for the Analysis of Brittle Matrix Fibrous Composites Under Repeated Bending Loading”, *Journal of Applied Mechanics* Vol. 74, pp. 1239-1246

Carpinteri A., Cadamuro E., Ventura G. (2015), “Fiber-reinforced concrete in flexure: a cohesive/overlapping crack model application”, *Materials and Structures*, Vol.48 pp. 235-247

Carpinteri A. and Accornero F. (2019), “The Bridged Crack Model with multiple fibers: Local instabilities, scale effects, plastic shake-down, and hysteresis”, *Theoretical and Applied Fracture Mechanics*, Vol. 104

Carpinteri A., Accornero F. and Rubino A., (2019), “Ductile-to-Brittle Transition in Fiber-Reinforced Brittle-Matrix Composites: Scale and Fiber Volume Fraction Effects”, in: *Proceeding of 10th International Conference on Fracture Mechanics of Concrete and Concrete Structures*. FraMCoS-X, Bayonne

Carpinteri A. and Accornero F. (2020), “Residual crack opening in fiber-reinforced structural elements subjected to cyclic loading”, *Strength, Fracture and Complexity*, Vol. 12, pp. 63-74

Chiaia B., Fantilli A. P., Vallini P. (2007), “Evaluation of minimum reinforcement ratio in FRC members and application to tunnel linings”, *Materials and Structures*, pp 593-604

Chunxiang Q., Patnaikuni I., (1999), “Properties of high-strength steel fiber-reinforced concrete beams in bending”, *Cement and Concrete Composites*, Vol.21, pp. 73-81

Cox B.N., Marshall D.B., (1991), “Stable and unstable solutions for bridged crack in various specimens”, *Acta Metallurgica et Materialia*, Vol. 39, pp. 579-589

Cunha V., C. F. M., Barros J. A. O. and Sena-Cruz J. M. (2010), “Pullout Behavior of Stell Fibers in Self-Compacting Concrete”, *Journal of Materials in Civil Engineering*, Vol. 22, pp. 1-9

Dancygier N.A., Berkover E., (2012), “Effect of Steel Fibers on the Flexural Ductility of Lightly Reinforced Concrete Beams”, *Innovative Materials and Techniques in Concrete Construction: ACES Workshop*, pp. 197-207

Dugdale D. S. (1960), “Yielding of Steel Sheets Containing Slits”, *Journal of Mechanics and Physics of Solids*, Vol. 8, pp. 100-104

Fantilli P. A., Chiaia B., Gorino A. (2016), “Unifield approach for Minimum Reinforcement of Concrete Beams”, *ACI Structural Journal*, pp. 1007-1116

Fantilli P. A., Chiaia B., Gorino A. (2016), “Fiber volume fraction and ductility index of concrete beams”, *Cement and Concrete Composites*, Vol. 65, pp. 139-149

Fantilli P. A. and Gorino A. (2020), “Scaled Approach to Designing the Minimum Hybrid Reinforcement of Concrete Beams”, *Materials*, Vol. 13

Facconi L., Plizzarri G., Minelli F., “Elevated slabs made of hybrid reinforced concrete: Proposal of a new design approach in flexure”, *International Federation for Structural Concrete*, Vol.20, pp 52-67

Hilleborg A., Moody M. and Petersson P. E. (1976), “Analysis of crack formation and crack growth in concrete by means of fracture mechanics and finite elements”, *Cement and Concrete Research*, Vol. 6, pp. 773-782

Holschemacher K., Mueller T., Ribakov Y. (2010), “Effect of steel fibres on mechanical properties of high-strength concrete”, *Materials and Design*, Vol. 31, pp. 2604-2615

Jenq Y. and Shah P.S., (1985), “Two Parameter Fracture Model for Concrete”, *Journal of Engineering Mechanics*, Vol. 111

Marshall D.B., Cox B.N., Evans A.G., (1985), “The mechanics of matrix cracking in brittle-matrix fiber composites”, *Acta Metallurgica*, Vol.33, pp 2013-2021

Meda A., Minelli F., Plizzari G.A., (2012), “Flexural behaviour of RC beams in fibre reinforced concrete”, *Composites: Part B*, Vol. 43, pp 2930-2937

Mobasher B., Yao Y., Soranakom C. (2015), “Analytical solution for flexural design of hybrid steel fiber reinforced concrete beams”, *Engineering Structures*, Vol.100, pp. 164-177

Naaman A. E., Namur G. G., Alwan J. M. and Najm H. S. (1991a), “Fiber pullout and bond slip. I: Analytical study”, *Journal of Structural Engineering*, Vol. 117, pp. 2769-2790

Naaman A. E., Namur G. G., Alwan J. M., and Najm, H. S. (1991b), “Fiber pullout and bond slip. II: Experimental validation.”, *Journal of Structural Engineering*, Vol. 117, pp. 2791-2800

Ning X., Ding Y., Zhang F., Zhang Y. (2015), “Experimental study and prediction model for flexural behavior of reinforced SSC beam containing steel fibers”, *Construction and Building Materials*, Vol. 93, pp. 644-653

Robins P., Austin S., Chandler J. and Jones P. (2001), “Flexural strain and crack width measurement of steel-fibre-reinforced concrete by optical grid and electrical gauge methods”, *Cement and Concrete Research*, Vol. 31, pp. 719-729

Robins P., Austin S. and Jones P. (2002), “Pull-out behaviour of hooked steel fibres”, *Materials and Structures*, Vol. 35, pp. 434-442

Robins P., Austin S. and Jones P. (2003), “Spatial distribution of steel fibres in sprayed and cast concrete”, *Magazine of Concrete Research*, Vol. 55, pp. 225-235

Robins P., Austin S. and Jones P. (2003), “Predicting the flexural load-deflection of steel fibre reinforced concrete from strain, crack-width, fibre pull-out and distribution data”, *Materials and Structures*, Vol. 41, pp. 449-46

Tiberti G., Trabucchi I., AlHamaydeh M., Minelli F., Plizzari G., (2017), “Crack control in concrete members reinforced by conventional rebars and steel fibers”, *IOP Conferences Series: Materials Science and Engineering*, Vol. 246, pp.1-10

Zhiguo Y., Chen X., Dong S., (2011), “Ductility and strength of hybrid fiber reinforced self-consolidating concrete beam with low reinforcement ratios”, *Systems Engineering Procedia*, Vol.1, pp.28-34

